Construction of a 408 nm Laser System

for Use in Ion Interferometry

James Lawrence Archibald II

A Master's Thesis submitted to the faculty of
Brigham Young University
in partial fulfillment of the requirements for the degree of

Master of Science

Dallin S. Durfee, Advisor

Department of Physics and Astronomy

Brigham Young University

October 2015

ABSTRACT

Construction of a 408 nm Laser System

for Use in Ion Interferometry

James Lawrence Archibald II

Department of Physics and Astronomy

Master of Science

This work reports on the construction of a 408 nm laser system designed to drive stimulated Raman transitions between the $F = 4$ and $F = 5$ $^2\mathrm{S}_{1/2}$ states of $^{87}\mathrm{Sr}^+$ using the $^2\mathrm{P}_{3/2}$ state as the intermediate state. This laser system will be used as part of a $^{87}\mathrm{Sr}^+$ ion interferometer. This work also includes a discussion of relevant theory describing the interaction of the ions and laser, along with a calculation of the transition rates as a function of laser power and detuning.

ACKNOWLEDGMENTS

Contents

List of Figures

Chapter 1

Background

In this chapter, I discuss the overall project of which the 408 nm 5 GHz detuned laser system is a part. I will give a detailed summary of the preparation the atoms undergo before they are manipulated by the laser system whose construction is the main topic of this thesis. I will also discuss the ion interferometer project vis-à-vis other physics experiments.

1.1   Ion interferometer basic overview

The central feature of any interferometer is that there is a travelling wave that is split and sent along two distinct paths. At some later point, the waves from the two paths are recombined. The output of the interferometer depends on the relative phase acquired by the wave as it travels along the two distinct paths of the interferometer. The goal of the ion interferometer project is to create an interferometer that uses the atomic wavefunction of a beam of travelling Strontium ions to achieve interference. In other words, we hope to split and recombine the atomic wavefunction of Strontium ions in such a way that the atomic wavefunction is nonzero along two distinct paths through space. The output of the interferometer will give information about the relative phase shift acquired by the ions as

they travel along each of the arms of the interferometer.

The ^{87}Sr$^+$ ion interferometer uses a Mach-Zehnder configuration, which refers to the fact that the two paths along which the waves travel enclose a non-zero area. Fig. 1.1 illustrates an optical Mach-Zehnder interferometer and compares this with the matterwave Mach-Zehnder interferometer that we are trying to build.

In order to accomplish ion interferometry, we must first acquire a suitable source of ^{87}Sr$^+$ ions. There are three basic processes that must be accomplished with the Sr atoms in order to successfully operate the interferometer:

- Generation of a low velocity beam of cold, neutral Strontium atoms

- Ionization of Strontium Atoms

- Atom interferometry

A schematic of the apparatus is depicted in Figure 1.2.

1.2   Trapping of neutral strontium and the low velocity intense source (LVIS)

We created a Low Velocity Intense Source (LVIS pronounced "Elvis") [1] that provides a cold beam of slow-moving, neutral Strontium atoms. The techniques we used were developed by the Cornell group at UC Boulder [2]. The LVIS consists of a Magneto-Optical Trap (MOT) where one of the mirrors has a small hole drilled in it[1]. This allows some of the atoms to escape the trap. These atoms have a relatively narrow distribution of velocities.

---

[1]This hole was drilled in-house and the details of how we avoided damage and tests that verify the integrity of its optical surface can be found in Ref. [1].
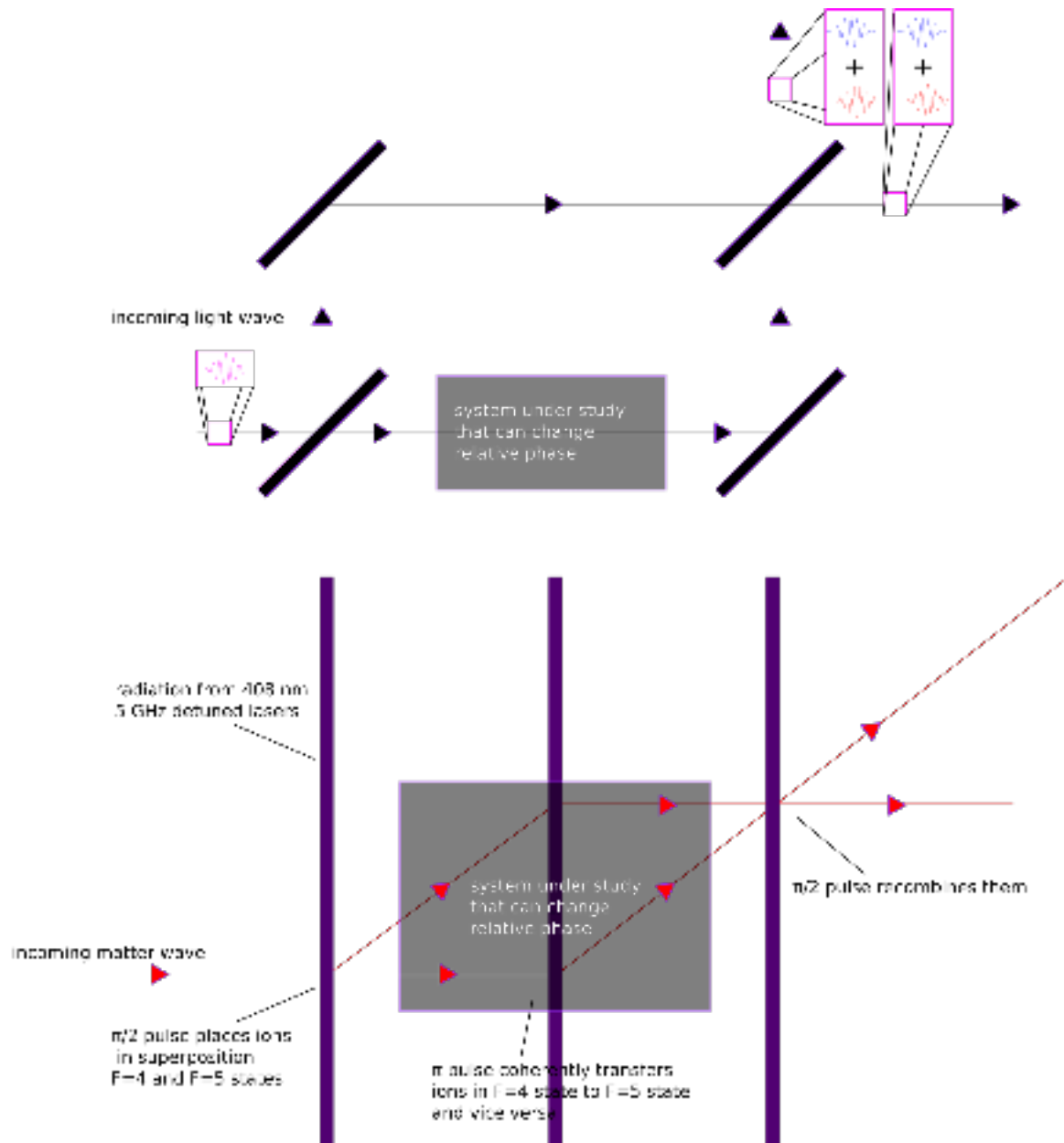
Figure 1.1 A traditional realization of an optical Mach-Zehnder interferometer (top) juxtaposed with a sparse diagram of the ion interferometer (bottom). The optical Mach-Zehnder interferometer achieves interference of light waves and uses traditional glass optics to split and recombine the beams. The ion interferometer is designed to achieve interference of matter waves. The ion interferometer splits the atomic wavefunction of the Strontium ions using continuous wave lasers. These lasers manipulate the ions in a coherent way and place them in a superposition of states that correspond to taking one path or the other.
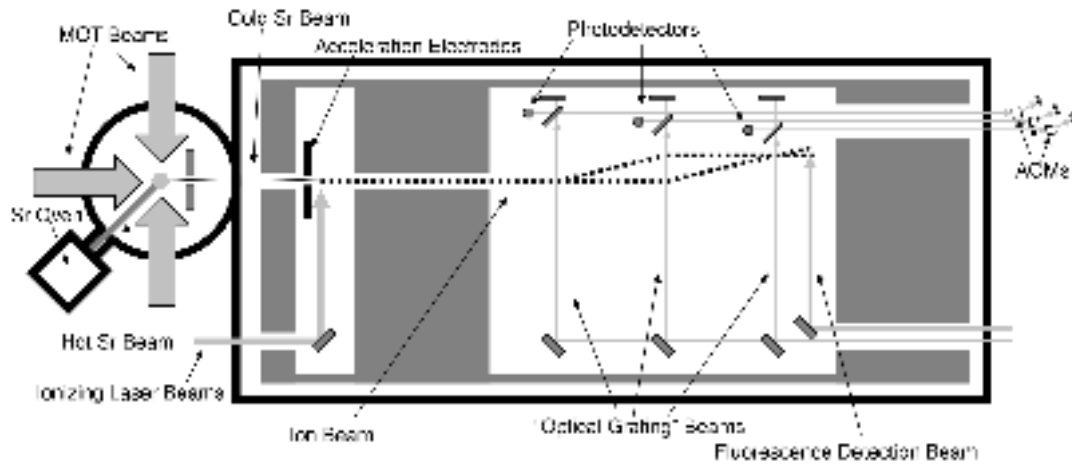
Figure 1.2 A schematic diagram of the $^{87}Sr^+$ ion interferometer. Neutral strontium atoms start out in the Sr Oven depicted on the left part of the diagram. The heated chunks of strontium release atoms into the vacuum chamber where some of them are cooled and trapped by the MOT beams. One of the mirrors used on the MOT beams has a hole in it, which allows some of the ions to escape. The MOT with a hole in it comprises the Low Velocity Intense Source (LVIS). Neutral atoms that emerge from the LVIS enter a larger vacuum chamber where they are ionized by a pair of lasers. After this, they are accelerated by an electric field into the part of the chamber where actual interferometry will take place. The "Optical Grating" Beams are generated by the 408 nm 5GHz detuned laser system that is the topic of this thesis.

The MOT at the heart of the LVIS uses the standard techniques for cooling and trapping atoms, as described by Erickson [1]. It utilizes the $5s^2$ $^1S_0$ to $5s5p$ $^1P_1$ transition in neutral ^{87}Sr to cool and trap the atoms. It selectively traps only the ^{87}Sr isotope of strontium. The trap consists of 6 red-detuned laser beams originating from the 460.8 nm laser system described in Ref. [1]. These point from each of six orthogonal directions towards the center of the MOT. The dominant cooling effect in the MOT is Doppler cooling. The trap also relies on the magnetic field produced by a pair of permanent rare-earth magnets. This magnetic field causes the atoms to experience a Zeeman shift whose magnitude depends on their location. This process effectively confines the coldest atoms to a small region.

The MOT is loaded via a Sr oven. The Sr vapor that is produced by heating a sample of Sr passes through a small Zeeman slower in order to maximize the quantity of atoms inside the trap.

Whenever the MOT is running, atoms escape through the hole in the mirror, thereby providing us with the LVIS. The atoms that exit the LVIS through the hole in the mirror are then accelerated by a sort of "Zeeman accelerator" or "reverse-Zeeman slower." This process works by a principle of operation that is similar to the principle of operation of a Zeeman slower. The permanent magnets that produce the appropriate magnetic field gradients inside the MOT also create a magnetic field outside the MOT. As the atoms exit the LVIS, this magnetic field gradient produced by the permanent magnetics results in a Zeeman shift whose magnitude changes. The change of the resonance frequency as a result of the Zeeman shift approximately cancels out the change in resonance caused by the Doppler shift experienced by the atoms as they are accelerated away from the trap by the 461 nm laser. The reverse-Zeeman slower effect is a unique feature of our LVIS. A typical LVIS would use Helmholtz coils to produce the magnetic fields at the center of the trap and the magnetic fields produced would not exhibit a reverse-Zeeman slowing effect.

1.3   Ionization of strontium

The next step is to selectively ionize the ^{87}Sr to produce ^{87}Sr$^+$. We will accomplish this using a pair of lasers tuned to resonant transitions of Sr. First, we stimulate the 5s^2 ^{1}S$_0$ $\rightarrow$ 5s5p ^{1}P$_1$ transition using a 461 nm laser. Conveniently, this is the same 461 nm transition used to cool the atom. The second transition is the 5s5p ^{1}P$_1$ $\rightarrow$5p^2 ^{1}D$_2$ transition. The ^{1}D$_2$ state is 57 meV above the ionization threshold [3]. This particular state rapidly and spontaneously autoionizes. Stimulation of this transition requires a 405 nm laser. This is also a very convenient wavelength since we can drive this transition with diode lasers that are widely-produced and readily commercially available. Because this process relies on a pair of resonant transitions, we expect to be able to ionize nearly 100% of the atoms in this way.

After passing through the ionization lasers, the ions are accelerated by an electric field produced by two copper electrodes held at constant potential. We can control the speed of the atoms by adjusting the potential on the electrodes.

1.4   Interferometry

After passing throught the electrodes, the ions enter the third major segment of the experiment, which is where the ion interferometry takes place. In this segment of the experiment, we will use a pair of laser beams from the lasers which are the topic of this thesis, which differ in frequency by the 5 GHz hyperfine splitting of the ground state of ^{87}Sr$^+$ to coherently manipulate the internal state of the ^{87}Sr$^+$ ions and to impart small amounts of momentum to the ions. The interaction between the 408 nm 5 GHz detuned lasers and the ions relies on both absorption and stimulated emission of photons. The experiment is designed to have three pairs of counterpropagating 408 nm laser beams perpendicular to the trajectory of

the ions through the chamber. These lasers are necessary in order to produce two distinct paths along which the ions' wavefunctions can propagate. We will use stimulated Raman transitions as done by Kasevich and Chu [4]. This is a two photon process: the ions will be driven from one state to another using a third state as an intermediate state. The lasers will induce stimulated Raman transition between the two ^{2}S$_{1/2}$ (5s) ground states corresponding to $F = 4$ and $F = 5$. The transition uses the ^{2}P$_{3/2}$ (5p) state as an intermediate state.

As the ions pass through the beams, they absorb a photon from one of the beams and then are stimulated to emit a photon into the other beam. Each of these imparts $h/\lambda \approx$ 1.6e-27 kg m/s of momentum to the ion in the same direction. The change in the ion's state after interacting with the lasers can be expressed in terms of the following states:

$$|e, \mathbf{p}_e\rangle = |e\rangle \otimes |\mathbf{p}_e\rangle \tag{1.1}$$

$$|g, \mathbf{p}_g\rangle = |g\rangle \otimes |\mathbf{p}_g\rangle \tag{1.2}$$

where $|e\rangle$ represents the internal excited state of the ion (^{2}S$_{1/2}$ with $F = 4$) and $|g\rangle$ represents the internal ground state of the ion [5]. The momentum of the overall atomic wave function is represented by $\mathbf{p}$, with $\mathbf{p}_g$ representing an ion that has not absorbed any momentum from the lasers and $\mathbf{p}_e$ representing an ion that has absorbed two photon recoils worth of momentum from the counterpropagating beams.

In order to send the ions along two distinct paths, we have designed the system so that first pair of counterpropagating beams puts the ions into a superposition of two states:

$$\frac{1}{\sqrt{2}} e^{i\phi} |e\rangle \otimes |\mathbf{p}_e\rangle + \frac{1}{\sqrt{2}} |g\rangle \otimes |\mathbf{p}_g\rangle. \tag{1.3}$$

This is known as a $\pi/2$ pulse because it changes the state of the system into an equal superposition, which is represented by the angle of $\pi/2$ radians in the Bloch sphere description of a two state system. Here ϕ represents any relative phase shift the ions might acquire during

this first interaction. In our system, this phase shift would depend on the optical phase of the light. The second pair of beams must drive the

$$|e\rangle \otimes |\mathbf{p}_e\rangle \to e^{i\phi'}|g\rangle \otimes |\mathbf{p}_g\rangle \tag{1.4}$$

$$|g\rangle \otimes |\mathbf{p}_g\rangle \to e^{i\phi''}|e\rangle \otimes |\mathbf{p}_e\rangle \tag{1.5}$$

transitions where ϕ' and ϕ'' represent phase changes due to details of the light-atom interaction. This interaction is known as a π pulse.

The final pair of beams provides another $\pi/2$ pulse to the two halves of the ion's wave function. This pulse recombines them, causing them to interfere.

We will analyze the atomic transitions more completely in Chapter 3. An overview of the laser system can be found in Chapter 2. More information on the master laser configuration and setup can be found in Chapter 4. Information about the Acousto Optic Modulator (AOM) configuration can be found in Chapter 5. The process of injection locking the slave lasers is discussed in more detail in Chapter 6. Data from the working system can be found in Chapter 7.

1.5 Precedents

In this section, I will discuss some related experiments. These experiments represent the intellectual heritage of our work. A few of the ideas that are central to our project are over 100 years old. Other experiments to which we are indebted are of much more recent vintage. These more recent experiments also pioneered many of the technologies, techniques, and tools that we use.

1.5.1 Interference effects involving light

Matterwave interferometry borrows many of its foundational concepts and terminology from interferometric light experiments. The wave nature of light has been the subject of serious study for a long time. It was first discussed as a way to explain diffraction. Grimaldi observed diffraction early on. Hooke, Huygens and Newton also did well-known early experimental and theoretical work involving the propagation of light and its interference phonomena. However, the word, "interferometer" usually refers to an experiment where light rays are split and then recombined in some way after travelling along two distinct paths. Young's double slit experiment, which played an important role in the acceptance of a wave model of light, could be viewed as an interferometer. Young placed two slits and passed light through them. He then observed a pattern of alternating dark and light fringes corresponding to the regions of constructive and destructive interference. This represents a type of interferometry since, for any given point on the output plane, there are two distinct, possible paths that the light could have taken to get there (one path passes through each slit). The output depends on the relative phase shift between the light travelling along each of the two paths.

Mach and Zehnder published work on their interferometers in 1892 and 1891 respectively [6] [7]. Their names are now synomous with the basic interferometer layout that they pioneered (see, for example, Fig. 1.1). "Mach-Zehnder" interferometer now refers specifi-

cally to any interferometer that uses different beam splitters to split and combine the wave and that encloses area. By contrast, a Michelson-Morley type interferometer uses the same beam splitter to both split and recombine the light. Thus, such an interferometer encloses no area. The original Michaelson-Morley interferometer was also among the most influential light interferometers. The goal of Michaelson's and Morley's original experiment was to look for ether drift and their famous null result was later interpreted as important early evidence of special relativity.

1.5.2   Experiments involing diffraction of matter waves

DeBroglie hypothesized that matter exhibits wave-like behavior. Some of the earliest direct confirmation of this was achieved by Davisson and Germer [8], whose electron scattering experiment was somewhat analogous to Bragg diffraction experiments performed using light. The first atomic diffraction experiment was by Estermann and Stern [9] [10]. Diffraction of matterwaves has also been the basis for a number of interferometers that use a series of physical diffraction gratings to separate, redirect and recombine matter waves of various types of massive particles. This was first achieved by Marton [11] for electrons and Rauch [12] for neutrons. The first atomic interferometers of this type were created by Pritchard [13] and Mlynek [14]. These experiments use gratings and slits similar to some of the early optics experiments. Experiments of this type have also been done with larger pieces of matter, including buckyballs [15] and other large molecules [16].

The development of techniques for the coherent control and measurement of atoms was a major boon to matterwave interferometry [10]. Rabi was among the first to use rf resonances to coherently control the internal states of molecules [17] [10]. Ramsey's work in creating long-lived superpositions and the method of separated oscillatory fields was similarly seminal [10] [18]. Bordé built [19] the first separated beam atom interferometer using light to split

the wavefunction. More recently, atom interferometers have been used for many different types of experiments. These have provided high-precision measurements of the fine structure constant [20] [21] [22], investigations of gravitational effects [23] [24] and ever tighter limits on potential deviations from Standard Model physics [25] [10] [26].

Kasevich and Chu pioneered the use of Raman transitions as atomic beam splitters [4]. The matterwave interferometers that they built are the most similar experiments to the ion interferometer that we are constructing. The project also relies on trapping and cooling of neutral ^{87}Sr, which was previously achieved and documented in Ref. [27]. Sr has been used in other experiments, including atomic clocks [28].

1.5.3 Laboratory-based electromagnetic tests

One possible application of our apparatus is to use the ^{87}Sr$^+$ ions to detect small electric fields in a setup like the one famously used by Cavendish in his early electrostatic experiments. Cavendish effectively measured fundamental electrostatic constants by measuring the electric field inside a charged, conducting enclosure. By demonstrating that the electric fields inside the enclosure were zero regardless of the charge on the enclosure, Cavendish was able to deduce that the repulsion between like electric charges falls off in proportion to the inverse of the square of the distance between them [29]. Many of the more recent tests of electrostatics were performed using setups similar to Cavendish's [30]. In fact, the main improvement that these experiments made over Cavendish's was that they used modern electronics rather than suspended pith balls to measure the electric field inside the conductor.

The ion interferometer relates to Cavendish's experiment in three ways: First, the ion interferometer could be used as the electric-field-detecting component in a Cavendish-type experiment. The ion interferometer will be very sensitive to electric fields and it could be placed inside a conductive shell whose electric potential is varied. In fact, it would

represent a significant improvement over current methods for measuring small electric fields in Cavendish-like experiments [3].

The second way in which our project is related to Cavendish's experiment is that it seeks to shed light on fundamental electromagnetic phenomena. If enclosed in a conducting shell (as mentioned in the previous paragraph), our experiment could be used to measure fundamental electrical constants. Cavendish was able to measure the $1/r^2$ dependence in what eventually became known as Coulomb's law. We hope that our experiment will be able to place limits on the photon rest mass.[2]

Third, Cavendish's experiment directly inspired our experiment. A former student in the group, Brian Neyenhuis, came across a practice GRE question about the best laboratory measurements to date confirming Coulomb's law, most of which are a variation on Cavendish's method. Neyenhuis started investigating the use of atomic physics techniques to improve these measurements when he learned that the key limiting factor in all cases was the experimenter's ability to measure small electric fields inside the conducting shell. Soon Neyenhuis and Durfee, along with another student, Christensen, had fleshed out their idea for creating an ion interferometer [31] [32].

Our project fits within a broader effort to perform laboratory tests of fundamental electromagnetic quantities. A good survey of the other experiments which test similar aspects of fundamental electromagnetic theory can be found in Ref. [33].

---

[2]Our experiment will also produce results that may be reported as ϵ in the $1/r^{2+\epsilon}$ generalization of Coulomb's law.

Chapter 2

Laser System Overview

This chapter provides a broad introduction to the laser system addressed in this thesis. More information on the master laser configuration and setup can be found in Chapter 4. Information about the Acousto Optic Modulator (AOM) configuration can be found in Chapter 5. The process of injection locking the slave lasers is discussed in more detail in Chapter 6. Data from the working system can be found in Chapter 7.

This thesis describes the construction of the laser system (408 nm 5 GHz detuned laser system) that I built from 2010-2012. The purpose of this system is to produce two lasers which are near resonant with the 5s ^{2}S$_{1/2}$ to 5p^{2}P$_{3/2}$ transition in ^{87}Sr+, but which differ in frequency by precisely 5 GHz. This frequency corresponds to the hyperfine splitting of the ground state. In other words, the $F = 4$ and $F = 5$ states of ^{87}Sr$^+$ differ in energy by $h \times 5$ GHz $\approx 3.313 \times 10^{-24}$J ≈ 20.7 meV. Tuning the lasers in this way is necessary to drive the stimulated Raman transitions for our ion interferometer project.

By the time I began work on this project, most of the planning for this laser system had already been done by Chris Erickson and Dallin Durfee. Chris had already ordered many of the parts, including most of the optics we would eventually need and the AOM. He also acquired most of the commercially-produced electronics that were ordered for this project.

The laser current drivers and temperature controllers were built in house by other students in the lab using the design discussed in Refs. [34] [35] [1]. Chris modified the laser diode housings to include an extra temperature sensor and he modified some of them so that they could be mounted on posts perpendicular to their usual orientation. Chris also built the first version of our spectrum analyzer. Chris had also already built part of the enclosure that goes around the system and he had already made an attempt to build an ECDL using one of the laser diodes and a grating. However, as I will discuss in Chapter 4, the final configuration of the master laser, including the selection of the diode and the final assembly and machining of the grating mount was done by me.

As detailed by the rest of this thesis, everything else that was done on the system was done by me. I did the optical layout of the system. I performed the characterization and selection of the diodes for the master and slave laser systems. I assembled the master and slave lasers in their final configuration. I installed all of the other components including the AOM, the optical isolators and all of the other components. I found the appropriate parameters to get the lasers to injection lock and to operate at the correct wavelength. I found the ECDL configuration that allowed the master laser to operate stably.

2.1   Basic design

The laser system consists of several components arranged together on a 12"×48" breadboard that is bolted to an optical table as well as electronic instrumentation which is separate from the breadboard. The breadboard is enclosed by a plastic case in order to reduce air currents, protect the optics, provide strain relief for cables, and beautify the experiment. The circuits that provide current to the lasers and the temperature controllers for the lasers are mounted on a shelf above the laser enclosure along with an RF generator and RF amplifier for driving the AOM and various pieces of test and measurement equipment.
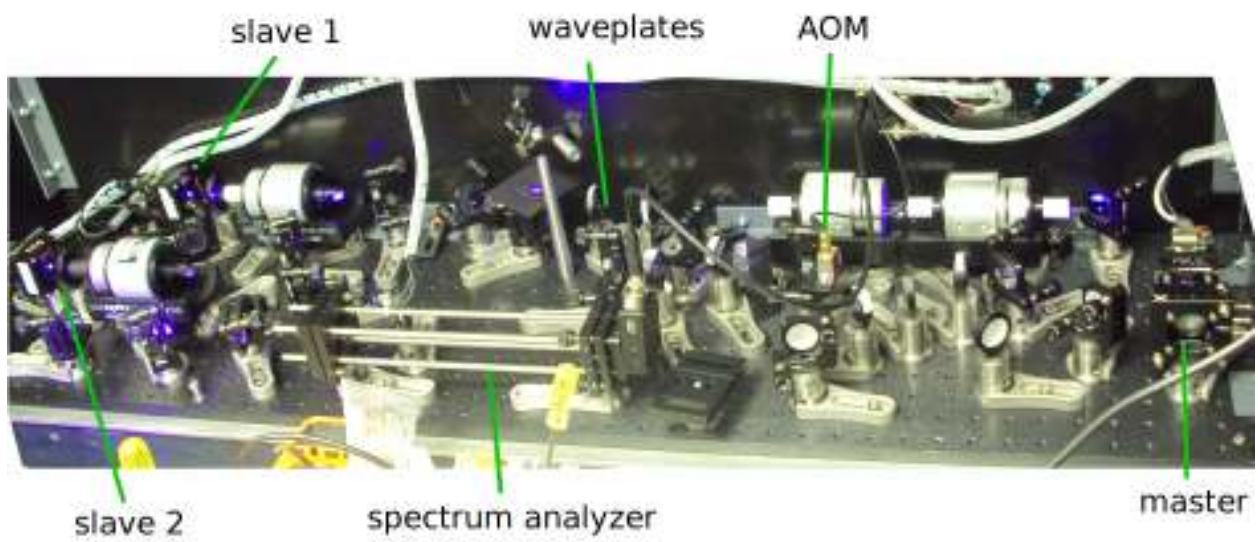
Figure 2.1 A photograph of the entire laser system while in operation.

There are three separate laser diodes in housings. One of them is designated the "master" laser. The other two are designated "slave 1" and "slave 2." The light that will actually be used on the atoms in the experiment is generated by the two slave lasers (slave 1 and slave 2). A diagram of the main components of the system can be found in Figure 2.2 while a picture of the completed setup can be found in Figure 2.1.

The system is designed so that some small fraction of the light coming from the master laser is shifted in frequency by an Acousto Optic Modulator (AOM) and used to seed one of the slave lasers. The unshifted light passing through the AOM is then retroreflected so that it passes through the AOM in the opposite direction and some small fraction of this light is then shifted in the opposite direction. This light is used to seed the other slave laser. Coupling the shifted light into the slave lasers and adjusting the slave lasers in such a way that they lase in a mode that is resonant with the light coupled into them is what is meant by "injection locking."

The advantage of this setup is that as the frequency of the master laser drifts, both slaves will drift with it, while the relative frequency difference between the slave lasers will remain stable. As I will later show in Chapter 3, the experiment is less sensitive to common mode drift between the two slave lasers than it is to drifts of the individual slaves relative to one another.

The basic objectives that I accomplished were (1) to make a stable master laser tuned near the mean of the frequencies that we desire out of the slave lasers, (2) to shift the light from the master laser using an AOM (3) to injection lock the slave lasers, and (4) to calculate the powers and frequency offsets necessary for our experiment.
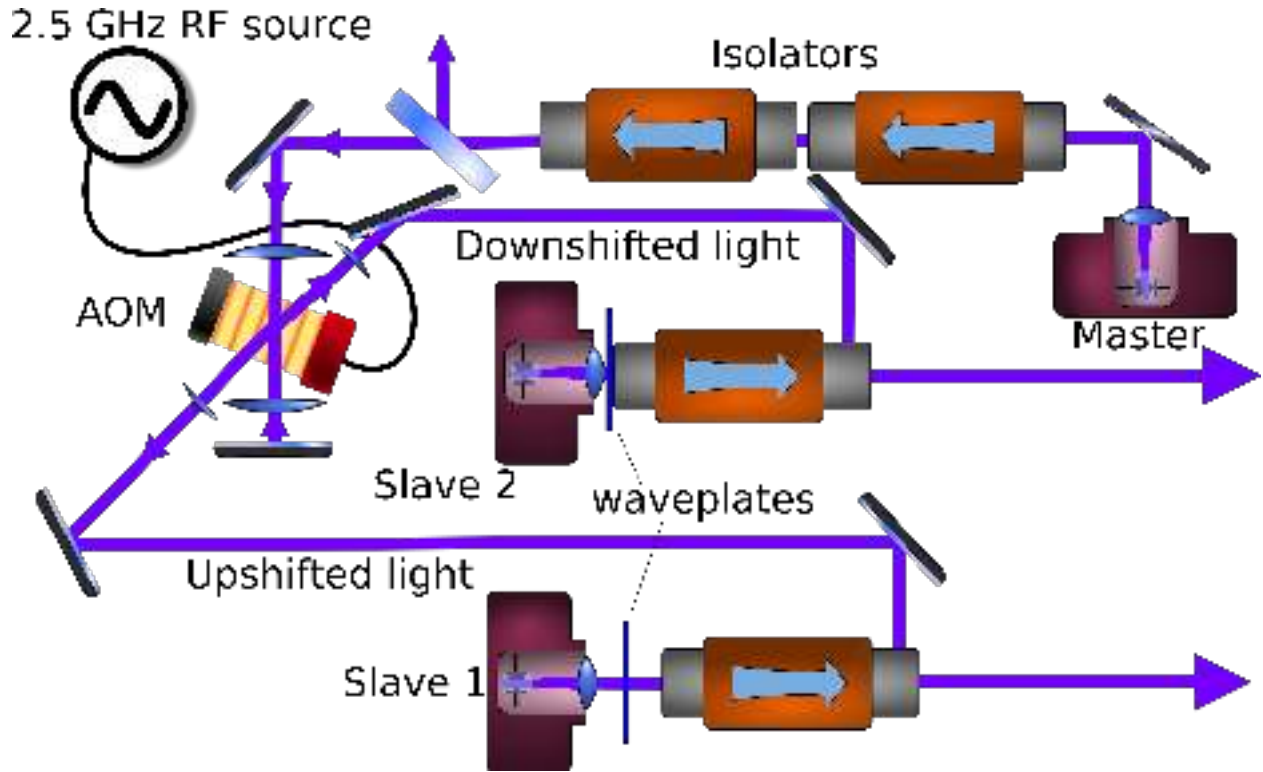
Figure 2.2 A schematic diagram of the basic pieces of the 408 nm 5 GHz detuned laser system apparatus. The master laser is depicted on the upper right. Its beam passes through two optical isolators in series. After this, the AOM is depicted with the upshifted and downshifted light coming out at exaggerated angles. These beams are then coupled into the rejection ports of two other optical isolators. Half waveplates are mounted in front of each of the slave lasers to rotate the polarization of the light to match the input polarizers on the isolators. The beams that will be used in the experiment are shown exiting through the lower right side of the diagram. The waveplates and polarizing beam cube that are used to adjust the light coupling into the AOM are not depicted.
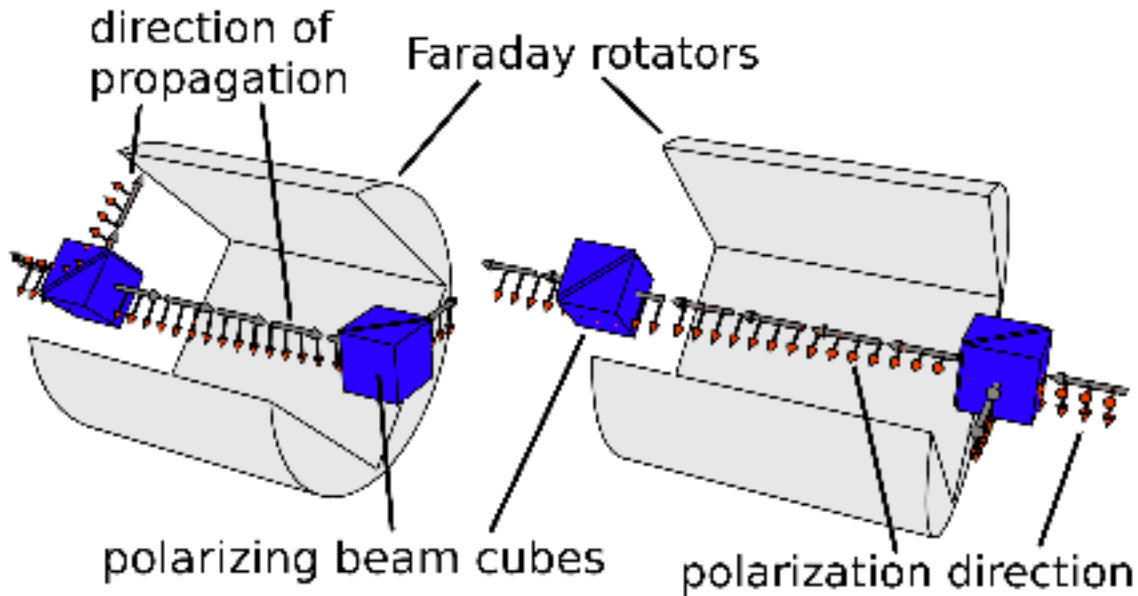
Figure 2.3 Optical isolators work via Faraday rotation of the light. The Faraday effect occurs in certain materials when placed under a strong magnetic field. The Faraday effect results in the rotation of the polarization of light as it passes through a crystal. The direction of the change in polarization is depicted in the diagram. The image on the left shows an isolator rejecting light, while the image on the right depicts the same isolator allowing light travelling in the opposite direction to pass through.

2.2   Following the beam path

Light from the master laser passes through two optical isolators. These use Faraday rotation and a pair of glan polarizers to ensure that light travelling away from the master laser is allowed to propagate while light is prevented from coming back into the master laser. See Fig. 2.3.

Optical isolators are important because the stability of the master laser and the injection locking of the slave lasers requires control of the light being coupled into the laser cavity. By

installing isolators, I can prevent unwanted reflections from coupling back into the master laser. This is an especially serious issue for the master laser since later in the beam path, the beam is retroreflected in such a way that, absent the isolators, light would couple directly back into the master laser.

The beam then passes through a pair of waveplates and a polarizing beam cube, which serves the dual purpose of allowing us to attenuate the portion of the beam that goes through the AOM and splitting off a beam that can be used in our spectrum analyzer. A discussion of the method I used for adjusting the quantity of light passing through these waveplates can be found in Appendix D.

After this, the laser is passed twice through an Acousto-optic Modulator (AOM). The first-order diffracted beam from the first pass through the AOM produces light that is shifted up in frequency (down in wavelength). However, most of the power is contained in the 0th order beam that passes through the AOM without being shifted at all. I collimate the 0th order beam and retroreflect it, thereby sending it through the AOM in the opposite direction. This pass produces a weak beam that is downshifted in frequency. I thus end up with two beams, one of which is shifted upwards by 2.5 GHz relative to the master laser and the other of which is shifted downward by 2.5 GHz.

These two shifted beams are then coupled to the internal cavities of the two slave lasers. The shifted beams seed the slave lasers, or in other words, the slave lasers amplify the light from the shifted beams and lase in a mode that is resonant with it. Coupling the seed light to the slave laser cavities requires that the incoming seed light propagate along the same path as the outgoing light from the slave laser. In order to achieve this, each slave laser has an optical isolator in its beam path. The optical isolator is configured to allow light emanating from the slave laser to come out its normal output port. However, the seed light is coupled to the laser by shining it through one of the rejection ports of the isolator (i.e. one

of the ports that light with the wrong polarization or light travelling the wrong direction is siphoned towards). In this way, we are able to create overlapping, counterpropagating beams with the correct polarizations (the polarization of the seed light matches the polarization of the light generated by the laser). The polarization considerations are not totally trivial, but the polarization of the light is crucial to understanding how the isolator works and why the isolator is necessary. However, whether the optical isolator is used for rejecting light that is propagating in the wrong direction, or whether it is used to couple light into a laser, in either case it is allowing light with the same polarization at one port to travel along different paths depending on the direction the light is propagating. These considerations are explained more deeply in Chapter 6.

The outputs of these two lasers are what we will send to the ion interferometer experiment to stimulate Raman transitions. Some of the light from each of the slaves are also redirected to the spectrum analyzer using beamsplitters or, for the purposes of characterization, mirrors that will later be removed.

2.3   Verifying the output of the 408 nm 5GHz detuned laser system

I use a Fabry-Perot spectrum analyzer to monitor whether the slaves are injection locked and to verify that the master laser and slave lasers are running single mode. The spectrum analyzer is depicted in Fig. 2.4. The spectrum analyzer is a semiconfocal cavity of length 200 mm whose length can be varied electronically. The flat, partially reflective mirror through which light enters the cavity is mounted on a Thorlabs KC1-PZ Kinematic Mirror Mount that features piezo-electric actuators. This allows for fine control of the mirror's position (and therefore fine changes in the cavity length). At the other end of the cavity there is a
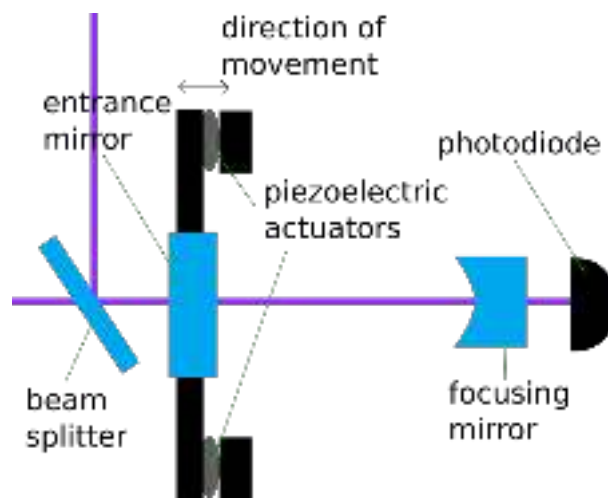
Figure 2.4 A diagram of the spectrum analyzer. The spectrum analyzer consists of a Fabry-Perot cavity of adjustable length. The photodiode on the far right of the diagram outputs a signal that shows when the incoming lasers are resonant with the cavity. The left cavity mirror is mounted on a piezoelectric mount that allows fine displacement of the mirror using electronic controls. There is a beamsplitter before the cavity that allows us to couple two different lasers to the cavity at the same time. A mirror on a flip mount (not shown) allows either the master laser and one slave laser or either of the two slave lasers to be coupled to the cavity simultaneously.

curved mirror of focal length 200 mm. Behind this there is a photodiode [1].

The piezoelectric actuators are connected to a commercially available piezo control box that sweeps the voltage in a sawtooth wave type pattern with a frequency ~20Hz. I use this to modulate the length of the cavity. When the cavity length is such that the coupled light is close to a resonance of the cavity, more light transmits through the cavity and there is a higher signal on the photodiode. During each period of the sweep, the length of the cavity changes by enough that light at any given frequency will go into and out of resonance several times. Therefore, we would expect to see a repeating pattern of peaks where each peak corresponds to the same frequency of light resonating with the cavity. Some sample data from the spectrum analyzer is shown in Figure 2.5.

The free spectral range (FSR) of the cavity is defined as the spacing between adjacent resonant frequencies of the cavity. Therefore, if f is some frequency of light that is resonant with a cavity, $f + m \times \text{FSR}$ will also be a resonant frequency of the cavity for any integer m. In the case of a semiconfocal cavity like the one used in our setup, the free spectral range is given by

$$\text{FSR} = \frac{c}{8L}. \tag{2.1}$$

Our cavity is a semiconfocal cavity of length 20 cm. The free spectral range of this cavity is thus 187 MHz. Knowing the free spectral range of the cavity allows us to interpret the data from the spectrum analyzer in terms of actual light frequencies

As an example, we consider a case where light of frequency f and light at frequency $f - \text{FSR}$ are coupled simultaneously to the cavity. Based on the definition of FSR, the length of the cavity corresponding to the mth order mode resonant with the light with frequency f should also be resonant with the $m - 1$ order mode of the light with frequency $f - \text{FSR}$. If we adjust the cavity length so that it is resonant with the m order mode of the

---

[1]This photodiode is from the Thorlabs DET family of reversed biased photodiode products
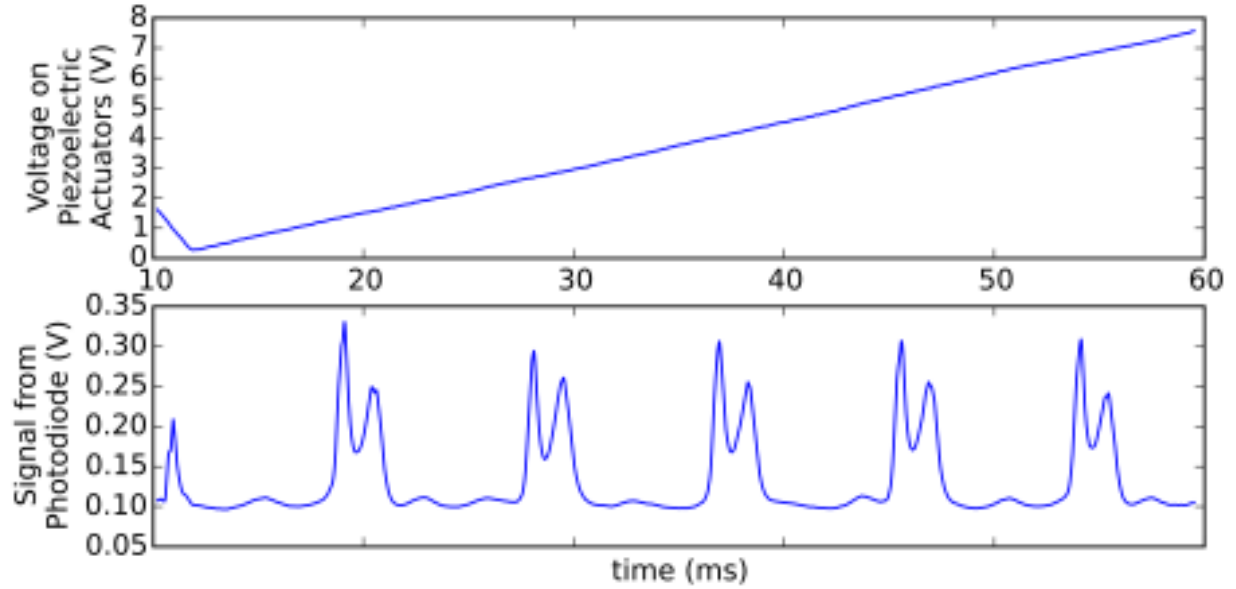
Figure 2.5 Sample data from the spectrum analyzer. These are two oscilloscope traces that were taken simultaneously. The data in the top graph represents the voltage across the piezoelectric actuators as a function of time. This voltage is proportional to the displacement of the cavity's entrance mirror. The data on the bottom graph represents the signal from the photodiode as measured across some resistance. This particular data was taken with two lasers coupled to the cavity. The peaks in the signal correspond to the moments in time when the cavity length was such that one or the other of the lasers was in resonance with the cavity. The pattern of resonances can be seen to clearly repeat itself with a well-defined period as the laser scans. The period over which the pattern repeats corresponds to the free spectral range of the cavity.

$f -$ FSR light, we should now find that we are also resonant with the $m + 1$ order mode of the light with frequency f. Therefore, the change in the cavity length between the m order modes of the light at frequency f and $f -$ FSR equals the change in the cavity length required to go between the m and $m + 1$ order modes of just the light at frequency f.

If we assume that the changes in cavity length are sufficiently small, the resonant frequencies of the cavity vary linearly as a function of change of cavity length. Therefore, using the information from the above paragraph, we can conclude that the period over which any resonance pattern on the spectrum analyzer repeats equals the free spectral range of the cavity, regardless of the exact spectral composition of the coupled light. This allows us to talk about the data from the spectrum analyzer in terms of real frequencies. The resonances of cavities and the validity of these approximations are explored in more detail in Appendix C.

The ability to analyze data from the spectrum analyzer in terms of real frequencies enables us to perform many types of measurements. For example, I can use the spectrum analyzer to place upper limits on the linewidth of the lasers by simply looking at the widths of the resonant peaks as a fraction of the spacing between adjacent identical peaks. The linewidth measured in this way is guaranteed to be larger than the actual linewidth of the laser (in practice, we would expect it to be much larger since the resonances of the cavity themselves are fairly wide). The spectrum analyzer can also be used to measure small shifts in frequency. The shift in any given peak's location as a fraction of the period over which the resonant pattern repeats itself is equal to the frequency shift of the peak as a fraction of the free spectral range. In Chapter 7, these concepts will be used to verify that the slave lasers track with the master laser by showing that the peaks corresponding to both the master laser and the slave laser move together and stay a fixed distance apart. Also in Chapter 7, I will show that the frequency difference between the two slaves depends in the correct way on the frequency of the signal used to drive the AOM.

Chapter 3

The Atoms

The objective of this chapter is to find the intensity and beam waist that will allow our lasers to impart the π and $\pi/2$ pulses to the atoms as they make their way through the chamber. In order to show that the 408 nm 5 GHz detuned laser can provide the π and $\pi/2$ pulses, one must first take a detailed look at the Raman transitions that the laser system is intended to stimulate. The basic steps that will be explained in this chapter are as follows:

- Model the dynamics of a generic three state atom undergoing a Raman transition.

- Identify the relevant contributions to the $^{87}\text{Sr}^+$ ions' Hamiltonian and show that it can be modeled as a three state system.

- Find and interpret appropriate numerical values for relevant physical parameters in the Hamiltonian.

- Calculate the intensity, width and polarization of our laser beams that will allow the laser to impart the π and $\pi/2$ pulses to the atom.

In this way I will show that the beams from this laser system will be able to accomplish their intended purpose.

3.1   Dynamics of two- and three-state systems

First, we will model the dynamics of the system based on information found in Refs. [5], [36], [37], [1] and [38]. We will eventually model the atom as a three-state system that undergoes stimulated Raman transitions. During these transitions, the atom moves coherently between the ground and excited states. In appropriate limits, however, the three-state system under-going Raman transitions can be shown to be equivalent to a two-state system undergoing Rabi oscillations between the ground and excited states. Therefore, we will first review Rabi flopping in a two state system, after which we will discuss the dynamics of a three-state system.

3.1.1   Two state Rabi oscillations

The first step to understanding the physics of the Raman transitions is to understand the dynamics of a two state atom. The dynamics of this system are well-known. Discussions of it can be found in many places, including Refs. [39], [40], and [5]. The Hamiltonian for a two level atom under periodic perturbation from an electric field can be written as

$$H = \hbar\omega_e|e\rangle\langle e| + \hbar\omega_g|g\rangle\langle g| - \mathbf{d}\cdot\mathbf{E}, \tag{3.1}$$

where ω_e and ω_g are the frequencies of the excited and ground states respectively and $\mathbf{d}$ is the dipole moment operator. The excited state is shown as $|e\rangle$, while $|g\rangle$ represents the ground state. The electric field $\mathbf{E}$ is given by

$$\mathbf{E} = \mathbf{E_0}\cos(\omega t + \phi). \tag{3.2}$$

Here, $\mathbf{E_0}$ represents the electric field amplitude and direction, while ω is the angular frequency of the laser, t is time and ϕ encapsulates the phase of the radiation. We have followed the conventions selected in Ref. [5]. These equations can be solved by moving into the interaction

picture, applying the rotating wave approximation, and diagonalizing the resulting matrix to find its eigenvalues and eigenstates.

If we let

$$|\Psi(t)\rangle = c_e(t)e^{-i\omega_e t}|e\rangle + c_g e^{-i\omega_g t}|g\rangle \tag{3.3}$$

represent the Schrödinger picture solution to the equation, then the solution in the case where $c_g(0) = 1, c_e(0) = 0$ turns out to be

$$c_e(\tau) = -ie^{-i(\delta\tau/2+\phi)}\frac{\Omega_{eg}}{\Omega_r}\sin\left(\frac{\Omega_r\tau}{2}\right) \tag{3.4}$$

$$c_g(\tau) = e^{i(\delta\tau/2)}\left(\cos\left(\frac{\Omega_r\tau}{2}\right) - i\frac{\delta}{\Omega_r}\sin\left(\frac{\Omega_r\tau}{2}\right)\right), \tag{3.5}$$

where Ω_{eg} represents the on-resonance Rabi frequency, which is defined as

$$\Omega_{eg} = -\frac{\langle e|\mathbf{d}\cdot\mathbf{E}|g\rangle}{\hbar} \tag{3.6}$$

and the off-resonance Rabi frequency, Ω_r, is defined as

$$\Omega_r = \sqrt{\Omega_{eg}^2 + \delta^2}. \tag{3.7}$$

The detuning, δ, is defined as

$$\delta = \omega - (\omega_e - \omega_g). \tag{3.8}$$

Equations 3.4 and 3.5 can be squared to find the total likelihood of finding the system in a particular state as a function of time (or, alternatively, we can interpret this as the population of the upper and lower states as a function of time):

$$|c_e(\tau)|^2 = \left(\frac{\Omega_{eg}}{\Omega_r}\right)^2\sin^2\left(\frac{\Omega_r\tau}{2}\right) = \frac{\Omega_{eg}^2}{2\Omega_r^2}(1 - \cos(\Omega_r\tau)) \tag{3.9}$$

$$|c_g(\tau)|^2 = 1 - \left(1 - \frac{\delta^2}{\Omega_r^2}\right)\sin^2\left(\frac{\Omega_r\tau}{2}\right) = 1 - \frac{\Omega_{eg}^2}{2\Omega_r^2} + \left(\frac{\Omega_{eg}^2}{2\Omega_r^2}\right)\cos(\Omega_r\tau). \tag{3.10}$$

These results are also quoted from Ref. [5], whose conventions I have also adopted.

The two state Rabi system has some important properties. First, we see that the only way to move 100% of the population from the ground state to the excited state is to drive the system on-resonance (i.e. with $\delta = 0$). Second, we see that the system oscillates between populating the excited and ground states with frequency Ω_r. The stronger the coupling between the laser and the system (which is encapsulated in $\langle e|\mathbf{d} \cdot \mathbf{E}|g\rangle$), the more rapidly these oscillations occur.

π and $\pi/2$ pulses

We are particularly interested in coherently swapping the entire populations of the two states and placing the ions into an equal, coherent superposition of the two states. An interaction that coherently moves the system from one state to the other is called a π pulse. An interaction that takes the system in one state into an equal superposition of the two states is caled a $\pi/2$ pulse. This terminology comes from the Bloch sphere. In the Bloch sphere, a superposition of $|e\rangle$ and $|g\rangle$ can be represented to within an overall phase as

$$\cos\left(\frac{\theta}{2}\right)|g\rangle + e^{i\phi}\sin\left(\frac{\theta}{2}\right)|e\rangle, \tag{3.11}$$

where ϕ and θ are arbitrary angles that can be changed to represent any state. A $\pi/2$ pulse changes θ by $\pi/2$ radians, while a π pulse changes it by π radians.

There is a little more that we can say about these pulses. In the experiment, we would like a $\pi/2$ interaction with the laser to be able to take an ion in the $|g\rangle$ or $|e\rangle$ states and put it into an equal superposition of the $|g\rangle$ and $|e\rangle$ states. However, we would also like to be able to use the same pulse to take ions that are in equal superpositions of the $|e\rangle$ and $|g\rangle$ states and put them into either the ground or excited states.

We let A be an operator representing a $\pi/2$ pulse that satisfies the above properties.

Then the effect of A on a state $|g\rangle$ is given by

$$A|g\rangle = \frac{e^{i\phi_o}}{\sqrt{2}} \left(|g\rangle + e^{i\phi_e}|e\rangle \right), \tag{3.12}$$

where ϕ_o and ϕ_e in this equation represent arbitrary constants. Now, if we apply A again, we would like to have 100% of the population moved to the excited state (i.e. A^2 is equivalent to a π pulse):

$$A^2|g\rangle = e^{i\phi_e'}|e\rangle \tag{3.13}$$

Now, substituting the result of Eq. (3.12), we get

$$A\frac{e^{i\phi_o}}{\sqrt{2}} \left(|g\rangle + e^{i\phi_e}|e\rangle \right) = e^{i\phi_e'}|e\rangle. \tag{3.14}$$

We can use the result of Eq. (3.12) again to get

$$\frac{e^{2i\phi_o}}{2}|g\rangle + \frac{e^{i(2\phi_o+\phi_e)}}{2}|e\rangle + \frac{e^{i(\phi_o+\phi_e)}}{\sqrt{2}}A|e\rangle = e^{i\phi_e'}|e\rangle. \tag{3.15}$$

We can solve this equation to find $A|e\rangle$:

$$A|e\rangle = \frac{\sqrt{2}}{e^{i(\phi_o+\phi_e)}} \left(-\frac{e^{2i\phi_o}}{2}|g\rangle + \left(e^{i\phi_e'} - \frac{e^{i(2\phi_o+\phi_e)}}{2} \right) |e\rangle \right) \tag{3.16}$$

$$A|e\rangle = -\frac{e^{i(\phi_o-\phi_e)}}{\sqrt{2}}|g\rangle + \left(\sqrt{2}e^{i(\phi_e'-\phi_e-\phi_o)} - \frac{e^{i\phi_o}}{\sqrt{2}} \right) |e\rangle. \tag{3.17}$$

Since A preserves normalization, we know that the sum of the norms of the coefficients of $|e\rangle$ and $|g\rangle$ must be one. Therefore,

$$\left| -\frac{e^{i(\phi_o-\phi_e)}}{\sqrt{2}} \right|^2 + \left| \sqrt{2}e^{i(\phi_e'-\phi_e-\phi_o)} - \frac{e^{i\phi_o}}{\sqrt{2}} \right|^2 = 1. \tag{3.18}$$

From this, we can solve to find that

$$\cos \left(\phi_e' - \phi_e - 2\phi_o \right) = 1. \tag{3.19}$$

Therefore,

$$\phi_e' - \phi_e = 2\phi_o. \tag{3.20}$$

By substituting Eq. (3.20) into Eq. (3.17), we get

$$A|e\rangle = \frac{e^{i\phi_o}}{\sqrt{2}} \left(-e^{-i\phi_e}|g\rangle + |e\rangle\right). \tag{3.21}$$

Now, we know how A acts on both $|e\rangle$ and $|g\rangle$, but we would like to figure out when we can expect to be able to apply A and get a transition from an equal superposition of $|e\rangle$ and $|g\rangle$ states to a pure $|e\rangle$ or $|g\rangle$ state. If we allow A to act on an arbitrary superposition with coefficients a_e and a_g, then we get

$$A\left(a_g|g\rangle + a_e|e\rangle\right) = \frac{e^{i\phi_o}}{\sqrt{2}} \left((a_g - a_e e^{-i\phi_e})|g\rangle + (a_e + a_g e^{i\phi_e})|e\rangle\right). \tag{3.22}$$

Thus, in order to get $A\left(a_g|g\rangle + a_e|e\rangle\right) = e^{i\gamma}|e\rangle$ (with γ an arbitrary phase),

$$\begin{aligned}\frac{e^{i\phi_o}}{\sqrt{2}} \left(a_e + a_g e^{i\phi_e}\right) &= e^{i\gamma} \\ \frac{e^{i\phi_o}}{\sqrt{2}} \left(a_g - a_e e^{-i\phi_e}\right) &= 0\end{aligned} \quad\Longrightarrow\quad \begin{aligned}a_e &= \frac{e^{i(\gamma-\phi_o)}}{\sqrt{2}} \\ a_g &= \frac{e^{i(\gamma-\phi_o-\phi_e)}}{\sqrt{2}}.\end{aligned} \tag{3.23}$$

Similarly, to get $A\left(a_g|g\rangle + a_e|e\rangle\right) = e^{i\gamma}|g\rangle$,

$$\begin{aligned}\frac{e^{i\phi_o}}{\sqrt{2}} \left(a_e + a_g e^{i\phi_e}\right) &= 0 \\ \frac{e^{i\phi_o}}{\sqrt{2}} \left(a_g - a_e e^{-i\phi_e}\right) &= e^{i\gamma}\end{aligned} \quad\Longrightarrow\quad \begin{aligned}a_g &= \frac{e^{i(\gamma-\phi_o)}}{\sqrt{2}} \\ a_e &= -\frac{e^{i(\gamma-\phi_o+\phi_e)}}{\sqrt{2}}.\end{aligned} \tag{3.24}$$

Thus, in order for a $\pi/2$ pulse to put ions that are already in a superposition into one state or the other, it must be the case that

$$|a_e|^2 = |a_g|^2 = \frac{1}{2}. \tag{3.25}$$

In addition, the phase difference between the two states determines whether we can put that superposition state into a single state and which state the $\pi/2$ pulse will put the ions in. We now consider an equal superposition of the $|e\rangle$ and $|g\rangle$ states. We arbitrarily and without loss of generality select the overall phase by allowing a_g to be real and we allow the relative

phase between the a_e and a_g coefficients to be $\Delta\phi$. Under these conditions, a_e and a_g take the form

$$a_e = \frac{e^{i\Delta\phi}}{\sqrt{2}} \tag{3.26}$$

$$a_g = \frac{1}{\sqrt{2}}. \tag{3.27}$$

Plugging this into Eq. (3.22), we see that

$$A\left(\frac{e^{i\Delta\phi}}{\sqrt{2}}|e\rangle + \frac{1}{\sqrt{2}}|g\rangle\right) = \left(\frac{1}{\sqrt{2}} - \frac{e^{i(\Delta\phi-\phi_e)}}{\sqrt{2}}\right)|g\rangle + \left(\frac{e^{i\Delta\phi}}{\sqrt{2}} + \frac{e^{i\phi_e}}{\sqrt{2}}\right)|e\rangle. \tag{3.28}$$

We can take the norm of the coefficients on the right hand side of Eq. 3.28 to see that the populations in each state are

$$\text{population in } |g\rangle \text{ state} = 1 - \cos(\Delta\phi - \phi_e) \tag{3.29}$$

$$\text{population in } |e\rangle \text{ state} = 1 + \cos(\Delta\phi - \phi_e). \tag{3.30}$$

This is handy because at the end of the interferometer, we hope to be able to detect the accumulated phase difference between the two beams. Equations 3.29 and 3.30 show that the relative phase between the two states when they are in an equal superposition will correspond to the populations in each state after the ions undergo a $\pi/2$ pulse.

3.1.2 Three state system

We now move to a discussion of the dynamics of a three state system, as shown in Figure 3.1. Following Ref. [5], we write our Hamiltonian as

$$H_{\text{tot}} = H + V. \tag{3.31}$$

Here, H is the Hamiltonian of the atom without the influence of the radiation from the laser. The symbol V represents the interaction between the atom and the laser.
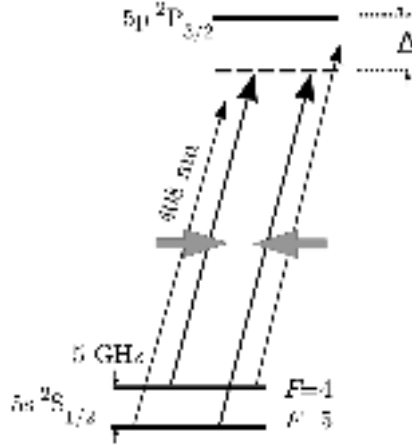
Figure 3.1 Energy Level Diagram for ^{87}Sr+. The hyperfine ground states are separated by a small energy. Diagram is not to scale: a scaled diagram would show the splitting between the $F = 4$ and $F = 5$ states to be about 147,000 times smaller than the splitting between the ^{2}S$_{1/2}$ states and the ^{2}P$_{3/2}$ states.

For present purposes, we neglect all but three states of H ($|e\rangle$,$|g_0\rangle$,and $|i\rangle$). We write H as

$$H = \hbar\omega_e|e\rangle\langle e| + \hbar\omega_g|g\rangle\langle g| + \hbar\omega_i|i\rangle\langle i| \tag{3.32}$$

Here, $|e\rangle$,$|g\rangle$, and $|i\rangle$ represent particular internal states of the atom. The state $|i\rangle$ is the "intermediate state" and is higher in energy than $|e\rangle$ or $|g\rangle$, which are the two states where we hope and expect to have population buildup. They are all eigenstates of H. In Section 3.3 we will show that $|e\rangle$ can represent the $F = 4$,$m_f = 0$,^{2}S$_{1/2}$ state, $|g\rangle$ can represent the $F = 5$,$m_f = 0$,^{2}S$_{1/2}$ state, and $|i\rangle$ can represent the $F = 5$,$m_f = 1$,^{2}P$_{3/2}$ state[1]. See Figure 3.1. The energies of these states are represented by $\hbar\omega_e, \hbar\omega_g$, and $\hbar\omega_i$ respectively.

The term representing the interaction between the laser and the ions is given by

$$V = -\mathbf{d} \cdot \mathbf{E}. \tag{3.33}$$

---

[1]Our analysis applies equally well to other sets of three states within the ions. We can select which states are involved by adjusting the tuning and polarization of the lasers.

We model the laser as a classical, oscillating electric field, $\mathbf{E}$, while $\mathbf{d}$ represents the dipole moment matrix operator of our atomic system. The electric field at the location of our atom takes the form

$$\mathbf{E} = \frac{1}{2}\left(\mathbf{E_1}e^{i\omega_1 t} + \mathbf{E_2}e^{i\omega_2 t} + c.c.\right). \tag{3.34}$$

Here, $\mathbf{E_1}$ and $\mathbf{E_2}$ are complex vectors containing the electric field magnitude, polarization, and relative phase information for two different lasers that oscillate with angular frequencies ω_1 and ω_2 respectively. The symbol $c.c.$ should be taken to mean the complex conjugate of all the terms that came before. We choose to let $\omega_1 > \omega_2$. Thus, in our convention, the laser with electric field $\mathbf{E_1}$ that oscillates at frequency ω_1 is tuned closer to the transition between $|g\rangle$ and $|i\rangle$, while the $\mathbf{E_2}, \omega_2$ laser is tuned closer to the transitions involving $|e\rangle$ and $|i\rangle$. Conveniently, this numbering matches both the conventions in Ref. [5] and it matches the numbering scheme of the slave lasers that is used in Chapter 2 (i.e. slave 1 outputs a higher frequency than slave 2).

The dipole moment matrix operator represents the coupling between the laser and the atomic system. The physical details of the dipole moment matrix operator as it relates to the $^{87}Sr^+$ ions will be addressed in Section 3.2.3. However, for now, we make a few physically valid assumptions to simplify our analysis. First, we note that by writing the interaction between the lasers and the atoms in the form $\mathbf{d} \cdot \mathbf{E}$, we have already assumed that the electric field produced by both lasers is uniform in the regime of the atoms. This is known as the "electric dipole approximation." Second, we now assume that all of the on-diagonal dipole moment matrix elements are zero [39]. Finally, we neglect any possible coupling betweeen $|e\rangle$ and $|g\rangle$. That is to say that $\langle e|\mathbf{d} \cdot \mathbf{E}|g\rangle = 0$, or that V only couples $|e\rangle$ and $|g\rangle$ to the excited state $|i\rangle$. This assumption is justified by the fact that, first of all, in our particular ions, it works out that $|e\rangle$ and $|g\rangle$ are not dipole-allowed transitions. However, we also note that the laser will be at such a frequency that even states that are dipole allowed will not

have any light close enough to their resonances to make them want to transition. Therefore, we expect to be able to write the dipole matrix element operator as

$$
V = \begin{array}{c} \\ |e\rangle \\ |g\rangle \\ |i\rangle \end{array}
\begin{array}{ccc} \langle e| & \langle g| & \langle i| \\ \left[\begin{array}{ccc} 0 & 0 & \langle e|\mathbf{d}\cdot\mathbf{E}|i\rangle \\ 0 & 0 & \langle g|\mathbf{d}\cdot\mathbf{E}|i\rangle \\ \langle i|\mathbf{d}\cdot\mathbf{E}|e\rangle & \langle i|\mathbf{d}\cdot\mathbf{E}|g\rangle & 0 \end{array} \right]. \end{array}
\tag{3.35}
$$

Here, we have used the basis $|e\rangle, |g\rangle, |i\rangle$. The columns and rows are labeled accordingly. It is convenient to define the one photon, on-resonance Rabi frequencies:

$$
\Omega_e = -\frac{\langle i|\mathbf{d}\cdot\mathbf{E}_2|e\rangle}{\hbar} \tag{3.36}
$$

$$
\Omega_g = -\frac{\langle i|\mathbf{d}\cdot\mathbf{E}_1|g\rangle}{\hbar}. \tag{3.37}
$$

Now V can be written slightly more concisely as

$$
V = -\hbar \begin{array}{c} \\ |e\rangle \\ |g\rangle \\ |i\rangle \end{array}
\begin{array}{ccc} \langle e| & \langle g| & \langle i| \\ \left[\begin{array}{ccc} 0 & 0 & \Omega_e^* \\ 0 & 0 & \Omega_g^* \\ \Omega_e & \Omega_g & 0 \end{array} \right]. \end{array}
\tag{3.38}
$$

Transformation to interaction picture

First, we move to the interaction picture. Information on the interaction picture and the basics of quantum dynamics can be found in Refs. [41] and [42]. Moving to the interaction picture is analagous to moving to a so-called "rotating frame" as is done in Ref. [5].The

interaction picture is related to the Schrödinger picture by the following transformations:

$$|e\rangle_I = e^{iH_0 t/\hbar}|e\rangle \tag{3.39}$$

$$|g\rangle_I = e^{iH_0 t/\hbar}|g\rangle \tag{3.40}$$

$$|i\rangle_I = e^{iH_0 t/\hbar}|i\rangle \tag{3.41}$$

$$V_I = e^{iH_0 t/\hbar} V e^{-iH_0 t/\hbar}. \tag{3.42}$$

In general, we may let $|\psi\rangle$ represent any generic state in the Schrödinger picture and $|\psi\rangle_I = \exp(iH_0 t/\hbar)|e\rangle$ represent the interaction picture version of the state. The equations of motion satisfied by the states is

$$i\hbar \frac{\partial}{\partial t}|\psi\rangle_I = V_I|\psi\rangle_I. \tag{3.43}$$

Note that in the basis $|e\rangle, |g\rangle, |i\rangle$, we can write $\exp(iH_0 t/\hbar)$ as

$$\exp(iH_0 t/\hbar) = e^{i\omega_e t}|e\rangle\langle e| + e^{i\omega_g t}|g\rangle\langle g| + e^{i\omega_i t}|i\rangle\langle i|. \tag{3.44}$$

This has the effect of moving the trivial evolution of the ion into the operators and allowing the stationary states of H to have no time-dependent phase. Now, the state of the system may be written as

$$|\psi(t)\rangle_I = c_e(t)|e\rangle_I + c_g(t)|g\rangle_I + c_i(t)|i\rangle_I, \tag{3.45}$$

where c_e, c_g, c_i are coefficients that change relatively slowly compared to the laser frequencies ω_1 and ω_2.

Rotating wave approximation

In order to solve for the dynamics, we must apply the rotating wave approximation. In order to do this, we first rewrite $\mathbf{E}$ from Eq. 3.34 as

$$\mathbf{E} = \mathbf{E_1} \frac{\exp(i(\omega_1 t + \phi_1)) + \exp(-i(\omega_1 t + \phi_1))}{2}$$
$$+ \mathbf{E_2} \frac{\exp(i(\omega_2 t + \phi_2)) + \exp(-i(\omega_2 t + \phi_2))}{2}, \tag{3.46}$$

Frequencies	Definition and comment
ω_1, ω_2	Laser frequencies
δ	Two photon detuning, $\delta = (\omega_e - \omega_g) - (\omega_1 - \omega_2)$
$\Delta, \Delta_{1g}, \Delta_{2e}$	One photon detunings, $\Delta \approx \Delta_{1g} = \omega_i - \omega_g - \omega_1 \approx \Delta_{2e} = \omega_i - \omega_e - \omega_2$
Ω_e, Ω_g	On-resonance single-photon Rabi frequencies.
Ω_r	Off-resonance Rabi frequency for two photon transition.
Ω_{eff}	Effective Rabi frequency for two photon transition.

Table 3.1 Frequencies used in this derivation. Note that $\omega_1, \omega_2 \gg \delta \gg \Delta$.

which means that the first few terms of V_I can be written in the interaction picture as

$$V_I = \frac{1}{2} e^{i(\omega_e - \omega_i + \omega_1)t + \phi_1} |e\rangle\langle e| \mathbf{d} \cdot \mathbf{E}_1 |i\rangle\langle i| + \frac{1}{2} e^{i(\omega_e - \omega_i - \omega_1)t - \phi_1} |e\rangle\langle e| \mathbf{d} \cdot \mathbf{E}_1 |i\rangle\langle i|$$

$$+ \frac{1}{2} e^{i(\omega_e - \omega_i + \omega_2)t + \phi_2} |e\rangle\langle e| \mathbf{d} \cdot \mathbf{E}_2 |i\rangle\langle i| + \frac{1}{2} e^{i(\omega_e - \omega_i - \omega_2)t - \phi_2} |e\rangle\langle e| \mathbf{d} \cdot \mathbf{E}_2 |i\rangle\langle i| + \dots \quad (3.47)$$

The rotating wave approximation is to assume that only the slowly-oscillating terms will make non-zero contributions to the dynamics of the system. The only terms where this criterion is satisfied are the ones near our resonances. We have assumed that $\omega_i - \omega_g \approx \omega_1$ and that $\omega_i - \omega_e \approx \omega_2$, which means that our new V_I with the rotating wave approximation applied is

$$V_I = \frac{1}{2} e^{i(\omega_i - \omega_g - \omega_1)t + \phi_1} |i\rangle\langle i| \mathbf{d} \cdot \mathbf{E}_1 |g\rangle\langle g| + \frac{1}{2} e^{i(\omega_g - \omega_i + \omega_1)t - \phi_1} |g\rangle\langle g| \mathbf{d} \cdot \mathbf{E}_1 |i\rangle\langle i|$$

$$+ \frac{1}{2} e^{i(\omega_i - \omega_e - \omega_2)t + \phi_2} |i\rangle\langle i| \mathbf{d} \cdot \mathbf{E}_2 |e\rangle\langle e| + \frac{1}{2} e^{i(\omega_e - \omega_i + \omega_2)t - \phi_2} |e\rangle\langle e| \mathbf{d} \cdot \mathbf{E}_2 |i\rangle\langle i| \quad (3.48)$$

For convenience, we define the following frequencies:

$$\Delta_{1g} = \omega_i - \omega_g - \omega_1 \quad (3.49)$$

$$\Delta_{2e} = \omega_i - \omega_e - \omega_2 \quad (3.50)$$

$$\delta = (\omega_e - \omega_g) - (\omega_1 - \omega_2). \quad (3.51)$$

(Table 3.1 summarizes most of the relevant frequencies we have defined.) We assume that $\delta \ll \Delta_{1g}$ and that $\delta \ll \Delta_{2e}$, or in other words that $\Delta_{1g} \approx \Delta_{2e}$.

We can write V_I explicitly using Eqs. (3.47), (3.49), (3.38), (3.36), and (3.37):

$$
V_I = \hbar
\begin{bmatrix}
0 & 0 & -\frac{\Omega_e^*}{2}e^{-i\Delta_{2e}t} \\
0 & 0 & -\frac{\Omega_g^*}{2}e^{-i\Delta_{1g}t} \\
-\frac{\Omega_e}{2}e^{i\Delta_{2e}t} & -\frac{\Omega_g}{2}e^{i\Delta_{1g}t} & 0
\end{bmatrix}.
\tag{3.52}
$$

Adiabatic elimination of $|i\rangle$ state

In order to solve the system, we use adiabatic elimination to make this look like the two state system. There are several ways to do this. One method is to write the solution as

$$
|\psi\rangle =
\begin{bmatrix}
c_e(t) \\
c_g(t) \\
c_i(t)
\end{bmatrix},
\tag{3.53}
$$

then find the three coupled differential equations that describe the evolution of the sytem and solve them assuming that $\frac{\partial c_i(t)}{\partial t} = 0$. There are some subtleties to this method [2] that are well-explained in Ref. [43]. In fact, Ref. [43] gives an excellent discussion of adiabatic elimination for a three state system like ours.

We can also motivate our use of the two state equations of motion using time-dependent perturbation theory. If we take the standard, time-dependent perturbation to second order, we get

$$
U_I(t) = \mathbb{1} - \frac{i}{\hbar}\int_{t_0}^t dt' V_I(t') + \left(-\frac{i}{\hbar}\right)^2 \int_{t_0}^t dt' V_I(t') \int_{t_0}^{t'} dt'' V_I(t'').
\tag{3.54}
$$

---

[2]For example, if we had defined our coefficients in terms of the basis vectors of the interaction picture (i.e. so that $|\psi\rangle_I = c_{e,I}(t)e^{-iHt/\hbar}|e\rangle + c_{g,I}(t)e^{-iHt/\hbar}|g\rangle + c_{i,I}(t)e^{-iHt/\hbar}|i\rangle$), assuming that $\dot{c}_{i,I} = 0$ would not give the right answer.

The symbol $U_I(t)$ represents the time evolution operator. If we use Eq. (3.52) to write V_I in its matrix form, Eq. (3.54) becomes

$$U_I(t) = \mathbb{1} + i \int_{t_0}^{t} dt' \begin{bmatrix} 0 & 0 & \frac{\Omega_e^*}{2}e^{-i\Delta_{2e}t} \\ 0 & 0 & \frac{\Omega_g^*}{2}e^{-i\Delta_{1g}t} \\ \frac{\Omega_e}{2}e^{i\Delta_{2e}t} & \frac{\Omega_g}{2}e^{i\Delta_{1g}t} & 0 \end{bmatrix} +$$

$$\int_{t_0}^{t} dt' \int_{t_0}^{t'} dt'' \begin{bmatrix} 0 & 0 & \frac{\Omega_e^*}{2}e^{-i\Delta_{2e}t'} \\ 0 & 0 & \frac{\Omega_g^*}{2}e^{-i\Delta_{1g}t'} \\ \frac{\Omega_e}{2}e^{i\Delta_{2e}t'} & \frac{\Omega_g}{2}e^{i\Delta_{1g}t'} & 0 \end{bmatrix} \begin{bmatrix} 0 & 0 & \frac{\Omega_e^*}{2}e^{-i\Delta_{2e}t''} \\ 0 & 0 & \frac{\Omega_g^*}{2}e^{-i\Delta_{1g}t''} \\ \frac{\Omega_e}{2}e^{i\Delta_{2e}t''} & \frac{\Omega_g}{2}e^{i\Delta_{1g}t''} & 0 \end{bmatrix}, \quad (3.55)$$

which reduces to

$$U_I(t) = \mathbb{1} + i \int_{t_0}^{t} dt' \begin{bmatrix} 0 & 0 & \frac{\Omega_e^*}{2}e^{-i\Delta_{2e}t'} \\ 0 & 0 & \frac{\Omega_g^*}{2}e^{-i\Delta_{1g}t'} \\ \frac{\Omega_e}{2}e^{i\Delta_{2e}t'} & \frac{\Omega_g}{2}e^{i\Delta_{1g}t'} & 0 \end{bmatrix} +$$

$$\int_{t_0}^{t} dt' \int_{t_0}^{t'} dt'' \begin{bmatrix} \frac{|\Omega_e|^2}{4}e^{i\Delta_{2e}(t''-t')} & \frac{\Omega_g\Omega_e^*}{4}e^{i(\Delta_{1g}t''-\Delta_{2e}t')} & 0 \\ \frac{\Omega_g^*\Omega_e}{4}e^{i(\Delta_{2e}t''-\Delta_{1g}t')} & \frac{|\Omega_g|^2}{4}e^{i\Delta_{1g}(t''-t')} & 0 \\ 0 & 0 & \frac{|\Omega_e|^2}{4}e^{i\Delta_{2e}(t'-t'')} + \frac{|\Omega_g|^2}{4}e^{i\Delta_{1g}(t'-t'')} \end{bmatrix}.$$

$$(3.56)$$

After carrying out the integration in the variable t'', we end up with the following:

$$U_I(t) = \mathbb{1} + i \int_{t_0}^{t} dt' \begin{bmatrix} 0 & 0 & \frac{\Omega_e^*}{2}e^{-i\Delta_{2e}t} \\ 0 & 0 & \frac{\Omega_g^*}{2}e^{-i\Delta_{1g}t} \\ \frac{\Omega_e}{2}e^{i\Delta_{2e}t} & \frac{\Omega_g}{2}e^{i\Delta_{1g}t} & 0 \end{bmatrix} +$$

$$\int_{t_0}^{t} dt' \begin{bmatrix} \frac{|\Omega_e|^2}{4i\Delta_{2e}}\left(e^{i\Delta_{2e}(t'-t')} - e^{i\Delta_{2e}(t_0-t')}\right) & \frac{\Omega_g\Omega_e^*}{4i\Delta_{1g}}\left(e^{i(\Delta_{1g}-\Delta_{2e})t'} - e^{i(\Delta_{1g}t_0-\Delta_{2e}t')}\right) & 0 \\ \frac{\Omega_g^*\Omega_e}{4i\Delta_{2e}}\left(e^{i(\Delta_{2e}-\Delta_{1g})t'} - e^{i(\Delta_{2e}t_0-\Delta_{1g}t')}\right) & \frac{|\Omega_g|^2}{4i\Delta_{1g}}\left(e^{i\Delta_{1g}(t'-t')} - e^{i\Delta_{1g}(t_0-t')}\right) & 0 \\ 0 & 0 & \begin{matrix}\frac{|\Omega_e|^2}{4i\Delta_{2e}}\left(e^{i\Delta_{2e}(t'-t')} - e^{i\Delta_{2e}(t'-t_0)}\right)+ \\ \frac{|\Omega_g|^2}{4i\Delta_{1g}}\left(e^{i\Delta_{1g}(t'-t')} - e^{i\Delta_{1g}(t'-t_0)}\right)\end{matrix} \end{bmatrix} .$$

$$(3.57)$$

We now argue that the many terms in this integral that oscillate with frequencies near $\Delta_{2e} \approx \Delta_{1g}$ can be neglected. Instead, we assume that the main contributions will be from the terms that oscillate with frequencies of 0 or $\Delta_{1g} - \Delta_{2e}$ (which is much smaller than Δ_{2e} and Δ_{1g}). The reasoning is that the terms that oscillate near Δ will oscillate through many periods over timescales over which the other terms will be more or less constant. Therefore, we can expect that for the purposes of integrating, the high frequency contributions will be approximately 0.

After removing the terms we are neglecting from Eq. (3.57) and making the substitutions $\Delta_{2e} - \Delta_{1g} \to \delta$, $\Delta_{2e} \to \Delta$, $\Delta_{1g} \to \Delta$ (we note that δ is small), we end up with

$$U_I(t) = \mathbb{1} - i \int_{t_0}^{t} dt' \begin{bmatrix} \frac{|\Omega_e|^2}{4\Delta} & \frac{\Omega_g\Omega_e^*}{4\Delta}e^{-i\delta t'} & 0 \\ \frac{\Omega_g^*\Omega_e}{4\Delta}e^{i\delta t'} & \frac{|\Omega_g|^2}{4\Delta} & 0 \\ 0 & 0 & \frac{|\Omega_e|^2}{4\Delta} + \frac{|\Omega_g|^2}{4\Delta} \end{bmatrix} \quad (3.58)$$

Now, we notice that this very closely resembles the *first*-order Dyson series we would have gotten if we had had a different V_I, namely

$$V_I = \hbar \begin{bmatrix} \frac{|\Omega_e|^2}{4\Delta} & \frac{\Omega_g\Omega_e^*}{4\Delta}e^{-i\delta t'} & 0 \\ \frac{\Omega_g^*\Omega_e}{4\Delta}e^{i\delta t'} & \frac{|\Omega_g|^2}{4\Delta} & 0 \\ 0 & 0 & \frac{|\Omega_e|^2}{4\Delta} + \frac{|\Omega_g|^2}{4\Delta} \end{bmatrix} . \quad (3.59)$$

We notice that in the limit we have selected, our new V_I no longer has any terms that might couple a long-term population to the intermediate state $|i\rangle$. Therefore, we will adopt a truncated version of Eq. (3.59) as our interaction Hamiltonian. What I have presented is not an airtight argument, but the result is correct. Alternative justifications for this can be found in several places, most helpfully in Ref. [43].

We will now treat this like a two-state system, so from now on we let

$$V_I = \hbar \begin{array}{c} \langle e| \qquad\qquad \langle g| \\ \begin{array}{c} |e\rangle \\ |g\rangle \end{array} \left[\begin{array}{cc} \frac{|\Omega_e|^2}{4\Delta} & \frac{\Omega_g\Omega_e^*}{4\Delta}e^{-i\delta t'} \\ \frac{\Omega_g^*\Omega_e}{4\Delta}e^{i\delta t'} & \frac{|\Omega_g|^2}{4\Delta} \end{array} \right]. \end{array} \tag{3.60}$$

Now, the solution to this equation is very similar to the solution to the two state system discussed in 3.1.1. Here, the quantity analagous to the off-resonance Rabi frequency is given by [5]:

$$\Omega_r = \sqrt{\Omega_{\text{eff}}^2 + (\delta - \delta^{AC})^2}, \tag{3.61}$$

where $\delta^{AC} = \frac{|\Omega_e|^2}{4\Delta} - \frac{|\Omega_g|^2}{4\Delta}$. This frequency accounts for the AC Stark shifts that appeared in Eq.(3.60). Also, Ω_{eff} is the effective on-resonance Rabi frequency given by

$$\Omega_{\text{eff}} = \frac{\Omega_e^*\Omega_g}{2\Delta}. \tag{3.62}$$

Following the analysis of a two-state system, it can be shown that the population in our two states for the case where $|c_g(\tau = 0)|^2 = 1$ and $|c_e(\tau = 0)|^2 = 0$ is given by

$$|c_e(\tau)|^2 = \frac{\Omega_{\text{eff}}^2}{2\Omega_r^2}(1 - \cos(\Omega_r\tau)) \tag{3.63}$$

$$|c_g(\tau)|^2 = 1 - \frac{\Omega_{\text{eff}}^2}{2\Omega_r^2} + \left(\frac{\Omega_{\text{eff}}^2}{2\Omega_r^2}\right)\cos(\Omega_r\tau). \tag{3.64}$$

Here again we see that in order to coherently move the entire population, we need to ensure that $\Omega_{\text{eff}} = \Omega_r$. This can be accomplished only when $\delta - \delta_{AC} = 0$. Notice that the detuning

from the upper state Δ only affects the Rabi rate. As long as it is small enough that our approximations hold, it does not affect the total population transfer that can be achieved. However, if the off-resonance Rabi frequency gets small enough, it is possible that we will run into the practial difficulty of not having enough laser power over a large enough interaction area to effectively transfer the ion population to the desired states.

3.2 Real world $^{87}Sr^+$ Hamiltonian contributions and relevant states

In this section, we will discuss the states of the real-world Strontium ions that will be used in the experiment. We will discuss the contributions to the Hamiltonian and figure out which states are relevant to the experiment.

The Hamiltonian of the Strontium ions is analagous to the Hamiltonian of a single-electron atom. In a single electron atom, the solution to the Schrödinger equation describing the electron is solved by separation of variables. Each solution is a product of a spherically symmetric function that depends only on the distance r from the nucleus and the spherical harmonics. This is because the orbital angular momentum operator $\mathbf{L}$ commutes with such a Hamiltonian. In fact, the orbital angular momentum operator commutes with any Hamiltonian with a spherically symmetric potential. Thus, we can use the familiar angular momentum quantum numbers for the eigenstates of any spherically symmetrical Hamiltonian.

In the case of $^{87}Sr+$, there is only one electron in the valence band. The inner shells are full and we assume that the symmetry is such that the eigenstates of the atom will also be eigenstates of the orbital angular momentum operator, $\mathbf{L}$. The system also involves two other angular momentum operators: the spin operator for the valence electron, $\mathbf{S}$, and the

spin of the nucleus, **I**. (Here and throughout, we will use the boldface **I** to mean the operator while the unbolded letter (I) will mean the associated eigenvalue.)

The "good" quantum numbers for describing the internal states of a ^{87}Sr+ ion are F, J, L, S, m_f and n [44] [45] where F, J, L, S, m_f take on their usual meanings (see Table 3.2). This is because the Hamiltonian for the unperturbed atom is diagonal in this basis. Equivalently, it is because these operators all commute with one another and with the other pieces of the Hamiltonian. However, a few of the external stimuli to the ions (like the constant magnetic field or the interaction of the lasers) can be most naturally modelled in terms of the eigenstates of the L, m_l, S, m_s, I, m_I quantum numbers.

Quantum Number	Definition and comment
L	Orbital angular momentum of valence electron.
S	Spin of valence electron. Takes on values $\pm 1/2$
I	Nuclear spin. For ^{87}Sr$^+$, $I = 9/2$
J	Total valence electron angular momentum. $\mathbf{J} = \mathbf{L} + \mathbf{S}$
F	Total angular momentum $\mathbf{F} = \mathbf{I} + \mathbf{J}$
m_f	Eigenvalue of $\mathbf{F}_z$.

Table 3.2 The quantum numbers used to describe the internal state of the ^{87}Sr+ ion.

There are two basic things we have to do in this section. First, we must account for each of the contributions to the Hamiltonian of the ions. We will write the Hamiltonian as

$$H = H_0 + H_{\text{hfs}} + H_{\text{Z}}, \tag{3.65}$$

where H represents the Hamiltonian of the ion while it is *unperturbed* by the laser. The contribution to the Hamiltonian due to the hyperfine splitting is encapsulated in H_{hfs}, while H_{Z} represents the contribution that Zeeman shifts make to the Hamiltonian. (We create a

constant, but adjustable magnetic field through which the atoms travel during the experiment. We do this specifically to break degeneracies between certain of the levels in the atom as discussed in Section 3.2.2.) The rest of the Hamiltonian is represented by H_0. We do not explicitly consider other contributions to the Hamiltonian (for example, the fine structure) because these are built into the values we look up in the NIST atomic spectra database [46][3].

Second, we must find which exact states the experiment will use. Our experiment is designed to use the $^2S_{1/2}$ and $^2P_{3/2}$ states. However, each of these spectroscopic terms refers to many states: For example, we must account for the states that correspond to different values of F. Since $\mathbf{F} = \mathbf{I} + \mathbf{J}$, F can take on any values between $|I - J|, |I - J| + 1, ..., |I + J|$. So, for example, since $I = 9/2$, the valid values of F for the $^2S_{1/2}$ state are $F = 4$ and $F = 5$. For the upper states, where $J = 3/2$, F can take on the values $3, 4, 5,$ or 6. We must also take into account the many possible values of m_J and m_F for these states.

3.2.1   Review of hyperfine splitting

We now discuss the Hyperfine contribution to our overall Hamiltonian. We will need to understand the hyperfine splitting to allow us to model the 5 GHz energy difference between the $F = 4$ and $F = 5$ $^2S_{1/2}$ states. Our discussion will allow us to calculate hyperfine shifts for all the energy levels in our atom based on the hyperfine A and B coefficients, for which we have found experimental and numerical estimates in the literature.

---

[3]For example, the NIST database gives transition lifetimes for $^2S_{1/2} \rightarrow ^2P_{3/2}$ transitions. The fine structure is already accounted for, as evidenced by the fact that there is a separate entry for $^2S_{1/2} \rightarrow ^2P_{1/2}$ transitions.

Hyperfine basics

The hyperfine splitting arises from interactions between the nucleus and the electrons. The piece of the Hamiltonian representing the Hyperfine interaction is represented by the symbol H_{hfs} in Eq. (3.65). The standard expansion of H_{hfs} in the literature is:

$$H_{\mathrm{hfs}} = \sum_k \mathbf{T}^{(k)} \cdot \mathbf{M}^{(k)}, \tag{3.66}$$

where $\mathbf{T}^{(k)}$ and $\mathbf{M}^{(k)}$ are irreducible spherical tensor operators of rank k [47] [44] [48]. The dot product for spherical tensors of arbitrary rank is defined in the normal way as

$$\mathbf{T}^{(k)} \cdot \mathbf{M}^{(k)} = \sum_q (-1)^q T_q^{(k)} M_{-q}^{(k)}. \tag{3.67}$$

The tensor operator $\mathbf{T}^{(k)}$ represents information about the electron. $\mathbf{M}^{(k)}$ represents the nucleus [44] [47] [49]. Writing the expansion in this form shows explicitly the geometry of the operator.

Before discussing what information $\mathbf{T}^{(k)}$ and $\mathbf{M}^{(k)}$ represent exactly, we pause to point out a few geometrical facts. Even if we had no knowledge of the mechanism by which hyperfine interactions occur, we might still arrive at Eq. 3.66 simply by geometrical considerations. Notice that the generator of rotations under which $\mathbf{T}^{(k)}$ is valid is the electron total angular momentum, $\mathbf{J}$, while $\mathbf{M}^{(k)}$ is subject to rotations defined in terms of the nuclear angular momentum operator $\mathbf{I}$. The direct product of these two gives us a value that can be validly rotated using the group generated by the combined angular momentum operator $\mathbf{F}$. [50] [49]. Thus, each term of our expansion has two parts: one that is a valid tensor operator associated with the geometry of the nucleus and one that is a valid tensor operator associated with the geometry of the electron. By combining these two parts using a dot product, we see that each term turns out to be a valid tensor operator for the entire atomic system. This is exactly what we would expect.

The most important contributions to the Hyperfine splitting come from magnetic dipole interactions and electric quadrupole interactions [49] [47] [45]. These correspond to the $k = 1$ and $k = 2$ terms in Eq. (3.67) respectively [44].

Magnetic dipole interaction

First, we discuss the $k = 1$ term, or magnetic dipole interaction term from the expansion in Eq. (3.67). Classically, we know that the potential energy of a dipole in a magnetic field is proportional to the dot product of the magnetic dipole moment vector with the magnetic field vector ($U = -\mu \cdot \mathbf{B}$). We also know that the magnetic field at the center of a classical dipole points in the direction of the dipole moment. Therefore, it seems reasonable that the energy due to the interaction of the electron and the nucleus might be somehow proportional to a dot product of two vectors representing their respective angular momenta. Indeed, this turns out to be the case: the magnetic dipole interaction can be written as follows [49]:

$$W_f = A\mathbf{I} \cdot \mathbf{J}, \tag{3.68}$$

where W_f represents the energy associated with this coupling and A encapsulates a coupling factor between the nuclear and electronic magnetic moments.

The product $\mathbf{I} \cdot \mathbf{J}$ can be expanded by noticing that $\mathbf{F}^2 = (\mathbf{I} + \mathbf{J})^2 = \mathbf{I}^2 + 2\mathbf{I} \cdot \mathbf{J} + \mathbf{J}^2$. This gives [45] [49]:

$$W_f = \frac{1}{2}A(\mathbf{F}^2 - \mathbf{J}^2 - \mathbf{I}^2). \tag{3.69}$$

We can also see how Eq. 3.68 represents the $k = 1$ term in Eq. (3.67). We clearly have one tensor operator from the Nuclear angular momentum space ($\mathbf{I}$) along with one vector from the electron angular momentum space ($\mathbf{J}$). The product we get is a scalar that will be invariant under rotations in the total space[4].

---

[4]A quick note about constants. In the expansion in Eq. (3.67), there are different conventions [47] for

Electric quadrupole interaction

In a similar way, the $k = 2$ term in Eq. (3.67) can be shown to correspond to the electric quadrupole interaction. Chapter 6.2 of Ref. [49] gives a good explanation for this. The crux of the argument is that the electric quadrupole interaction,

$$W = \int \frac{\rho(\mathbf{r})\rho'(\mathbf{r}')}{|\mathbf{r} - \mathbf{r}'|} d\mathbf{r} d\mathbf{r}'. \tag{3.70}$$

can be expanded in terms of spherical harmonics:

$$W = \int d\mathbf{r} d\mathbf{r}' \rho(\mathbf{r})\rho'(\mathbf{r}') \sum_k \frac{r'^k}{r^{k+1}} [C^k(\theta, \phi) \cdot C^k(\theta', \phi')]. \tag{3.71}$$

The $k = 2$ term in the integral contained in Eq. 3.71 takes the form of an inner product between two rank 2 spherical tensors. Thus, we are satisfied that we have found the $k = 2$ terms in Eq. (3.67).

The inner product between two rank 2 spherical tensors can be evaluated using Eq. 4.169 from Sobelman [49] (the formula can also be found in Ref. [50] and is also referred to in Ref. [47]):

$$\langle \gamma I J F m_f | (T^{(k)} M^{(k)}) | \gamma J I F m_f \rangle$$

$$= (-1)^{F+I+J} \sum_\gamma \langle \gamma J || T^{(k)} || \gamma J \rangle \langle \gamma I || M^{(k)} || \gamma I \rangle \begin{Bmatrix} J & I & F \\ I & J & k \end{Bmatrix}, \tag{3.72}$$

where $\begin{Bmatrix} J & I & F \\ I & J & k \end{Bmatrix}$ represents the Wigner $6j$ symbol.

---

deciding which coefficients are pulled into which operators. However, as we will see, the coefficient A as used in Eq. 3.68 is defined in a standard way and can be looked up in the literature. For this reason, we are specifying T and M only up to a constant. This is fine since the point of showing the expansion is really just to make a comment about the geometry of hyperfine interactions, while the actual calculations only involve the first two terms

Using the properties of the Wigner $6j$ symbols, it can be shown that the equation for the electric quadrupole term in the hyperfine interaction takes the form [45] [49]

$$W = BC(C + 1), \tag{3.73}$$

where

$$C = F(F + 1) - J(J + 1) - I(I + 1). \tag{3.74}$$

(Interestingly, Eq. 3.69 can also be evaluated using Eq. 3.72 using $k = 1$.)

Write both hyperfine terms in terms of standard constants

We can rewrite Eq. (3.69) in terms of C and then combine it with Eq. (3.73) to get the full hyperfine splitting [45]:

$$E_{\text{hfs}} = \frac{1}{2}AC + BC(C + 1). \tag{3.75}$$

The coefficients A and B as used in Eqs. 3.75 and 3.69 are the hyperfine A and B coefficients[5]. The symbols A and B are a standard name and notation used in calculating hyperfine energy shifts. Their values can be looked up in the literature [45]. We found values for the A and B coefficients for ^{87}Sr+ in Ref. [51]. These are summarized in Table 3.3.

Calculate hyperfine energy shifts

We may calculate the splitting between the $F = 4$ and $F = 5$ ^{2}S$_{1/2}$ states using $I = 9/2$, $F = 4, 5$, $L = 0$ using Eq. 3.75. In this case, we can see that with $A = 1000$MHz, we can

---

[5]These are *not* the Einstein A and B coefficients relating to radiative transition rate. Though, unfortunately, we will have to mention the Einstein A and B coefficients later.

[6]Ref. [51] reports B/Q as 271MHz/b and also says that $Q = 0.327(24)$b. We multiplied 271MHz/b×0.327(24)b= 88.68 MHz, to get the value that appears here.

Level	$A^{\text{(SDpT)}}$	$A^{\text{(theor)}}$	$A^{\text{(expt)}}$
$5s^2\text{S}_{1/2}$	-997.85 MHz	-1000 MHz	-1000.473673(11) MHz
$5p^2\text{P}_{3/2}$	-35.26 MHz	-35.3 MHz	-36.0(04) MHz

Level	$B^{\text{(SDpT)}}$	$B^{\text{(theor)}}$	$B^{\text{(expt)}}$
$5s^2\text{S}_{1/2}$		0 MHz	
$5p^2\text{P}_{3/2}$	88.94MHz	88.68MHz[6]	88.5(54)MHz

Table 3.3 Values of A and B coefficients in MHz for relevant states taken from Ref. [51]. The label "SDpT" refers to the value calculated using one particular numerical approach as detailed in Ref. [51]. The label "theor" represents theoretically calculated values. The label "expt" refers to measured values from experiments.

calculate the splitting between the $F = 4$ and $F = 5$ levels:

$$C_{F=4} = -5.5 \tag{3.76}$$

$$C_{F=5} = 4.5 \tag{3.77}$$

$$W_{F=4} - W_{F=5} = 5000 \quad \text{MHz.} \tag{3.78}$$

Furthermore, we can calculate the hyperfine splitting for all the $^2\text{P}_{3/2}$ states, which is contained in Table 3.4.

3.2.2   Magnetic field

The next feature of our system Hamiltonian that we need to model involves the constant magnetic field pointing in the $\hat{z}$ direction that exists throughout the entire area where the interferometry will take place. This field has been placed there intentionally to break the degeneracy of some of the m_f sublevels that we might couple to. It also prevents the atoms from precessing around stray magnetic fields, which would take them out of the lab-centric coordinate system we would like to keep them in.

State	Hyperfine shift
$F = 3\ ^2\mathrm{P}_{3/2}(5p)$	22971 MHz
$F = 4\ ^2\mathrm{P}_{3/2}(5p)$	5803 MHz
$F = 5\ ^2\mathrm{P}_{3/2}(5p)$	306 MHz
$F = 6\ ^2\mathrm{P}_{3/2}(5p)$	17121 MHz

Table 3.4 Hyperfine splitting on $^2\mathrm{P}_{3/2}$ states. The Hyperfine shift represents the energy shift between the Hamiltonian neglecting hyperfine splitting and the Hamiltonian that includes it . The values are given in MHz and the associated energy is hf. Code for calculating these values can be found in Appendix E.

The energy shift due to the Zeeman interaction is simply [49]:

$$W = -\mu \cdot \mathbf{H}, \tag{3.79}$$

where μ is the magnetic dipole moment of the atom and $\mathbf{H}$ is the magnetic field strength. The magnetic moment μ for an atom without hyperfine structure can be written as [49]

$$\mu = -\mu_0 g \mathbf{J}. \tag{3.80}$$

Here μ_0 is the Bohr Magneton and g is the gyromagnetic ratio or g factor which is usually of order unity.

We note that, in contrast to H_{hfs}, which turned out to be diagonal in the F, I, J, S, m_f basis, the interaction energy due to a magnetic field pointing in the $\hat{z}$ direction is more naturally written in the I, m_I, L, m_L, S, m_S basis. This is because the field breaks the degeneracy of the m_x levels and it would be nice to be able to model the effect using the magnetic moment of the electron spin, electron orbit and nuclear spin separately.

However, we can make an approximation for the case where the Zeeman splitting is small compared to the hyperfine splitting. Ref. [49] gives us the following equation:

$$\langle \gamma JIFM|W|\gamma JIFM \rangle = \mu_0 g \frac{F(F+1) + J(J+1) - I(I+1)}{2F(F+1)} m_f H, \tag{3.81}$$

where $\mu_0 = e\hbar/(2m_e)$ and is the Bohr magneton[7]. (Here, m_e is the mass of the electron.)

Eq. 3.81 shows that the Zeeman splitting is linear as a function of m_f. The splitting depends on g, the Landé g factor of the atom and the magnetic field. We expect the Landé g factor to be of order 1. We could perform a more in-depth analysis of the exact splitting. However, in the experiment, the magnetic field is adjustable and will be tuned in such a way that it just barely removes the degeneracy between the m_f sublevels. In other words, we will adjust H until the separation between adjacent m_f sublevels is just a few times greater than the linewidth of our laser, which is on the order of a few hundred Megahertz. Therefore, for the purposes of our calculations here, we will simply assume that the m_f sublevels for each of our states are not degenerate and that the energies differ by $\sim$100 MHz.

3.2.3 Electric dipole interaction with laser light

The next piece of the Hamiltonian that we need to model involves the interaction with the laser. Following the work of Section 3.1.2, we still model the laser radiation as a classical field that makes a time-dependent contribution to the Hamiltonian. We also make the electric dipole approximation and we assume that V can be written in terms of a dipole interaction: [40] [45] [36] [5]

$$H_{\text{int}} = -\mathbf{d} \cdot \mathbf{E}, \tag{3.82}$$

where $\mathbf{E}$ represents the electric field at the atom, and $\mathbf{d}$ represents the dipole moment operator for our states.

We must now evaluate the dipole moment operator. Specifically, we need to find

$$\langle i|\mathbf{d} \cdot \mathbf{E}|g\rangle \tag{3.83}$$

$$\langle i|\mathbf{d} \cdot \mathbf{E}|e\rangle \tag{3.84}$$

---

[7]$e\hbar/(2m_e c)$ in Gaussian units

in order to calculate Ω_e, Ω_g and, ultimately, Ω_r.

Classically, the dipole moment is a vector quantity that encapsulates the charges and the distance between them. The dipole moment operator that we are looking should, in the classical limit, equal the charge of the electron times some vector that roughly represents the displacement between the electron and the nucleus. The dipole moment operator is defined as

$$\mathbf{d} = -e\mathbf{r}, \tag{3.85}$$

where $\mathbf{d}$ is the dipole moment operator, e is the fundamental charge[8] and $\mathbf{r}$ represents the vector operator describing the electron's position relative to the atom [40].

The electric dipole moment operator commutes with the $\mathbf{S}$ and $\mathbf{I}$ operators. The rotation operators that may be used to generate rotations of the electric dipole moment operator are $\mathbf{L}$, $\mathbf{J}$ and $\mathbf{F}$ [52]. In other words, the electric dipole moment operator is most naturally discussed using the L and m_l basis.

However, our Hamiltonian is still specified using the F, J, I, L, m_f basis. Thus, we must perform a change of basis operation on the electron dipole moment operator. In order to do this, we could use repeated applications of the Wigner-Eckart theorem. However, for now it is more convenient if we make use of an equation similar to Eq. 3.72 that is known in some places as the "spectator theorem" [52].

The theorem says that, given a system with two angular momenta, $\mathbf{J}_1$ and $\mathbf{J}_2$ and total angular momentum $\mathbf{J}_{12} = \mathbf{J}_1 + \mathbf{J}_2$,

$$\langle \gamma' J_1' J_2 J_{12}' || T^{(k)} || \gamma J_1 J_2 J_{12} \rangle =$$

$$(-1)^{J_1' + J_2 + J + k} \langle \gamma' J_1' || T^{(k)} || \gamma J_1 \rangle \sqrt{2J_{12} + 1} \sqrt{2J_{12}' + 1} \begin{Bmatrix} J_1' & J_{12}' & J_2 \\ J_{12} & J_1 & k \end{Bmatrix}, \tag{3.86}$$

---

[8]in our convention, $e > 0$ and the charge of an electron is $-e$

where we have used J_1, J_2 and J_{12} to refer to the initial values for their respective operators and J_1', J_2' and J_{12}' correspond to the final values. The parameters γ and γ' respectively represent the initial and final values of all other quantum numbers that describe the system.

We will use this formula to separate out I and J from F. We eliminate F, by making the following replacements in Eq. 3.86:

$$J_1 \rightarrow J \tag{3.87}$$

$$J_2 \rightarrow I \tag{3.88}$$

$$J_{12} \rightarrow F \tag{3.89}$$

$$\gamma \rightarrow n, L, S. \tag{3.90}$$

This gives

$$\langle n'L'SJ'IF'||T^{(k)}||nLSJIF\rangle =$$

$$(-1)^{J'+I+J+k}\langle n'L'SJ'||T^{(k)}||nLSJ\rangle\sqrt{2F+1}\sqrt{2F'+1}\begin{Bmatrix} J' & F' & I \\ F & J & k \end{Bmatrix}. \tag{3.91}$$

For convenience, we will refer later to

$$\frac{\langle n'L'SJ'IF'||T^{(k)}||nLSJIF\rangle}{\langle n'L'SJ'||T^{(k)}||nLSJ\rangle} = (-1)^{J'+I+J+k}\sqrt{2F+1}\sqrt{2F'+1}\begin{Bmatrix} J' & F' & I \\ F & J & k \end{Bmatrix}. \tag{3.92}$$

Table 3.5 contains several relevant, calculated values of this quantity.

We could use Eq. 3.86 again, making additional substitutions in order to get an expression that relates $\langle n'L'SJ'IF'||\mathbf{r}||nLSJIF\rangle$ to $\langle n'L'||\mathbf{r}||nL\rangle$. In some ways, this would be the most natural thing to do since the electric dipole moment is associated with L and is not related to electron spin. As we mentioned before, the electron spin operator $\mathbf{S}$ commutes with the electric dipole operator. In this sense, the electron spin is a so-called "spectator" operator that could be accounted for with the spectator theorem (as we have just done with F).

However, it turns out that values for the reduced electric dipole moment matrix operator that we found in the literature (this is discussed in Section 3.2.4) are given in the J basis (i.e. $\langle n'L'SJ'||d^{(k)}||nLSJIF\rangle$).

Now, we can calculate the Wigner 6j symbols using the SymPy module in Python [53] [54]. We make our calculation in Table 3.5. The code behind this calculation is included in Appendix E. This allows us to calculate transition rates to specific hyperfine states in terms of the reduced dipole matrix elements that would be used for J states.

States	Exact Values	Approximate numerical values
$F' = 3$, $F = 4$	$0.5\sqrt{7}$	1.32
$F' = 4$, $F = 4$	$-0.1\sqrt{165}$	-1.28
$F' = 4$, $F = 5$	$0.2\sqrt{15}$	0.775
$F' = 5$, $F = 4$	$0.1\sqrt{110}$	1.05
$F' = 5$, $F = 5$	$-0.1\sqrt{165}$	-1.28
$F' = 6$, $F = 5$	$0.5\sqrt{13}$	1.80

Table 3.5 Values of $\langle n'L'SJ'IF'||\mathbf{r}||nLSJIF\rangle/\langle n'L'SJ'||T^{(k)}||nLSJ\rangle$ as given in Eq. 3.92. These coefficients essentially take into account the geometrical considerations that come into play when we discuss an operator that has been described to us in terms of eigenstates of $\mathbf{J}$ if we want to discuss it in terms of the eigenstates of $\mathbf{F}$. In this table, we have placed only values that gave nonzero results. The symbol F' denotes the total angular momentum number of the intermediate ($^2P_{3/2}$) states, while F is for the $^2S_{1/2}$ state. These results were obtained using the SymPy Python module [53] [54]. Code for calculating these values can be found in Appendix E.

3.2.4   Looking up relevant parameters

We would like to carefully determine the value of the dipole moment matrix operator. According to Ref. [51] the magnitude of the dipole moment operator is -4.35075 a.u.(atomic units, a_0e, where a_0 is the Bohr radius and e the fundamental charge) as calculated using

the all-order, relativistic SD method. It is useful to compare this to the value obtained from at least one other source[9]. According to the NIST atomic spectra database, $A_{ki} = 1.41e8$ s^{-1} [46]. This is the Einstein A coefficient associated with the decays from this state. If this is the case, then we use this equation from Ref. [40]:

$$|\langle f||d||i\rangle|^2 = (4\pi\epsilon_0)\frac{3\hbar c^3}{4\omega_0^3}(2J'+1)A_{ki}. \tag{3.93}$$

(This comes from slightly modifying Equation 3.117 in Ref [40]. It was necessary to convert it from Gaussian units by taking $d \to d\sqrt{4\pi\epsilon_0}$. Furthermore, what Ref. [40] calls γ must be renamed A_{ki}. Here J' refers to the total angular momentum of the electron in the upper state, which in our case is 3/2.)

Plugging in our values into Eq. 3.93, we get that the magnitude of $|\langle f||d||i\rangle|$ is 4.344 electron Bohr Dipole Moments. Details of this calculation are contained in Appendix E. Thus, the agreement between the theoretical calculations of Ref. [51] and the experimentally-derived values of Ref. [46] is very good. As a practical matter, this gives us enormous confidence since, not only do the experimental and theoretical approaches to finding the electric dipole reduced matrix element match one another, but we can also be sure that our sources are using the same conventions for, e.g. the Wigner Eckart theorem as we are.

3.2.5 Evaluation of dipole moment matrix operator

Now we will use the Wigner-Eckart theorem in order to calculate the dipole moment matrix elements using the reduced dipole moment matrix operator. The Wigner-Eckart theorem allows us to evaluate the dipole moment operators for all our quantum numbers using the reduced dipole moment matrix operator:

---

[9]It is easy to make simple mistakes regarding units and conventions.

$$\langle \xi', j', m'|T_q^k|\xi, j, m\rangle = \frac{\langle \xi', j'||T^k||\xi, j\rangle}{\sqrt{2j'+1}}\langle j, m, k, q|j', m'\rangle, \tag{3.94}$$

where T^k is a rank k spherical tensor, j' and j represent the angular momentum of the final and initial states respectively, ξ' and ξ represent the final and initial values of all other quantum numbers respectively and $\langle j, m, k, q|j', m'\rangle$ is a Clebsch Gordan coefficient. In our case, we are looking to calculate matrix elements $\langle F', J', L', I', S', m_f'|\mathbf{d}|F, J, L, I, S, m_f\rangle$, so we have:

$$\langle F', I', J', L', S', m_f'|d_q^{(1)}|F, I, J, L, S, m_f\rangle =$$
$$\frac{\langle F', I', J', L', S'||T^k||F, I, J, L, S\rangle}{\sqrt{2F'+1}}\langle F, m_f, k = 1, q|F', m_f'\rangle. \tag{3.95}$$

The reduced dipole moment matrix elements that appear here can be evaluated using Eq. 3.91 and the values we found in Section 3.2.4.

However, before we perform these calculations, we would like to briefly pause and make the case for eliminating some of the states from our consideration in order to keep our equations manageable. Evaluation of the Clebsch Gordan coefficients in Eq. 3.95 eliminates most of the possible states. However, there are still many states with dipole-allowed transitions to worry about.

3.3 States to be used in the experiment

In Section 3.2.2, we discussed how we will be using a magnetic field to break the degeneracy between the m_f sublevels of our state. In Section 3.1, we will discuss the driving of the Raman transitions. There, we will assume that the one photon detuning Δ, is much greater than the two-photon detuning δ. We also expect that our sensitivity to the two-photon detuning δ is such that by tuning our lasers, we can address any m_f levels we like.

Since we are free to choose which m_f levels to address, we will focus on driving $m_f = 0 \rightarrow m_f = 0$ transitions between the $F = 4$ and $F = 5$ $^2S_0$ states since these states will be the least sensitive to drifts in the applied magnetic field.

However, even though we expect the Zeeman splitting to plays a large role in determining which m_f sublevels on the $^2S_{1/2}$ states we can couple to, the Zeeman splitting will be much less important in determining which $^2P_{3/2}$ we can neglect. In fact, Δ will be much larger than the splitting between the m_f levels. Therefore, we need to consider all possible intermediate states that can support electric dipole transitions with both ground states.

Furthermore, based on the other calculations in Ref. [1], we expect that the detuning Δ will be about the same order of magnitude as the Hyperfine splitting. Therefore, we plan to tune our lasers so that Δ is below the lowest of the hyperfine levels of the $^2P_{3/2}$. According to Table 3.4, this means that we expect to be able to focus exclusively on the $F = 5$ states of the $^2P_{3/2}$ level.

In other words, we now restrict our analysis to $m_f = 0$ for the $^2S_{3/2}$ states. For the intermediate states, we will focus on the $F = 5$ $^2P_{3/2}$ states.

3.3.1 Evaluation of Clebsch-Gordan coefficients

We can automatically evaluate the Clebsch Gordan coefficients for our system in order to identify which of the possible $^2P_{3/2}$ states we are coupling to. The condition for an intermediate state to be valid is that we must be able to drive a dipole transition to it from the $F = 5$ $^2S_{1/2}$ state and that we must be able to use our other laser to drive the atom from that state to the $F = 4$ $^2S_{1/2}$ state. If we let the intermediate state be represented by quantum

numbers $F_i = 5, m_{f,i}$, we can write this condition mathematically as

$$\langle (^2\text{P}_{3/2})F_i, m_{f,i}|\mathbf{d}_{q_1}|(^2\text{S}_{1/2})F = 5, m_f = 0\rangle \neq 0$$

$$\Rightarrow \langle F = 5, m_f = 0, 1, q_1|F_i, m_{f,i}\rangle \neq 0. \quad (3.96)$$

In order for the other laser to couple our upper state to the $F = 4$ ground state,

$$\langle (^2\text{S}_{1/2})F = 4, m_f = 0|\mathbf{d}_{q_2}|(^2\text{P}_{3/2})F_i, m_{f,i}\rangle \neq 0$$

$$\Rightarrow \langle F_i, m_{f,i}, 1, q_2|F = 4, m_f = 0\rangle \neq 0, \quad (3.97)$$

where q_1 and q_2 represent the components of polarization of the light from Slave 1 and Slave 2 respectively. $q = 0$ corresponds to linearly polarized light in the z direction, while $q = \pm 1$ corresponds to cicularly polarized light of different handedness.

Evaluating the coefficients by brute force, we see that this condition is met only for a handful of coefficients. These are tabulated in Table 3.6. Based on the values in the table, we see that we must ensure that our lasers are circularly polarized such that one provides $\sigma+$ light and the other provides $\sigma-$ light. Furthermore, we see that the only state with $F = 5$ that we couple to will be the $m_f = 1$ or $m_f = -1$ state. For concreteness, we opt for the $q_1 = 1$, $q_2 = -1, m_{f,i} = 1$ state.

3.4   Calculation of beam geometries

We can use the derived formulae above to calculate the necessary beam geometries.

First of all, we calculate our on-resonance Rabi frequencies. We will calculate the following values:

F_i	q_1	q_2	$m_{f,i}$	$\langle F=5, m_f=0, 1, q_1 \vert F_i, m_{f,i} \rangle$	$\langle F_i, m_{f,i}, 1, q_2 \vert F=4, m_f=0 \rangle$
4	-1	1	-1	$\frac{\sqrt{22}}{11}$	$-\frac{\sqrt{2}}{2}$
4	1	-1	1	$\frac{\sqrt{22}}{11}$	$\frac{\sqrt{2}}{2}$
5	-1	1	-1	$\frac{\sqrt{2}}{2}$	$\frac{\sqrt{33}}{11}$
5	1	-1	1	$-\frac{\sqrt{2}}{2}$	$\frac{\sqrt{33}}{11}$

Table 3.6 The couplings that turn out to give nonzero values for both Eq. (3.96) and Eq. (3.97) for both $F=4$ and $F=5$ $^2P_{3/2}$ states. The total angular momentum quantum number for the intermediate state is given by F_i, while q_1 and q_2 represent polarizations of our laser. Code for calculating these values can be found in Appendix E.

By combining Eqs. (3.95), (3.92), we get that

$$
\langle F', I', J', L', S', m'_f \vert d_q^{(1)} \vert F, I, J, L, S, m_f \rangle = \langle n'L'SJ' \vert\vert T^{(k)} \vert\vert nLSJ \rangle
$$

$$
\times (-1)^{J'+I+J+k} \sqrt{2F+1} \sqrt{2F'+1}
\begin{Bmatrix} J' & F' & I \\ F & J & k \end{Bmatrix}
$$

$$
\times \frac{1}{\sqrt{2F'+1}} \langle F, m_f, k=1, q \vert F', m'_f \rangle. \quad (3.98)
$$

We will now evaluate $\langle F', I', J', L', S', m'_f \vert d_q^{(1)} \vert F, I, J, L, S, m_f \rangle$ for the states we have chosen. First, we will calculate Ω_g, which means that the relevant dipole matrix operator is

$\langle ^2\mathrm{P}_{3/2}, F=5, m_f=1 \vert \mathbf{d} \vert ^2\mathrm{S}_{1/2}, F=5, m_f=0 \rangle$

$$F' \to 5 \qquad\qquad F \to 5 \qquad\qquad (3.99)$$

$$m'_f \to 1 \qquad\qquad m_f \to 0 \qquad\qquad (3.100)$$

$$I' \to 9/2 \qquad\qquad I \to 9/2 \qquad\qquad (3.101)$$

$$J' \to 3/2 \qquad\qquad J \to 1/2 \qquad\qquad (3.102)$$

$$L' \to 1 \qquad\qquad L \to 0 \qquad\qquad (3.103)$$

$$S' \to 1/2 \qquad\qquad S \to 1/2. \qquad\qquad (3.104)$$

Using the values found in Section 3.2.4, we use

$$\langle n'L'SJ'||T^{(k)}||nLSJ\rangle \to 4.344a_oe. \tag{3.105}$$

Using Table 3.1, we get that

$$(-1)^{J'+I+J+k}\sqrt{2F+1}\sqrt{2F'+1}\begin{Bmatrix} J' & F' & I \\ F & J & k \end{Bmatrix} \to -\frac{\sqrt{165}}{10}. \tag{3.106}$$

From Table 3.6, we look up the value of

$$\langle F, m_f, k=1, q|F', m'_f\rangle \to -\frac{\sqrt{2}}{2}. \tag{3.107}$$

After inserting $F' = 5$, we have

$$\langle {}^2\mathrm{P}_{3/2}, F=5, m_f=1|\mathbf{d}|{}^2\mathrm{S}_{1/2}, F=5, m_f=0\rangle \tag{3.108}$$

$$= 4.344a_0e\left(-\frac{\sqrt{165}}{10}\right) \times \left(\frac{1}{\sqrt{2 \times 5 + 1}}\right) \times \left(-\frac{\sqrt{2}}{2}\right) \tag{3.109}$$

$$= 4.344a_0e\left(\sqrt{\frac{3}{20}}\right) \tag{3.110}$$

$$\approx 8.903 \times 10^{-11}\mathrm{em} \tag{3.111}$$

$$\approx 1.426 \times 10^{-17}\ \mathrm{pC\ m.} \tag{3.112}$$

For Ω_e, we look at $\langle {}^2\mathrm{S}_{1/2}, F=4, m_f=0|\mathbf{d}|\langle {}^2\mathrm{P}_{3/2}, F=5, m_f=1\rangle$ and make similar substitutions.

$$F' \to 4 \qquad\qquad F \to 5 \tag{3.113}$$

$$m'_f \to 0 \qquad\qquad m_f \to 1 \tag{3.114}$$

$$I' \to 9/2 \qquad\qquad I \to 9/2 \tag{3.115}$$

$$J' \to 1/2 \qquad\qquad J \to 3/2 \tag{3.116}$$

$$L' \to 0 \qquad\qquad L \to 1 \tag{3.117}$$

$$S' \to 1/2 \qquad\qquad S \to 1/2. \tag{3.118}$$

Similar to the other transition, this gives

$$\langle {}^2\mathrm{S}_{1/2}, F = 4, m_f = 0 | \mathbf{d} |{}^2\mathrm{P}_{3/2}, F = 5, m_f = 1\rangle \tag{3.119}$$

$$= 4.344 a_0 e \left(\frac{\sqrt{110}}{10}\right) \times \left(\frac{1}{\sqrt{2 \times 4 + 1}}\right) \times \left(\frac{\sqrt{33}}{11}\right) \tag{3.120}$$

$$\approx 4.344 a_0 e \frac{1}{\sqrt{30}} \tag{3.121}$$

$$\approx 6.724 \times 10^{-18} \text{ pC m.} \tag{3.122}$$

Using these values, we find that the single-photon on-resonance Rabi frequencies defined in Eqs. (3.36) and (3.37) are

$$\Omega_e = -\frac{\langle i|\mathbf{d} \cdot \mathbf{E}_2|e\rangle}{\hbar} \approx 63760 \mathrm{m/s/V} \cdot \mathbf{E}_2 \tag{3.123}$$

$$\Omega_g = -\frac{\langle i|\mathbf{d} \cdot \mathbf{E}_1|g\rangle}{\hbar} \approx 135221 \mathrm{m/s/V} \cdot \mathbf{E}_1. \tag{3.124}$$

Now, for our laser, we can find the electric field by looking at the intensity of the laser. We recall that

$$I = \frac{c\epsilon_0}{2}|E|^2. \tag{3.125}$$

Thus, if we assume that we are coupling perfectly to our atomic system with light at the correct polarization, we can rewrite $\mathbf{E}$ as

$$|E| = \sqrt{\frac{2I}{c\epsilon_0}}. \tag{3.126}$$

Noting that the intensity equals the power over the area of the beam, we let the beam have waist radius w_0. Now, if we let I_0 represent the intensity of the beam at its peak, then the relationship between the power and the intensity is

$$P_0 = \frac{1}{2}\pi I_0 w_0^2. \tag{3.127}$$

We will pretend that the region where the laser light is shining is a circle of radius w_0 and that within the circle, we have a uniform intensity of

$$I = \frac{P}{\pi w_0^2}. \tag{3.128}$$

We will assume that outside the circle there is no power.

Then, if the ions are travelling through the laser beam, the time they spend is equal to

$$t = \frac{2w_0}{v} \tag{3.129}$$

where t is the time spent in the beam and v is the velocity of the atoms.

The off-resonance Rabi frequency is simply [5]

$$\Omega_r = \sqrt{\Omega_{\textit{eff}}^2 + (\delta - \delta^{AC})^2} \tag{3.130}$$

where

$$\Omega_{\textit{eff}} = \frac{\Omega_e^* \Omega_g}{2\Delta}. \tag{3.131}$$

We assume that we can get $\delta - \delta^{AC} = 0$. So, we need to check on Ω_{eff}. We would like to have it so that

$$\Omega_{\textit{eff}} t = \pi \tag{3.132}$$

Plugging in our approximations for the laser parameters, we can solve for the necessary power.

If we suppose (like Ref. [1]) that we might get 5 mW from each laser for any given interaction zone and that the waist is ∼0.4 mm and that we want $\Delta = 2.5GHz$, then we get 12.92 MHz for the Rabi frequency. This is 10 times smaller than what Ref. [1] calculated.

Counterintuitively, the single photon Rabi rates do not have to match. We can avoid population buildup in the upper states even if they do not match.

Chapter 4

Generation of Seed Light

In this chapter, I will discuss the design and construction of the master laser. I built the master laser system beginning in 2010. Initial work on the master laser was completed by Chris Erickson before I joined the project. He ordered many of the components and did some of the early work to begin to assemble the system.

The main goal of the master laser system is to produce a stable oscillator from which the signals used to injection lock the slave lasers can be derived. It must have a reasonably narrow linewidth in order to allow us to discriminate between the transitions in the ion that we want to stimulate. It must also operate with a single spatial mode. The master laser must also be sufficiently tunable so that its frequency can be set to the appropriate detuning from the $^2S_{1/2} \leftrightarrow {}^2P_{3/2}$ resonance as calculated in Chapter 3.

The main concern regarding the master laser is that we need to get it to the right wavelength. Most of the processes in this chapter involve some means of maximizing the likelihood that we can get the master laser to oscillate at a frequency at which we can run the experiment. The basic means of controlling the master laser are

- Diode selection

- Temperature

- Coarse adjustment of grating using threaded actuators

- Electronic adjustment of grating using piezoelectric actuators

- Current

Each of these factors is interdependent and, in general, the adjustment of one usually involves adjusting all the others. However, the above list of technieques is approximately in order from coarsest to finest adjustment of the master laser frequency. Many of the steps I took in building the master laser were done with the end goal of getting the laser closer to the right wavelength with each step providing finer control and greater accuracy.

4.1   Stabilization of master laser

4.1.1   Master laser layout

The master laser is a 408 nm extended cavity diode laser (ECDL). It consists of a laser diode mounted in a temperature-controlled housing from the Thorlabs LDM21 family of products. It is collimated by a small, aspherical lens (Thorlabs C570TM-A). The master laser ECDL also has a grating mounted outside of the temperature-controlled housing. The grating is mounted on a Thorlabs KC1-PZ piezoelectric kinematic mount, which is attached to the laser via a series of rods. A picture of the master laser can be seen in Fig. 4.1, while a picture of the inside of the housing can be seen in Fig. 4.2.

4.1.2   Master laser diode selection

The diode used in the master laser is a single-spatial mode InGaN diode. Its model number is Mitsubishi ML320G2. The master laser diode was wavelength-selected by the distributor
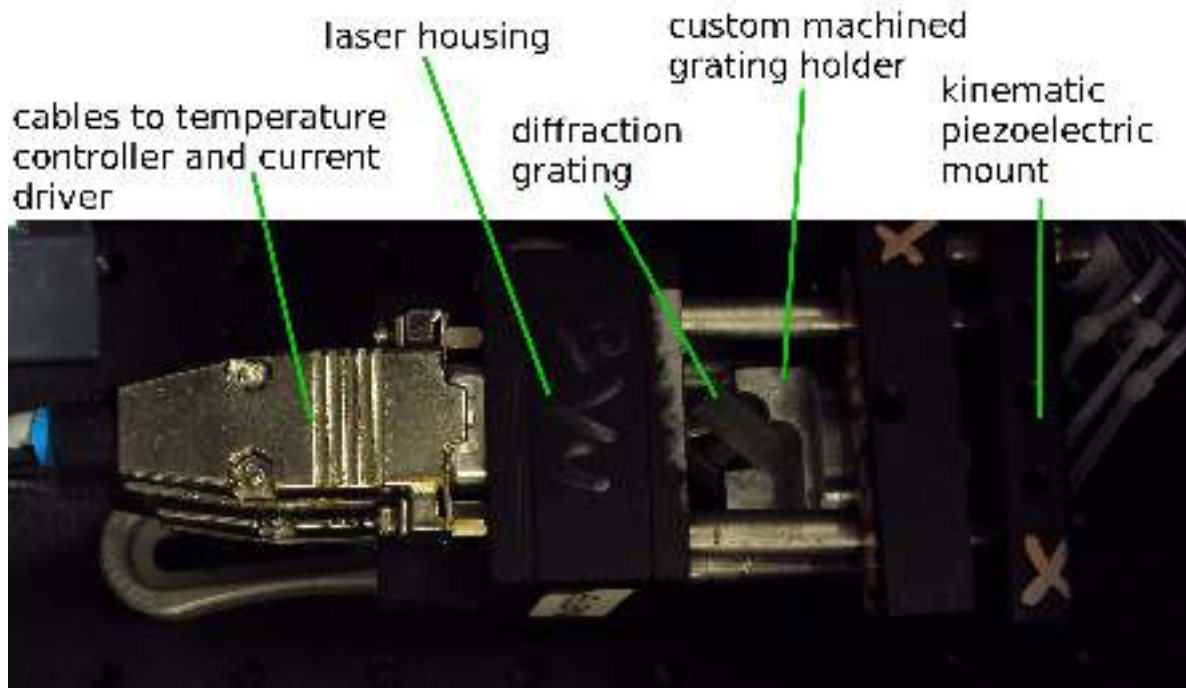
Figure 4.1 The master laser system. The diffraction grating that provides feedback to the laser is mounted on a custom machined grating holder that is attached to the Thorlabs KC1-PZ piezoelectric kinematic mount. I initially tried several other configurations. However, after multiple iterations, I found that the use of the metal rods to provide direct mechanical coupling between the laser and grating mount were necessary for stable, single-mode operation. I also found through trial and error that placing the grating a distance of $\sim$4 cm from the aperture seemed to allow this particular laser to operate single mode for relatively long periods of time (about a day or so in open loop conditions).
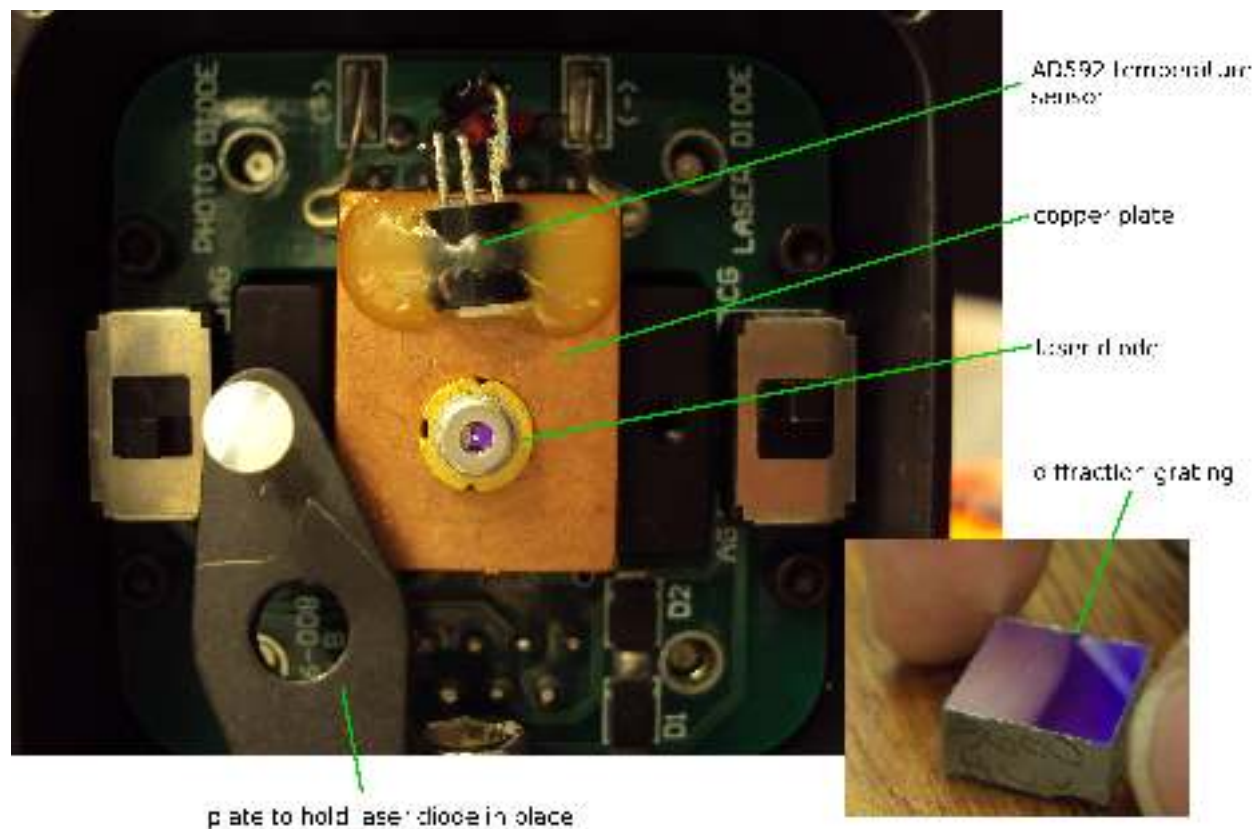
Figure 4.2 The master laser in its housing and the diffraction grating before it was installed (inset). We modified the housing to include an additional temperature sensor (the AD592), which can be seen glued to the top of the copper plate. In this particular photo, the anodized aluminum plate that holds the laser diode in place has been moved aside to allow an unobstructed view of the laser diode.

(i.e. the distributor performed measurements and binned the parts based on their output wavelengths; we then ordered lasers from their 408 nm bin). The diode is very similar to the diode lasers used in Blu-ray players. In fact, we also bought 30 diodes on eBay that had been removed from actual Blu-ray or HD-DVD players as backup diodes. We measured the free running wavelengths of these diodes in order to bin them ourselves using techniques that I will describe in Section 4.1.3. Some of these diodes were ultimately used in the slave lasers, whose configuration will be described in Section 6.2.

The selection of laser diodes required a few iterations before I found diodes that would

work properly. I initially tried to build the master laser using a non-wavelength-selected Sharp GH04020A2GE low power diode, which I could not stabilize for unknown reasons. I quickly switched to a non-wavelength-selected Sharp GH04P21A2GE diode for the master laser. However, this laser's free-running wavelength at 25°C was far too low. In order to tune this diode to the correct wavelength, I found that I had to maintain the diode at a temperature of ∼60°C. This required me to modify our temperature controller to increase its output current. Running at such a high temperature resulted in degradation of the diode and loss of power over the course of a few months. It was this experience that prompted me to use wavelength selected diodes. In this way, I was able to get a laser that could lase at the wavelength we needed without having to risk seriously diminishing the operational lifetime of the laser.

4.1.3   Grating spectrometer wavelength measurements

In order to tune the master laser to precisely the correct wavelength and to measure the room-temperature, free-running wavelength of the uncharacterized lasers (i.e. the lasers that were bought on eBay and later used in the slave lasers), I used a compact grating spectrometer from the Ocean Optics USB2000 series to measure the center frequency of the free-running laser diodes. This spectrometer uses a diffraction grating to separate light based on its constituent wavelenghts. Light scattered off the diffraction grating is detected by a CCD array consisting of 2048 pixels that is also enclosed in the spectrometer. The average difference in wavelength between adjacent pixels is ∼.061 nm.

I tried several techniques to maximize the resolution and accuracy of these measurements. The center wavelength of the bare diodes changed only a few nanometers over the entire range of possible temperatures and currents. In order to ensure accurate absolute wavelength measurements, we calibrated to a mercury source both before and after looking at the spectra
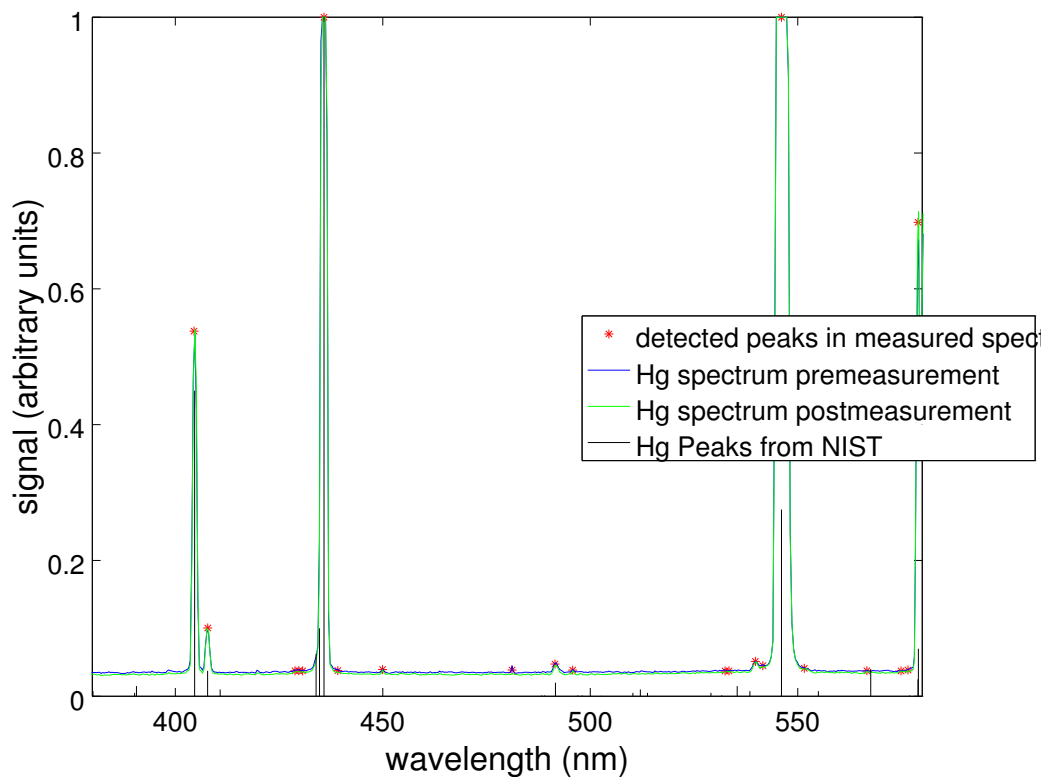
Figure 4.3 Data from the calibration using the mercury lamp. I deliberately allowed some of the peaks to saturate in order to improve our signal for the peaks near 408 nm. The black lines represent spectral lines taken from the NIST Atomic Spectra Database [46]. The average of the premeasured and postmeasured Hg spectra was sent through an Octave script I wrote that automatically identified peaks in the spectrum, displayed the peaks, and then allowed the user to select which peak in the NIST Hg spectrum these peaks corresponded to. The peaks found by this script are displayed with the label, "detected peaks in measured spectrum."
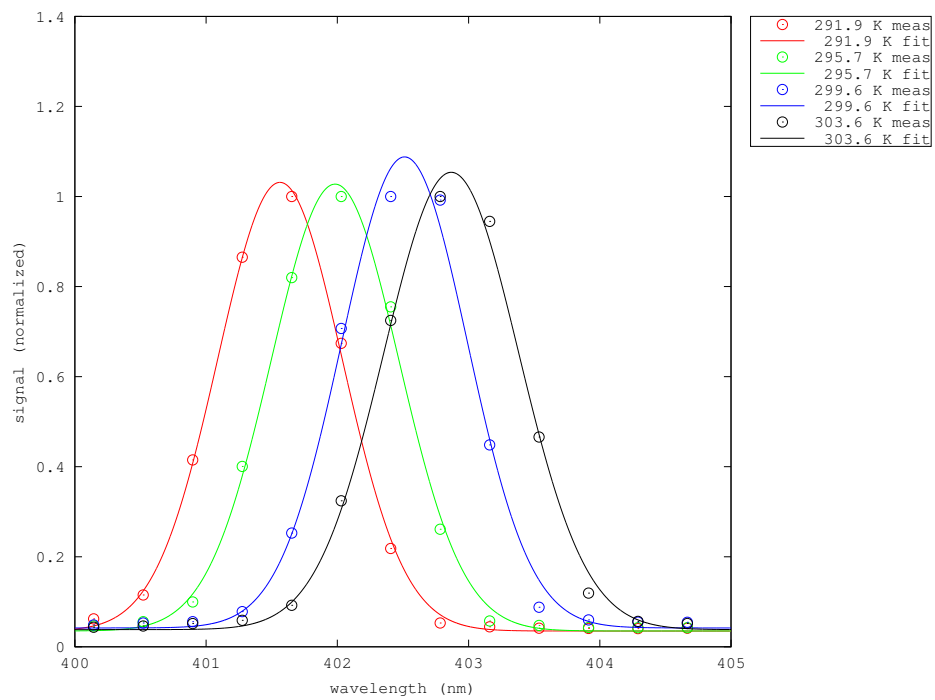
Figure 4.4 Spectrum of one of the free-running diodes I tested for use in the master laser at four different diode temperatures.
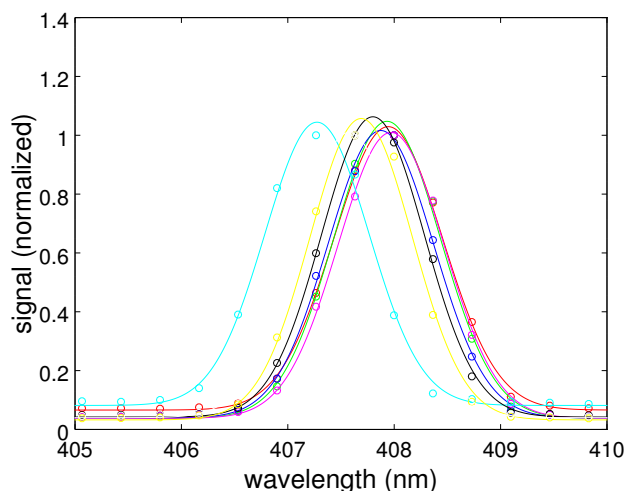
Figure 4.5 Representative data of the free-running (i.e. no grating feedback or extended cavity) wavelength of several wavelength selected lasers taken at 120 mA and 22.5°C.

of the various lasers. We feel confident in our calibrations since mercury conveniently has spectral lines at 405 and 436 nm, which are close to our target wavelength of 407.771 nm. A typical before and after calibration spectrum taken using the mercury lamp can be seen in Figure 4.3. When analyzing the peaks produced by the laser on the grating spectrometer, we fit the measured data to a Gaussian distribution in hopes of squeezing out some sub-pixel level resolution of the peak location. Examples of this type of analysis are shown in Figures 4.4 and 4.5.

The temperature and the current of the laser diode are two of the main means we have for affecting the wavelength of the free-running master laser diode. Using a grating spectrometer, we measured the center wavelength of the bare laser (i.e. no grating feedback or extended cavity).

We have data on the wavelength dependence on temperature and current for our laser. This data is plotted in Fig. 4.6. We see that the variation of the center wavelength of the laser is roughly linear over reasonable values of temperature and current.
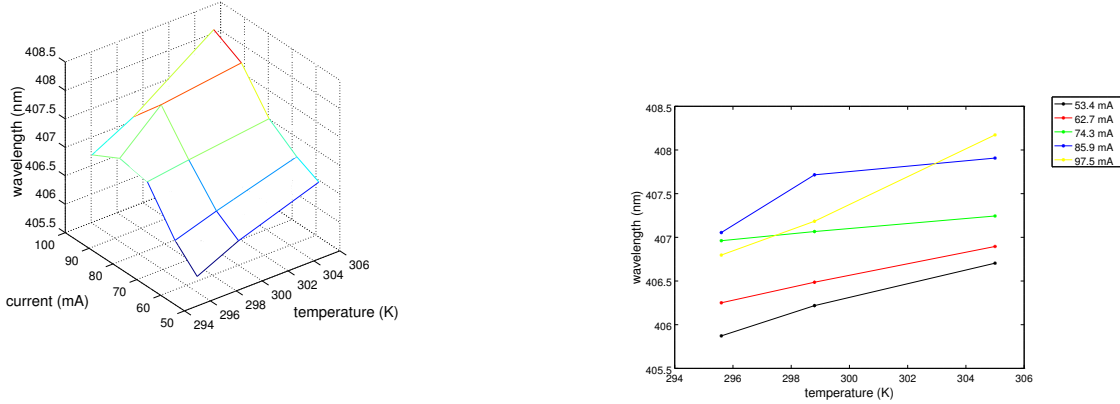
Figure 4.6 Representative data of the free-running wavelength of the master laser as a function of nominal current and nominal temperature. Both plots show the same data. This data was taken using a diode that was eventually used in the master laser.

4.1.4 Placement of the grating

Lasers work by amplifying light resonant with a particular mode of the laser cavity via stimulated emission. Ideally, we would like to favor a cavity mode corresponding to our desired wavelength. In order to accomplish this, we add yet another resonant cavity outside our laser that can couple light back into the laser.

This cavity is formed by a diffraction grating on one side and the laser's output coupler on the other side. This configuration is called an Extended Cavity Diode Laser (ECDL). The grating we selected was a Thorlabs model number GH13-36U, which has 3600 lines/mm. A picture of the grating can be seen in Figure 4.2.

The diffraction grating is angled so that the first order diffraction peak at 407.771 nm is directed back into the laser. The condition for this to be the case is

$$n\lambda = 2d\sin(\theta), \tag{4.1}$$

where n is the order of the diffraction peak (in our case, $n = 1$), d is the spacing between slits (in our case $d = 1$ mm$/3600 = 278$ nm) and θ is the angle of incidence to the grating. We can therefore calculate that the θ should be approximately 47.2°.

I machined a custom grating holder out of aluminum, which was machined to set the angle near 47.2° and can be seen in Figure 4.1. The aluminum holder was mounted in a Thorlabs KC1-PZ piezoelectric mount, which allows us the necessary fine control of the grating's location and angle over a narrow range. The grating was mounted approximately 4 cm from the aperture of collimating lens. I had to ensure that the diffraction grating is installed such that both the angle and the cavity length match our desired wavelength. In order to get the grating aligned initially, I turned on the current to the laser until the laser was just below the threshold where it would begin to lase. We then aligned the grating using the threaded actuators on the piezoelectric mount until we saw the output power of the laser increase. When this happens, it indicates that we are successfully coupling light to the laser cavity. The output power of the laser can be monitored by eye or by instrument and it is fairly easy to get a feel for what it should look like when the grating first couples to a laser operating just below threshold. After light is coupling, I often again turn the current even lower and try to get the laser to lase at an even lower current. This process can be repeated several times in order to maximize the coupling of the light from the grating back to the laser.

After this, I used a Bristol 521 wavelength meter to measure the wavelength. The Bristol 521 is a calibrated instrument that relies on an optical Michelson-Morley interferometer to make measurements. (We used the grating spectrometer method instead of the Bristol 521 for the free-running lasers because the free-running lasers' linewidths was too large to be successfully measured on the wavelength meter.) Using the wavelength information from the wavelength meter, the laser is tuned iteratively by adjusting the grating using the

threaded/manual actuators. For each adjustment, I then find new sets of currents at which the laser will operate stably.

4.1.5 Ensuring ability to fine tune

The piezoelectric actuators on the grating mount can also be moved electrically. It is important that we find a way to move the piezeoelectric actuators in concert in such a way that we maximize the range over which we can scan the laser frequency without the laser mode hopping. When the $^{87}Sr^+$ ion interferometer is operational, we might need this for several reasons: First, it may be the case that we decide to lock the laser to an external reference like a vapor cell or a cavity. In this case, the laser frequency will need to be adjusted based on an error signal that we derive from our stable reference. In the current setup, we do not lock the laser to any external reference (we probably do not need to since we plan to operate the lasers fairly far from the resonance and the system has been shown to be relatively insensitive to the overall frequency). However, we never know if we might decide we want to on some later date. Second, the ability to modulate the laser with a single knob is very handy. In fact, this is what we did to verify that the slave laser frequencies were properly tracking with the master laser frequency (see Fig. 7.1). Experimenters running the ion interferometer experiment will likely appreciate a simple way to tune the laser manually that does not involve rather having to adjust several pieces separately.

The control circuitry is similar to the PID controllers desribed in Ref. [1] that are used elsewhere in the lab (see Fig. 4.7). These PID controllers consist of a simple PID controller combined with a "scan balancer." The PID controller segment of the circuit could be used to generate a feedback signal based on an error signal. We could generate suitable error signals by measuring absorption through a vapor cell or by looking at transmission through a cavity.

The scan balancer portion of the circuit takes the feedback signal and allows us to use it to generate three signals with independently-controllable gains: one signal can be used to modulate the current coming from the laser current driver, while the other two signals can be amplified and sent to the piezoelectric actuators. The circuit also features a DC offset that can be digitally controlled and added directly to the feedback signal. Thus, if the scan balancer is configured with suitable gains, the experimenter can make fine adjustments to the tuning of the master laser using a digital control knob.

In order for this to work, we must properly set the gains in the scan balancer. There is some insight to be gained by modeling the ideal relative motion of the piezoelectric actuators. We would like to find a way to ensure that the grating moves and rotates in such a way that the resonance of the cavity it creates changes as smoothly as possible over as wide a range of wavelengths as possible.

The change in the wavelength reflected from the grating as a function of θ can be found by taking the derivative of Eq. 4.1 with $n = 1$:

$$\frac{d\lambda}{d\theta} = 2d\cos(\theta). \tag{4.2}$$

However, as the grating rotates, we also want to make sure that the cavity length (L) changes in such a way that the change in the resonant wavelength of the external cavity varies at the same rate as the change in the wavelength favored by the rotation of the grating. The relationship between the cavity length and the resonant wavelength is

$$L = m\frac{\lambda}{2} \tag{4.3}$$

where m is an integer, L is the length of the external cavity and λ is the wavelength in air.

We note that L and θ are both functions of the displacement of the piezo actuators. For small changes in L and θ, we can assume that the piezoelectric actuators need to provide displacements in a constant ratio. That is, if we let x_1 be the displacement of the linear

Figure 4.7 Schematic of the PID circuit that we use on the master laser. The PID stages are depicted at the bottom left of the diagram and these will be used only if we lock the laser system to an external reference. At the top left of the diagram is a DAC that allows us to set a digital offset. The signal from this DAC is added directly to the feedback signal that comes out of the PID stages. Even if we do not lock the laser to a vapor cell, we can use the DC offset signal to manually adjust the position of the grating in a controlled way and therefore to tune the laser.

actuator on one side from its initial position and allow x_2 to be the displacement of the linear

actuator on the other side, we define the Piezo ratio R as

$$\text{piezo ratio} = x_2/x_1. \tag{4.4}$$

We would like to find some value of R such that

$$\frac{d\lambda}{d\theta(x_1, x_2)} = \frac{d\lambda}{dL(x_1, x_2)}. \tag{4.5}$$

or, taking $x_1 \rightarrow Rx_1$ as in Eq. (4.4),

$$\frac{d\lambda}{d\theta(x_1, Rx_1)} = \frac{d\lambda}{dL(x_1, Rx_1)}. \tag{4.6}$$

where $\theta(x_1, x_2) = \theta(x_1, Rx_1)$ is the angle at which the grating is rotated relative to its initial

position as a function of the piezo displacements, or as a function of the piezo ratio and the

displacement of one of the piezoelectric actuators. $L(x_1, Rx_2) = L(x_1, Rx_1)$ is the length of

the cavity as a function of the same two variables. This problem depends heavily on the

geometry of the system. The solution involves a lot of terms and geometric bookkeeping.

Our model is detailed in a well-commented Mathematica Notebook included in Appendix B.

The result is that we calculate that $R = 0.478755$ is the ratio between the displacement of our

piezoelectric actuators that will rotate and move the grating properly given the geometry

of our grating mount. In practice, we would fine tune this ratio by scanning the piezos

and iteratively making adjustments to maximize the size of the range over which the laser

operates single mode. However, the calculation is nice to have since it gives a good starting

point. The calculation is also useful because some diffraction grating mount geometries result

in surprising ratios (for example, one of the lasers discussed in Ref. [1] required that the

piezos scan in opposite directions (i.e. have a negative ratio), which required a change to

the scan balancer circuitry).

4.1.6 Calculation of maximum safe intensity

The specifications in the datasheet for the laser diode are valid only when the diode is free running. However, using the laser in an ECDL configuration requires coupling power back into the laser diode. In order to ensure that we did not damage our laser, we performed a brief calculation. We assumed that the maximum current for which the diode is rated corresponds to the maximum amount of power that can be emerging through the front facet of the laser without damage. We put the maximum recommended current of 250 mA through the laser and measured the output. Then we measured the efficiency of the grating. From this, we were able to model the external cavity and deduce how much power would be coming out of the external cavity when the power coming out the front face of the laser was near its maximum allowable value. We then measured the output of the cavity for various currents. We estimated that it is safe to run the laser at currents up to $\sim$105 mA.

4.2 Operation

The master laser successfully runs single mode. It has been tuned to the correct 407.771 nm wavelength with the Bristol Wavemeter while operating single mode with grating feedback with a temperature of 26.798°C and a current of 65.9 A. It produces 19 mW of power.

Chapter 5

Installation of the AOM

We generate shifted beams by sending the seed light through an Acousto-optic Modulator (AOM)[1] using a double pass configuration. This is illustrated in Figure 5.2. A photograph of the AOM can be seen in Figure 5.1.

The AOM we use is model number TEF-2500-200-405 made by Brimrose Corporation of America. The crystal material is Tellurium Flouride; the center carrier frequency is 2500 MHz; the bandwidth (3dB) is 200 MHz. The AOM's anti-reflective coatings are specified to work at 405 nm.

5.1 Principle of operation

The AOM is a crystal with a piezoelectric transducer attached to one side and an acoustic absorber attached to the other side. Acoustic waves are produced by the tranducer. These waves travel across the active area of the AOM crystal and are absorbed by the absorber on the other side. The compression and decompression caused by the travelling acoustic waves changes the index of refraction within the crystal as a function of both space and time. This

---

[1]also known as an Acousto-optic frequency shifter
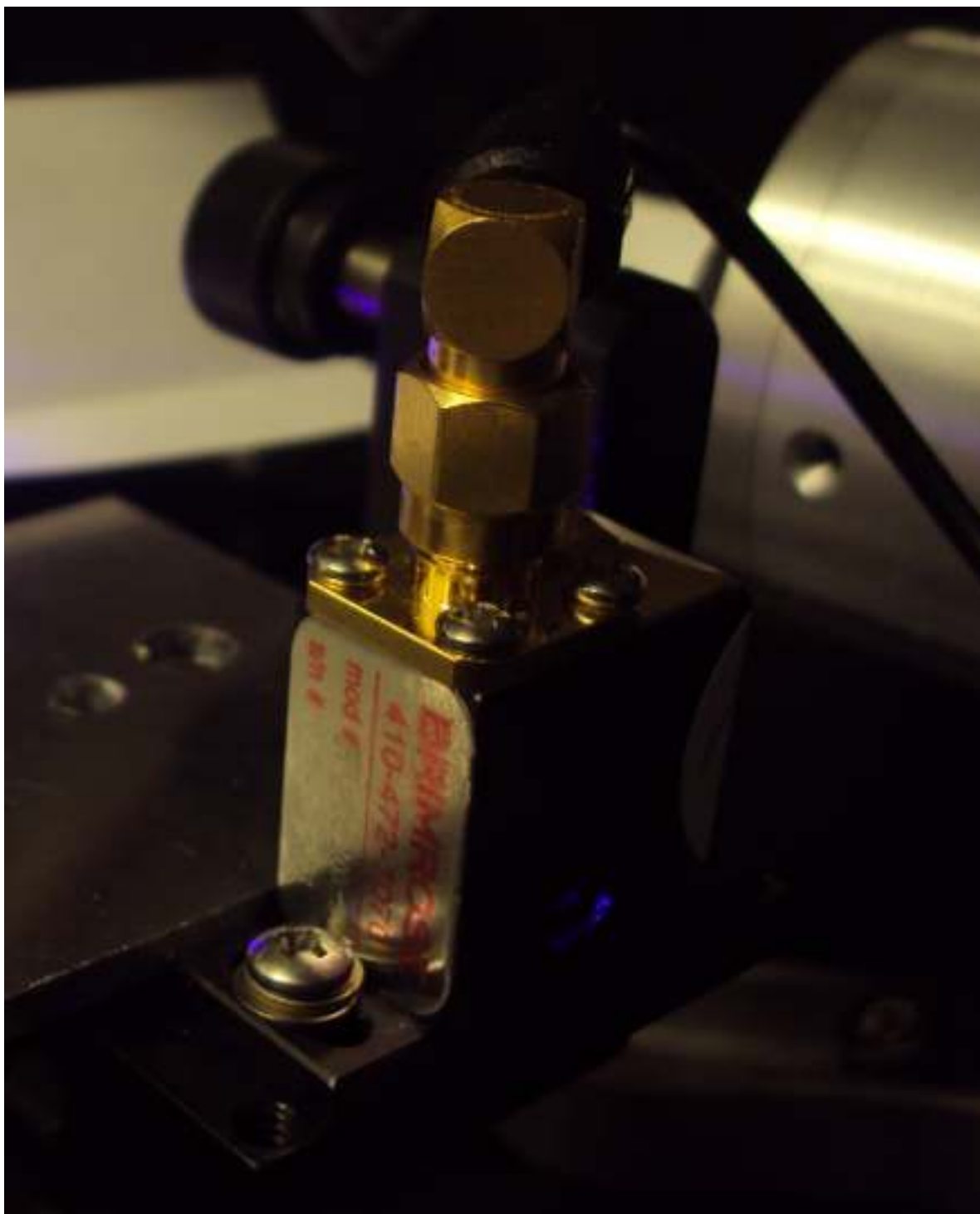
Figure 5.1 The AOM mounted in the setup. The aluminum plate in the lower left part of the photo that can be seen butting up against the AOM was used only as a guide for initial AOM alignment and was removed in the final system.
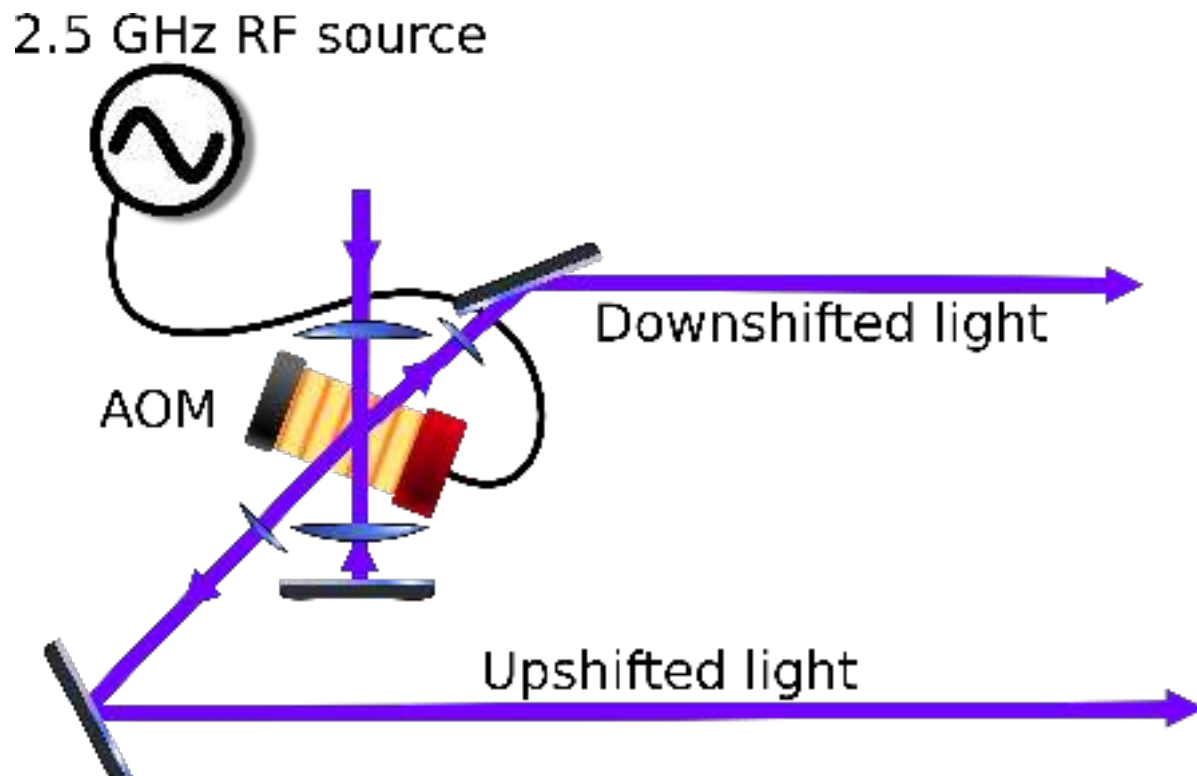
Figure 5.2 Detail of Figure 2.2. The light from the master laser is depicted entering from the top of the diagram. This beam travels into the AOM, which is depicted in the center of the diagram. The upshifted light (upshifted in frequency, or blue shifted) is depicted travelling towards the lens and mirror near the lower left side of the diagram. The zeroth order diffracted beam is recollimated and then retroreflected. The downshifted light (red shifted) is depicted exiting the AOM towards the top right of the figure.

creates what are effectively a series of travelling Bragg planes that correspond to the acoustic wavefronts travelling across the crystal. Light crossing through the crystal can experience Bragg reflection off these planes and, because the effective reflective surface is moving, the light scattered off these features is Doppler-shifted. This light emerges at a distinct angle compared to the incoming light. This allows the AOM to produce frequency-shifted beams that are spatially separated from the unshifted components of the beam.

The relationship between the driving frequency and the Bragg angle for an AOM is well known and is given by

$$m\lambda' = 2\Lambda \sin\theta_B \tag{5.1}$$

where θ_B is the Bragg angle (which is measured between the incoming beam and the Bragg planes), λ' is the wavelength of the laser within the AOM crystal, Λ is the wavelength of the acoustic wave in the crystal medium, and m is an integer representing the diffraction order. The deflection angle (the angle between the unshifted portion of the beam and the outgoing shifted portion of the beam) is equal to twice the Bragg angle. Only $m = 0, 1$ are relevant to the experiment. The $m = 1$ beams are the ones used to injection lock the slave lasers. The $m = 0$ beam refers to the laser light that passes straight through the AOM with no frequency shift. Most of the power emerges in the $m = 0$ diffraction order. The $m = 0$ order beam from the first pass is retroreflected to produce the second pass.

The relationship between the driving frequency and the shift in the frequency of the light simply turns out to be

$$m f_{\text{driving}} = \Delta f_{\text{laser}}. \tag{5.2}$$

Ultimately, getting the AOM to work properly involves optimizing just a few parameters. The AOM must be installed at the right angle relative to the incoming beam. I must ensure that as much of the incoming beam as possible hits the active aperture of the AOM, which is specified as having dimension 0.05 mm. This requires alignment in the X and Y directions,

but it also means that I attempted to maneuver the AOM so that the focal point of the incoming beam was approximately in the center of the crystal in the Z direction as well (direction of propagation). This way, we keep the beam small on both of the entry holes in the case of the AOM. I also optimized the power used to drive the piezoelectric transducer. Furthermore, the intensity and shape of the incoming beam were adjusted to ensure that we do not exceed the maximum allowable intensity for the AOM, which is specified as 50 W/mm^2. Thus, I will first discuss some work I did to characterize the incoming beam.

5.2 Optimization of beam waist

First, we would like to control the beam so that at its focus nearly all of the beam ($\sim 99.96\%$) is within the active area of the AOM. This area is specified as being 0.05 mm wide. Our goal is to have a beam waist radius that will be $\approx$4 times smaller than this 0.05 mm value.[2] If the beam waist is too small, we have to reduce the power to avoid damaging the AOM. Also, the diffraction efficiency decreases because the beam will interact with fewer Bragg planes. If the waist is too large, only a small portion of the beam would be within the active area of the AOM. This would reduce diffraction efficiency and cause distortion of the laser's transverse mode.

We can model the laser as a Gaussian beam. Gaussian beams have the property that their intensity profile always takes a Gaussian shape, i.e. [55]

$$I(\mathbf{r}) = I_0 \exp\left(-\frac{2r^2}{w(z)^2}\right), \tag{5.3}$$

where z and r are cylindrical polar coordinates. z represents position along the axis of propagation with the point $z = 0$ defined to be the point along the beam path at which the beam is narrowest, while r is the coordinate describing the distance from the z axis. I_0

---

[2]Note that I am comparing the beam waist *radius* to the full *width* of the active area.

represents the intensity of the beam at $z = 0, r = 0$ and $w(z)$ is a function that gives the radius of the Gaussian beam, which is given by:

$$w(z) = w_0 \sqrt{1 + \frac{z^2}{z_R^2}}. \tag{5.4}$$

The beam radius, $w(z)$, is also the distance from the center of the beam to the point where the intensity of the beam has fallen by a factor of $1/e^2$ (i.e. the spot size). While the Rayleigh range is denoted z_R, and also satisfies the relation

$$z_R = \pi w_0^2 / \lambda. \tag{5.5}$$

A slight modification of Eq. (5.3) allows us to model elliptical beams by allowing for a different waist in each of the x and y directions:

$$I(\mathbf{x}, \mathbf{y}) = I_0 \exp\left(-2\left(\frac{x^2}{w_x(z)^2} + \frac{y^2}{w_y(z)^2}\right)\right). \tag{5.6}$$

Here, there are two relevant beam radii, w_x in the x direction and w_y in the y direction. Each of these has an associated Rayleigh range z_{Rx} and z_{Ry}, and each satisifies relations analagous to Eqs. (5.4),(5.5).

I can measure the Gaussian beam radius in one dimension using a standard knife-edge technique. This involves placing a photodiode in the path of the beam. A razor blade is then moved perpendicular to the beam in a controlled way such that the beam is partially blocked. The blade is then moved across the laser beam in a direction perpendicular to the blade's edge to several different locations. For each razor blade position, the power incident on the photodiode is measured. By integrating Eq. 5.6, we get

$$\text{Power incident on photodiode} = \frac{1}{2}P\left(\text{erf}\left(\frac{\sqrt{2}x}{W_{0x}}\right)\right). \tag{5.7}$$

We do this several times at various points along the path of the laser and can perform a curve fit to calculate our beam divergence and therefore infer its waist.

I was somewhat worried that modeling the beam coming into the AOM as a Gaussian beam would not be adequate. This was in part due to irregularities in the transverse mode of the master laser. Because I was planning to operate the AOM relatively close to its damage threshold, I examined the possibility of using a more sophisticated theory to model our beam based on measurable parameters.

Siegman [56] discusses the characterization of beams in terms of a quantity that is known simply as "M^2." One way to interpret M^2 is that it serves as a measure of how Gaussian a beam is. If a beam is Gaussian, $M^2 = 1$. If a beam contains higher order Laguerre-Gaussian modes, M^2 will be greater than 1. In Ref. [56], Siegman asserts that any beam comprised of Laguerre-Gaussian modes can be mathematically proven to propagate according to the following equation:

$$W_x^2 = W_{0x}^2 + \left(\frac{M_x^2 \lambda}{\pi W_{0x}} \right)^2 (z - z_{0x})^2 \tag{5.8}$$

The z coordinate of the x-direction beam waist is given by z_{0x}. The spot size parameter (radius) of the beam in the x direction is represented by $W_x(z)$, which can be written as

$$W_x(z) = 2\sigma_x, \tag{5.9}$$

where the second-moment width, σ_x, is defined by

$$\sigma_x^2 = \frac{\int_{-\infty}^{\infty} (x - x_0)^2 I(x, y) \, dx \, dy}{\int_{-\infty}^{\infty} I(x, y) \, dx \, dy}. \tag{5.10}$$

Here $I(x, y)$ is the intensity profile of our beam, which is propagating in the z direction. The second moment width σ_x^2 then satisfies the following equation:

$$\sigma_x^2 = \sigma_{0x}^2 + \left(\frac{M_x^2 \lambda}{4\pi \, \sigma_{0x}} \right)^2 (z - z_{0x})^2. \tag{5.11}$$

In the special case of the Gaussian beam, $2\sigma_x(z) = w_x(z)$.

In principle, we could take measurements of σ_x^2 for our beam using the knife edge technique described above at several points along the beam's path and then fit this to Eq. 5.11.

I tried allowing M^2 to be one of my fit parameters as I analyzed data from the beam, but I found it difficult to get data of sufficient quality to give a good estimate. The knife edge data did not have sufficient resolution over a large enough range. One problem is that the contribution to σ_x increases as the square of the distance from the center of the beam. This means that any measurement has to be very accurately adjusted to compensate for background offset. I also attempted to use a camera, but I was not able to trust its linearity and offsets enough to get good results. Information about my attempt to calibrate the camera can be found in Appendix A.

However, I did consider the implications on the beam if $M^2 \neq 1$. I can look at the effective slope of divergence by rearranging Eq. 5.11 and taking the limit as $(z - z_R) \to \infty$

$$\frac{\sigma_x}{z - z_R} = M_x^2 \frac{\lambda}{4\pi\sigma_{0x}} \tag{5.12}$$

Note that the smallest possible beam waist radius corresponding to any given beam divergence occurs if $M^2 = 1$. That is, if I measure the beam divergence and perform my curve fit assuming that $M^2 = 1$, the beam-waist radius that I calculate will be guaranteed to be *smaller than or equal to* the actual beam waist radius of the beam no matter what the beam's actual value of M^2 might be. Thus, for the purposes of keeping the intensity at the beam waist below the AOM's damage threshold, the assumption that $M^2 = 1$ gives a sort of "worst case scenario."

5.2.1 Ray transfer matrix analysis of system

It is crucially important that I limit the intensity of the light that passes through the AOM. As a sanity check, I now calculate what the beam waist should be for our optical setup using an ABCD matrix (ray-transfer matrix). This model can be used to estimate the sensitivity of the system to small changes in the setup. In this way, I can verify that the system is

robust against small changes and realignments and thereby gain some small reassurance. For example, if the master laser ever had to be taken apart and reassembled, it would likely be the case that there will be tiny differences in the position of the laser or collimating lens. I seek to verify that such small changes will not yield catastrophic changes in the size of the beam as it passes through the AOM.

There is a method of modeling Gaussian beam propagation using a matrix

$$M = \begin{bmatrix} A & B \\ C & D \end{bmatrix} \tag{5.13}$$

which is known as a "ray transfer matrix" or simply as an "ABCD matrix." We will use the well-known rule [57] [55] for modelling a Gaussian beam as it passes through a system described by a ray transfer matrix with elements A,B,C and D, which is

$$z_0' - i z_R' = \frac{A(z_0 - i z_R) + B}{C(z_0 - i z_R) + D}. \tag{5.14}$$

Here, z_0' represents the location of the beam waist relative to the end of the system described by the ABCD matrix and z_R' represents the new Rayleigh range of the beam. The location of the beam waist relative to the start of the system described by the ABCD matrix and the Rayleigh range of the incoming beam are represented by z_0 and z_R respectively. This can be solved to give

$$z_R' = \frac{z_R(BC - AD)}{C^2 z_0^2 + C^2 z_R^2 + 2CD z_0 + D^2} \tag{5.15}$$

$$z_0' = \frac{AC z_0^2 + AC z_R^2 + AD z_0 + BC z_0 + BD}{C^2 z_0^2 + C^2 z_R^2 + 2CD z_0 + D^2}. \tag{5.16}$$

(Note that in an ABCD matrix, A and D are unitless, while B has units of [length], and C has units of [length]$^{-1}$.)

The system has only a few components that we need to model. At the start, we assume that the light coming out of the face of the laser diode is essentially a Gaussian beam with

different beam waist radii for the x and y directions. The waist of this beam can be estimated based on parameters given in the datasheet. The datasheet for the master laser shows that a typical angle of divergence for light coming out of the laser is going to be 9° in one direction and 19° in the other. A Gaussian beam's angular divergence can be surmised by looking at Eq. 5.12. The relationship turns out to be the one given in Ref. [58]:

$$\theta_x = \frac{\lambda}{\pi w_{0x}} \tag{5.17}$$

$$\theta_y = \frac{\lambda}{\pi w_{0y}}. \tag{5.18}$$

Using this equation, we calculate the equivalent Gaussian beam height and width at the face of the laser based on the given angle of divergence of light. The beam waist dimensions turn out to be 972.913 nm and 460.854 nm at the face of the laser.

The light from the laser head is emitted and collimated by a lens[3] with focal length 2.84 mm. The propagation of the light from the laser diode to the collimating lens can be represented by the matrix

$$\begin{bmatrix} 1 & d_1 \\ 0 & 1, \end{bmatrix} \tag{5.19}$$

where d_1 represents the distance between the face of the laser and the collimating lens. The effect of the collimating lens is represented by the following ABCD matrix:

$$\begin{bmatrix} 1 & 0 \\ -1/f_a & 1 \end{bmatrix}. \tag{5.20}$$

Here, $f_a \approx 2.84$ mm is the focal length of the lens

The beam then goes through various optical components, including the diffraction grating, the optical isolators, some waveplates, a polarizing beam cube, and many mirrors. The collective impact of these components on the waist of the beam can be modeled as simple

---

[3]Thorlabs C570TM-A

propagation over some effective distance. In order to be complete, I will evaluate the out-going beam properties over the entire range of possible path lengths. This is much easier than trying measure the total path length accurately and then trying to find detailed dimensions and indices of refraction for all the components in the system. The ABCD matrix representing this propagation is given by

$$\begin{bmatrix} 1 & d_2 - d_1 \\ 0 & 1 \end{bmatrix},$$ (5.21)

where d_2 represents the total distance the beam travels from the face of the laser diode up until it reaches the lens that focuses it into the AOM. Thus, $d_2 - d_1$ represents the distance from the collimating lens of the master laser to the lens that focuses the beam into the AOM. I estimate the the effective distance of propagation should be on the order of 1 m. To be safe, I will ultimately examine what happens for all beam paths between 0.5 m and 2 m.

Finally, the beam is then focused by a lens with focal length 10 cm and passed through the AOM. The focusing of the 10cm focal length lens is represented by

$$\begin{bmatrix} 1 & 0 \\ -1/f_f & 1 \end{bmatrix},$$ (5.22)

where the focal length of the lens is written as f_f.

We can write the ABCD matrix for the whole system as the product of the ABCD matrices that represent the individual components of the system that were found in Eqs. (5.19),(5.20),(5.21), and (5.22):

$$\begin{bmatrix} 1 & 0 \\ -1/f_f & 1 \end{bmatrix} \begin{bmatrix} 1 & d_2 - d_1 \\ 0 & 1 \end{bmatrix} \begin{bmatrix} 1 & 0 \\ -1/f_a & 1 \end{bmatrix} \begin{bmatrix} 1 & d_1 \\ 0 & 1 \end{bmatrix} = \begin{bmatrix} A & B \\ C & D \end{bmatrix}.$$ (5.23)

Finding the resulting ray transfer matrix that describes the system involves simply performing the matrix multiplication prescribed in Eq. 5.23. However, I opt not to write out

result in this thesis. Instead, I used Mathematica to find the expressions for z'_R and z'. These expressions were then evaluated numerically for several values of likely experimental parameters. In particular, I was interested in verifying that the beam waist inside the AOM remains reasonable for realistic values of d_1 (the distance from the laser face to the collimating lens) and d_2 (the distance traveled between the collimating lens and the other lens), since these are values that may not be known to high precision and which may drift with time.

From this analysis, I calculated the effective area of the beam for many values of d_1 and d_2. For each of these values, I calculated the corresponding ratio between the intensity at the most intense part of the beam and the total power in the beam. The way to interpret this is that if we have a constant amount of power, the ratio shows how much the maximum intensity of the beam changes for different beam parameters. The data in Fig. 5.3 shows that the maximum intensity of the beam changes smoothly as a function of d_2 and that for small drifts in d_2, the changes in the beam's maximum intensity are reasonable. Figure 5.4 shows a plot of the effective area of the beam as a function of d_1 (the distance from laser face to collimating lens). The effective area is given by the expression $\pi W_{0x} W_{0y}/2$. The intensity at the center of the beam waist, I_{max} is given by $I_{max} = \text{power}/\text{effective area}$. Figure 5.4 shows that the effective area of the beam is sharply peaked when $d_1 = f_a$, which means that the intensity is at a local minimum. If we asume that the laser was reasonably well-collimated when we did the initial optimization, we can deduce that the intensity of the laser at its focus will increase if the distance d_1 were to drift in the actual setup. Thus, any adjustment to d_1 should be accompanied by a reassessment of the power and waist of the beam hitting the AOM. The extent to which the beam is collimated can be evaluated visually by shining the beam on a wall that is about ∼1m away. The collimating lens on the laser is mounted on a mount that fits into a 40 turns/inch threaded hole. Adjustments to the collimation

are made by turning the lens holder. Based on my experience collimating the laser, I am relatively confident that I can get the lens holder to within 1/10 of a turn of where it needs to be to collimate the laser perfectly. An accuracy of 1/10 turn corresponds to getting the distance d_1 to within 0.010 mm of the focal length of the collimating lens. Clearly, this places d_1 somewhere within the main spike on the plot in Figure 5.4, but it does not lend enough confidence in the repeatability of this adjustment to allow an experimenter to forego reassessing the beam parameters at the AOM.
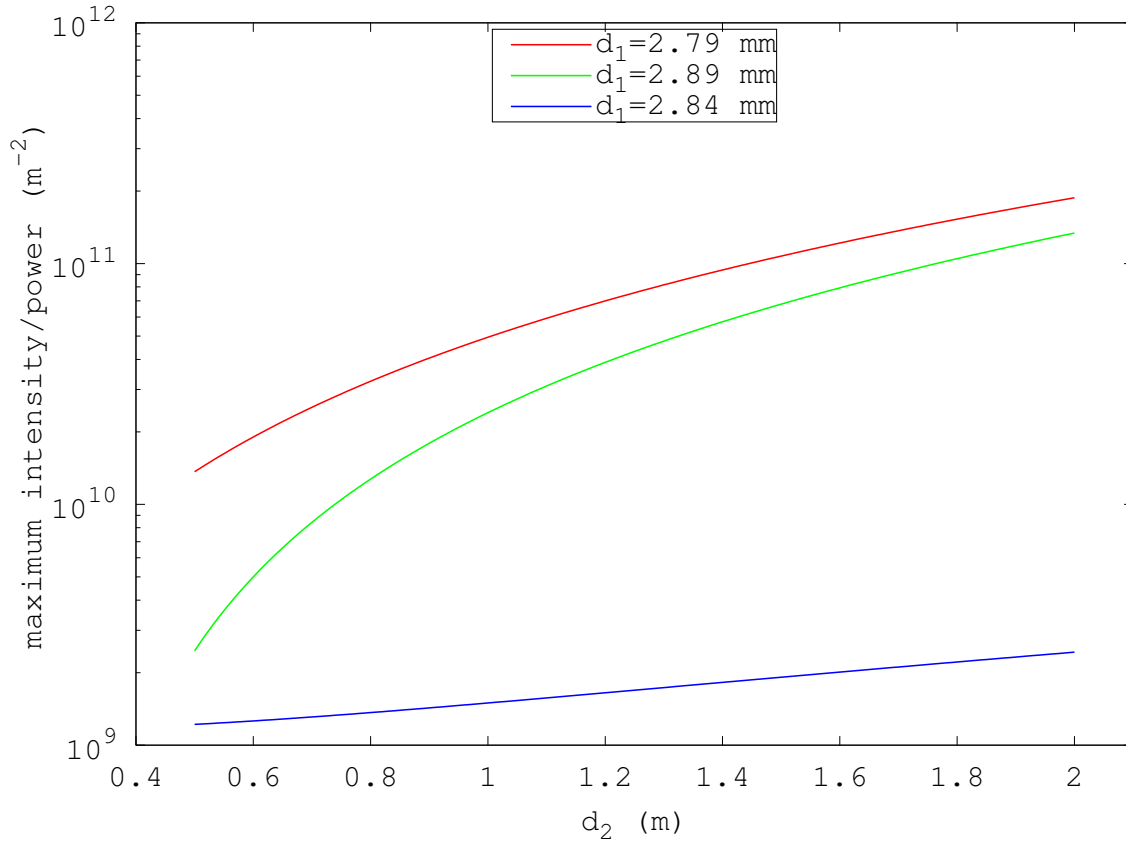
Figure 5.3   The ratio of the maximum intensity to the total beam power as a function of the distance between the laser's collimating lens and the focusing lens (d_2) plotted for several values of d_1, which is the distance between the laser diode's output face and the collimating lens. The maximum intensity divided by the total beam power is given by $2/(\pi W_{0x} W_{0y})$. Because it is difficult to measure d_2 accurately, we have plotted it over a very large range of possible values. However, the actual path length is likely to stay the same to within a few millimeters, over which scales the system is relatively insensitive to changes in d_2.
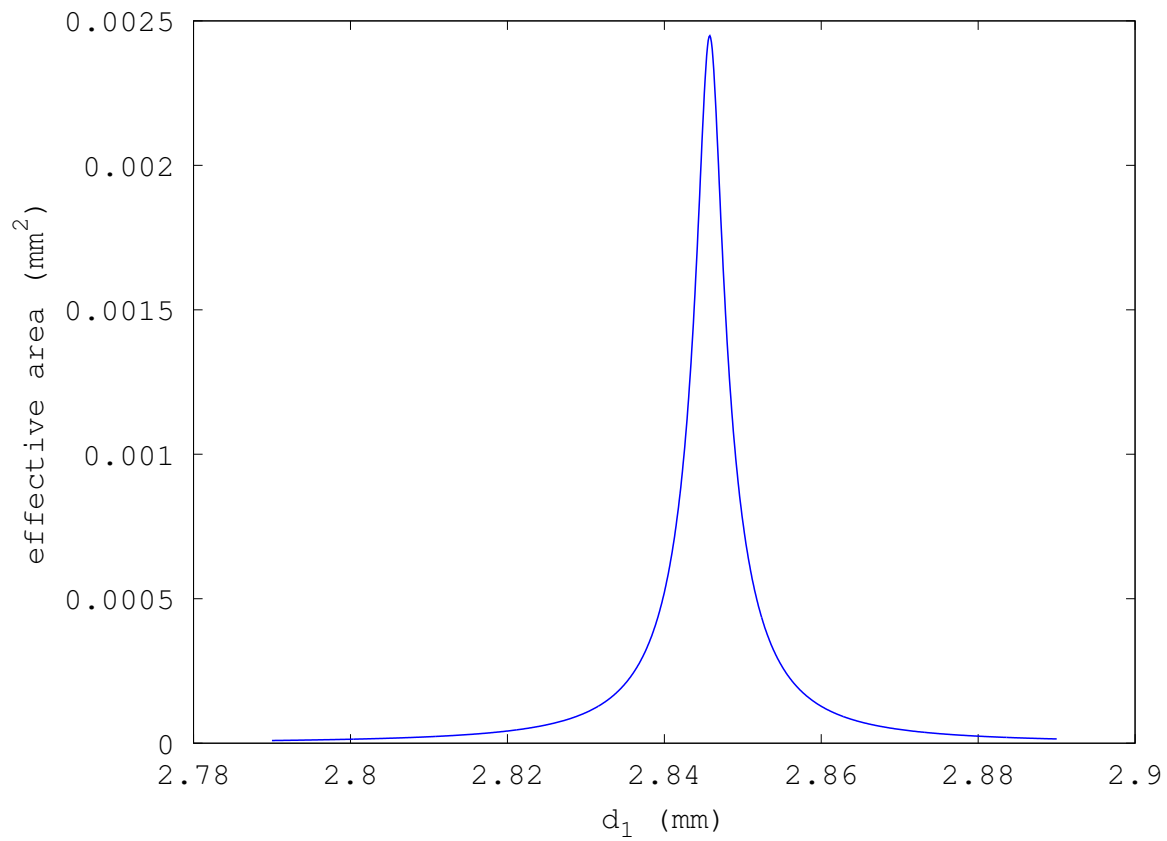
Figure 5.4 The effective beam area at the beam's focus as a function of the distance between the laser diode's output face and the collimating lens (d_1). Here, it is clear that the effective area is largest when d_1 equals the focal length of the laser's collimating lens. The peak intensity gets larger with any change of d_1.

Chapter 6

Injection Locking

Injection locking two slave lasers was necessary to get more power than would have been available from just the shifted beams from the master laser alone. In order to achieve injection locking, we must couple the first-order diffracted light that came out of the AOM into the laser cavities of each of the slave lasers. This is the first step in seeding the slave lasers with light from the master laser. The second step is to adjust the current and temperature of the slave lasers so that they achieve prolonged, single-mode operation in a mode that is in tune with the seed light.

6.1 Theory of operation

The laser operates on the principle of stimulated emission of radiation. In a non-injection-locked laser, the laser's output is determined by the interplay of several factors, including the resonant modes of the laser cavity and the spectral characteristics of the laser gain medium. "Mode competition" is the process whereby the power circulating in the laser concentrates in certain, more dominant modes at the expense of others. Since the gain saturation of the diode laser is determined largely by the rate at which electron-hole pairs can be created, it

is possible for one mode to dominate the other modes by reaching not only self-saturation, but cross-saturating the gain medium for the other modes [59]. This results in essentially single mode operation.

Therefore, intuitively, the goal of injection locking is to merely couple enough light into a suitable mode of the slave laser so that this mode has a slight advantage over the other modes.

6.2   Initial slave configuration

I selected the diodes for the slave lasers in the same manner in which I selected the master laser diode. I used the wavelength-selected diodes with the data I took on the Ocean Optics spectrometer. The setup and configuration of the slaves was very similar to what I did with the master laser, including all the part numbers and control electronics as described in Chapter 4.1.2. The slave lasers, however, have no diffraction grating. Rather than using grating feedback, the slave lasers achieve improved stability and wavelength control because they are injected with shifted light from the AOM, whose stability is determined by the stability of the master laser and the rf oscillator that drives the AOM.

6.3   Matching the mode properly

I optimized coupling to the laser diode by using the following technique: First, I turned off the slave lasers and disconnected them from their current supplies. Next, I used the slave laser diode as a photodiode. I coupled light from the AOM into the laser and measured the photocurrent produced by the laser. Better coupling between the beam from the AOM and the laser results in higher photocurrent coming out of the laser. In this way, I can conveniently align the optics.

I also adjusted the temperatures of the lasers in order to maximize the range of currents over which they would stay injected. When slave 2 was injection locked, the current produced when coupling the light in from the AOM was 8.2μA. The current at which it was working was 71.752 mA and the temperature was found to be 311.309K. Slave 1 worked properly at 72.979 mA and 30.026 K.

The amount of power being sent towards each slave (though, not necessarily being coupled in) is $\sim 90\mu W$. The slaves typically produce 48 mW to 63 mW.

Chapter 7

Results and Conclusions

The injection locking was successful and I successfully produced two working beams with an adjustable detuning. I have verified that both beams' frequencies are coupled to and offset from the master laser. Furthermore, the output from the slaves is sufficient to drive the transition.

7.1 Brief note on data from the spectrum analyzer

The main way that we can see if the lasers are working properly is to couple them to the spectrum analyzer, which was discussed in Section 2.3 and Appendix C. The spectrum analyzer is an optical cavity whose length is being changed as a function of time. A photodiode on the end of the spectrum analyzer captures a signal that is proportional to the transmission through the spectrum analyzer cavity. This signal is read on an oscilloscope.

For all of the data in this thesis, the length of the spectrum analyzer was modulated in a sawtooth pattern. Thus, the length of the cavity changed at a constant speed over some interval before being quickly brought back to its original length. A typical scan typically involves changing the length of the cavity by $\sim 3\mu$m.

The output of the photodiode is sent to an oscilloscope that is triggered by the frequency generator that also modulates the piezoelectric actuators on the spectrum analyzer. Therefore, typical data from the spectrum analyzer is a trace from an oscilloscope. The y axis represents signal from the photodiode, while the x dimension represents time elapsed since the last triggering event. The x axis values in the regimes shown in Figures 7.1 and 7.2 are also proportional to the change in length of the cavity becuase the cavity length is changing linearly as a function of time during the parts of the scan that I am showing. Because each sweep of the sawtooth function generator and piezo driver is identical, we can safely compare subsequent traces to track the relative frequency changes of any given peak.

If we scan about $\sim 2\mu$m, we expect that the peaks corresponding to our 408 nm lasers will go in in and out of resonance ~ 5 times. Therefore, we would expect that in the oscilloscope trace, the same peak should be repeated approximatly five times. For this cavity, the free spectral range is 187 MHz. This means that the distance between two peaks from the the same spectral component of the light in our scan will correspond to the distance that any given peak would move by if it were detuned by 187 MHz. This gives us a natural scale by which to judge the movement of peaks.

However, note that the detunings relevant to this experiment are on the order of GHz, which is much less than the free spectral range of the cavity. This simply means that two nearby peaks coming from different lasers are from different orders of longitudinal mode.

7.2   Tracking slave lasers with master laser

First, when we look at one slave and the master laser on the spectrum analyzer and scan the master laser, we see that the slave scans with the master laser. This is illustrated in Figure 7.1.

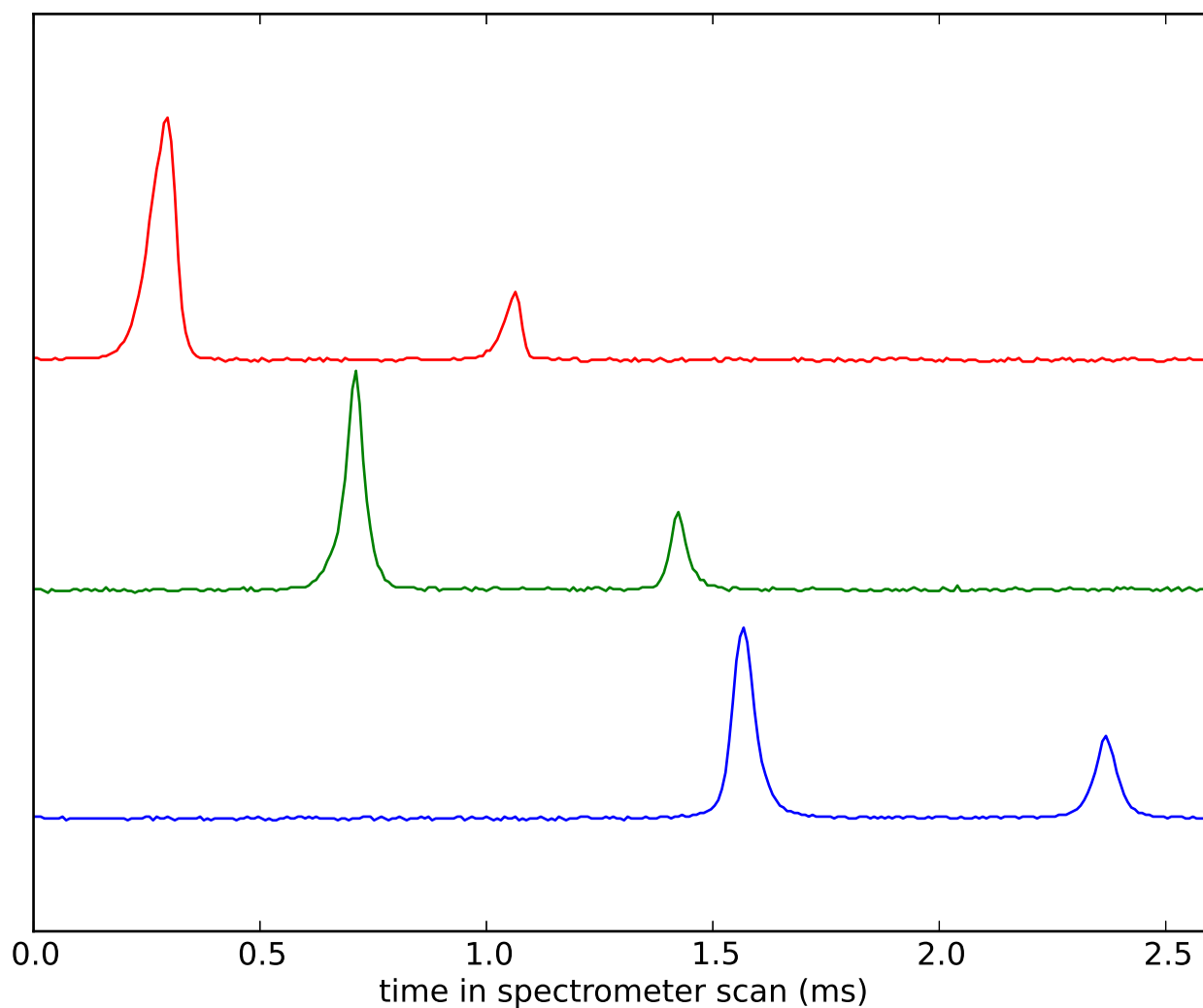**Figure 7.1** The slave and master laser on the spectrum analyzer. The y axis is the signal on the spectrum analyzer. There are three traces here, each showing the master laser at a different frequency. The slave laser is the taller peak, while the other peak belongs to the master laser. The peaks corresponding to the master laser and the slave laser move together. Each trace is offset in order to make it visible

7.3 Verifying that the slave frequencies can be adjusted with the RF oscillator

Second, I examined the output of the spectrum analyzer while both slave lasers were coupled into it. The two peaks clearly corresponded to the two slave lasers, which we verified by alternatively blocking each of the slaves.

I performed an experiment where I adjusted the driving frequency of the rf frequency generator that drives the AOM. I observed that the peaks on the spectrum analyzer shifted by an amount corresponding to the change in the frequency of the rf oscillator. This provides strong evidence that the two slaves were, indeed, injection locked to the modulated beams coming out of the AOM. This data is presented in Figure 7.2.

We have shown that we can change the rf oscillator frequency and thereby change the detuning. There are two limiting factors on the extent that we can do this. (Notice in Fig. 7.2 that the peaks get small as we continue to detune.) Both factors are geometrical in nature: First, the AOM diffraction efficiency decreases because the Bragg angle changes. Second, the diffraction angle changes, leading to a misalignment of the injected beams and a weakening of injection. However, even for large detunings, the injection lock can be achieved simply by realigning the output beams. We demonstrated this by successfully tuning the AOM driving frequency to the point where injection was lost, realigning (using the lasers as photodiodes) and then reachieving successful injection lock.

7.4 Summary and future work

To summarize: I have built a laser system capable of driving stimulated Raman transitions between the $F = 4$ and $F = 5$ hyperfine levels of $^{87}Sr^+$. I successfully tuned and stabilized
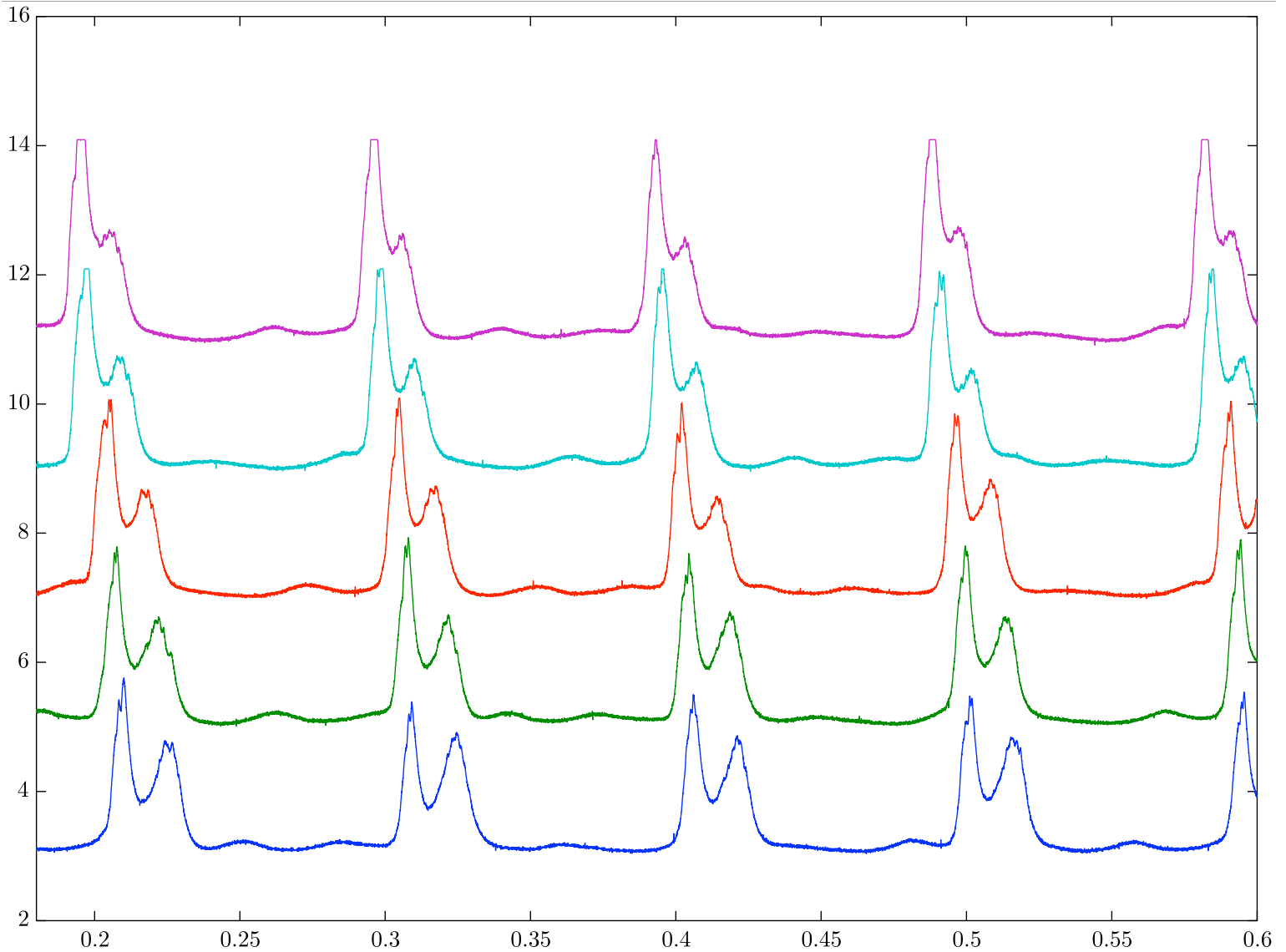
Figure 7.2 Scans of slave lasers for several rf oscillator frequencies. I changed the detuning on the frequency generator in 10 MHz increments between capturing each of these traces. The y axis represents transmission through the spectrum analyzer cavity as measured by the photodiode and is presented in arbitrary units with the traces offset to enhance visibility. The x axis represents time during the cavity scan. As the detuning changes, the distance between the two peaks shifts, thereby proving that the detuning between the slave laser and the master laser is controlled by the AOM and rf frequency generator.

the master laser. Using an AOM, I generated two shifted beams that I used to injection lock two other lasers (slave 1 and slave 2).

In order to ensure that the 408 nm 5 GHz detuned laser system works, we will need to actually drive stimulated Raman transitions in $^{87}Sr^+$. Completion of this requires the completion of the LVIS and other parts of the experiment. Getting the transition rate right will also likely require tweaks to many of the parameters of the current system. There are also additional optics that need to be installed to get the beams produced by this laser system to the atomic chamber. We will need to split the beams and then install optics to control their phase.

The 408 nm 5GHz detuned laser system could be improved in many ways. One thing that would be a great benefit is to increase the amount of time that the laser can operate without mode hopping. There was a technique described in Ref. [60] for improving the stability of an ECDL by creating a closed feedback loop to monitor and minimize the laser's amplitude noise. I developed some circuitry and took some data to investigate a variation on this which could potentially be applied to injection locked lasers, but this is not included in this thesis.

Bibliography

[1] C. J. Erickson, Ph.D. thesis, Brigham Young University, 2011.

[2] Z. T. Lu, K. L. Corwin, M. J. Renn, M. H. Anderson, E. A. Cornell, and C. E. Wieman, "Low-Velocity Intense Source of Atoms from a Magneto-optical Trap," Phys. Rev. Lett. **77,** 3331–3334 (1996).

[3] D. S. Durfee, proposal submitted to the NSF (unpublished).

[4] M. A. Kasevich and S. Chu, "Atomic Interferometry Using Stimulated Raman Transitions," Phys. Rev. Lett. **67,** 181–184 (1991).

[5] B. Young, M. Kasevich, and S. Chu, "Precision Atom Interferometry with Light Pulses," in *Atom Interferometry*, P. R. Berman, ed., (Academic Press, San Diego, 1997), pp. 363 – 406.

[6] L. Mach, "Ueber einen Interferenzrefraktor," Zeitschrift fr Instrumentenkunde **12,** 89–93 (1892).

[7] L. Zehnder, "Ein neuer Interferenzrefraktor," Zeitschrift fr Instrumentenkunde **11,** 275285 (1891).

[8] C. Davisson and L. H. Germer, "Diffraction of Electrons by a Crystal of Nickel," Phys. Rev. **30,** 705–740 (1927).

[9] I. Estermann and A. Stern, "Beugung von molekular-strahlen (bending of molecular rays)," Z. Phys 61 (1930).

[10] A. D. Cronin, J. Schmiedmayer, and D. E. Pritchard, "Optics and interferometry with atoms and molecules," Rev. Mod. Phys. **81,** 1051–1129 (2009).

[11] L. Marton, "Electron Interferometer," Phys. Rev. **85,** 1057–1058 (1952).

[12] H. Rauch and J. Summhammer, "Neutron-interferometer absorption experiments in the quantum limit," Phys. Rev. A **46,** 7284–7287 (1992).

[13] D. W. Keith, C. R. Ekstrom, Q. A. Turchette, and D. E. Pritchard, "An interferometer for atoms," Phys. Rev. Lett. **66,** 2693–2696 (1991).

[14] O. Carnal and J. Mlynek, "Young's double-slit experiment with atoms: A simple atom interferometer," Phys. Rev. Lett. **66,** 2689–2692 (1991).

[15] M. Arndt, O. Nairz, J. Vos-Andreae, C. Keller, G. van der Zouw, and A. Zeilinger, "Wave-particle duality of C60 molecules," Nature **401,** 680–682 (1999).

[16] B. Brezger, L. Hackermüller, S. Uttenthaler, J. Petschinka, M. Arndt, and A. Zeilinger, "Matter-Wave Interferometer for Large Molecules," Phys. Rev. Lett. **88,** 100404 (2002).

[17] I. I. Rabi, J. R. Zacharias, S. Millman, and P. Kusch, "A New Method of Measuring Nuclear Magnetic Moment," Phys. Rev. **53,** 318–318 (1938).

[18] N. F. Ramsey, "A Molecular Beam Resonance Method with Separated Oscillating Fields," Phys. Rev. **78,** 695–699 (1950).

[19] C. J. Bordé, "Atomic Interferometry with Internal State Labelling," Physics Letters A **140,** 10–11 (1989).

[20] A. Wicht, J. M. Hensley, E. Sarajlic, and S. Chu, "A Preliminary MeasMeasure of the Fine Structure Constant Based on Atom Interferometry," Physica Script **T102,** 82–88 (2002).

[21] D. S. Weiss, B. C. Young, and S. Chu, "Precision measurement of the photon recoil of an atom using atomic interferometry," Phys. Rev. Lett. **70,** 2706–2709 (1993).

[22] K. Gibble, "Difference between a Photon's Momentum and an Atom's Recoil," Phys. Rev. Lett. **97,** 073002 (2006).

[23] H. Müller, S.-w. Chiow, S. Herrmann, S. Chu, and K.-Y. Chung, "Atom-Interferometry Tests of the Isotropy of Post-Newtonian Gravity," Phys. Rev. Lett. **100,** 031101 (2008).

[24] P. W. Graham, J. M. Hogan, M. A. Kasevich, and S. Rajendran, "New Method for Gravitational Wave Detection with Atomic Sensors," Phys. Rev. Lett. **110,** 171102 (2013).

[25] K.-Y. Chung, S.-w. Chiow, S. Herrmann, S. Chu, and H. Müller, "Atom interferometry tests of local Lorentz invariance in gravity and electrodynamics," Phys. Rev. D **80,** 016002 (2009).

[26] S. M. Dickerson, J. M. Hogan, A. Sugarbaker, D. M. S. Johnson, and M. A. Kasevich, "Multiaxis Inertial Sensing with Long-Time Point Source Atom Interferometry," Phys. Rev. Lett. **111,** 083001 (2013).

[27] T. Kurosu and F. Shimizu, "Laser Cooling and Trapping of Calcium and Strontium," Japanese Journal of Applied Physics **29,** L2127 (1990).

[28] A. D. Ludlow *et al.,* "Sr Lattice Clock at 1 1016 Fractional Uncertainty by Remote Optical Evaluation with a Ca Clock," Science **319,** 1805–1808 (2008).

[29] M. Kovarik, "Cavendishs phenomenological derivation of Coulombs law,", 2012, retrieved 2015-08-12.

[30] J. D. Jackson, *Electrodynamics– 3rd ed.* (Wiley, 1999).

[31] D. Christensen, B. Neyenhuis, and D. S. Durfee, "Numerical calculation of classical and non-classical electrostatic potentials," ArXiv Physics e-prints (2006).

[32] B. Neyenhuis, D. Christensen, and D. S. Durfee, "Testing Nonclassical Theories of Electromagnetism with Ion Interferometry," Phys. Rev. Lett. **99,** 200401 (2007).

[33] G. Spavieri, J. Quintero, G. T. Gillies, and M. Rodrguez, "A survey of existing and proposed classical and quantum approaches to the photon mass," The European Physical Journal D **61,** 531–550 (2011).

[34] C. J. Erickson, M. V. Zijll, G. Doermann, and D. S. Durfee, "An ultrahigh stability, low-noise laser current driver with digital control," Rev. Sci. Instrum. 79 (2008).

[35] D. L. Troxel, C. J. Erickson, and D. S. Durfee, "Note: Updates to an ultar-low noise laser current driver," Rev. Sci. Instrum. 82 (2011).

[36] T. L. Gustavson, Ph.D. thesis, Stanford University, 2000.

[37] C. J. Foot, *Atomic Physics, Oxford Master Series in Atomic, Optical and Laser Physics* (Oxford University Press, Great Clarendon Street, Oxford OX2 6DP, 2005).

[38] E. A. Korsunsky, "Atomic beamsplitter based on Raman transitions in four standing light waves," Quantum Semiclass. Opt. **10,** 477–483 (1998).

[39] C. Cohen-Tannoudji, J. Dupont-Roc, and G. Grynberg, *Atom-Photon Interactions: Basic Processes and Applications* (John Wiley & Sons, Inc., 1992).

[40] D. P. D. Dmitry Budker, Derek F. Kimball, *Atomic Physics: An exploration through problems and solutions*, 2nd ed. (Oxford University Press, 2008).

[41] J. J. Sakurai, in *Modern Quantum Mechanics*, S. F. Tuan, ed., (Addison-Wesley Publishing Company, Inc., 1994).

[42] E. Merzbacher, *Quantum Mechanics* (John Wiley & Sons, Inc., 1998).

[43] E. Brion, L. H. Pedersen, and K. M?lmer, "Adiabatic elimination in a lambda system," Journal of Physics A: Mathematical and Theoretical **40,** 1033 (2007).

[44] E. Arimondo, M. Inguscio, and P. Violino, "Experimental determinations of the hyperfine structure in the alkali atoms," Rev. Mod. Phys. **49,** 31–75 (1977).

[45] D. Kleppner, D. E. Pritchard, J. Doyle, and W. Ketterle, "Physics 8.421 Lecture Notes,", 2006.

[46] Y. Ralchenko, A. E. Karmida, J. Reader, and et. al., "NIST Atomic Spectra Database (version 3.1.5),", 2008.

[47] C. Schwartz, "Theory of Hyperfine Structure," Phys. Rev. **97,** 380–395 (1955).

[48] W. Xiao-Li, Y. Kai-Zhi, G. Bing-Cong, and Z. Meng, "Calculations on the hyperfine constants of the ground states for lithium-like system," Chinese Physics **16,** 2389 (2007).

[49] I. I. Sobelman, *Atomic Spectra and Radiative Transitions* (Springer Berlin Heidelberg, 1992).

[50] G. Racah, "Theory of Complex Spectra. II," Phys. Rev. **62,** 438–462 (1942).

[51] M. S. Safronova, W. R. Johnson, and U. I. Safronova, "Two-photon transitions in Ca+, Sr+ and Ba+ ions," J. Phys. B: At. Mol. Opt. Phys. 43 (2010).

[52] D. DeMille, not sure who authored this. (unpublished).

[53] SymPy Development Team, *SymPy: Python library for symbolic mathematics*, 2014.

[54] J. Rasch and A. Yu, "Efficient Storage Scheme for Pre-calculated Wigner 3j, 6j and Gaunt Coefficients," SIAM J. Sci. Comput. **25,** 1416–1428 (2003).

[55] P. W. Milonni and J. H. Eberly, *Laser Physics* (John Wiley & Sons, Inc., 2010).

[56] A. E. Siegman, "How to (Maybe) Measure Laser Beam Quality," DPSS Lasers: Applications and Issues 17 (1998).

[57] J. Peatross and M. Ware, *Physics of Light and Optics* (2009).

[58] "Gaussian Beam Optics,".

[59] "Gain Saturation in RP Photonics Encyclopedia,".

[60] S. wey Chiow, Q. Long, C. Vo, H. Müller, and S. Chu, "Extended-cavity diode lasers with tracked resonances," Appl. Opt. **46,** 7997–8001 (2007).

[61] S. D. Bergeson, "Physics 571 Lecture 4,".

Appendix A

Measuring Beam Waist

Sometimes it's important to measure the waist of one's laser beam. This explains the exact method we use.

The profile for the intensity of the beam is given by

$$I(r, z) = I_0 \left(\frac{w_0}{w(z)} \right)^2 \exp\left(\frac{-2r^2}{w^2(z)} \right) \tag{A.1}$$

Extrapolating this to when there are two different waists in different directions, we get:

$$I(r, z) = (\text{constants}) \exp\left(-2 \frac{x^2}{w_x^2(z)} - 2 \frac{y^2}{w_y^2(z)} \right). \tag{A.2}$$

Now, total power (P) can be obtained by integrating the the intensity:

$$P = \int_{-\infty}^{\infty} \int_{-\infty}^{\infty} (\text{constants}) \exp\left(-2 \frac{x^2}{w_x^2(z)} - 2 \frac{y^2}{w_y^2(z)} \right) dxdy \tag{A.3}$$

$$P = \frac{\pi}{2} (\text{constants}) w_x(z) w_y(z) \tag{A.4}$$

Now, we figure out that those constants will be

111

$$(\text{constants}) = \frac{2P}{\pi w_x(z)w_y(z)}. \tag{A.5}$$

The "constants" term represents the maximum intensity that occurs within the beam (i.e. when $x = y = z = 0$, or in other words, at the center of the narrowest part of the beam.)

Now, to take measurements with a knife, we block some fraction of the beam by mounting the knife on a translation stage. We then look at the amount of power from the beam hitting a photodiode that is placed downstream from the knife. If, for example, the knife is mounted vertically, the measurements on the photodiode correspond to the total power in the beam from $x = -\infty$ to x_0 where x_0 is the location of the knife. Thus, if we plot this power as a function of the spatial position of the knife, we expect that the result should be

$$P(x_0) = \int_{\infty}^{\infty} \int_{-\infty}^{x_0} \frac{2P}{\pi w_x(z)w_y(z)} \exp\left(-2\frac{x^2}{w_x^2(z)} - 2\frac{y^2}{w_y^2(z)}\right) dxdy \tag{A.6}$$

$$P(x_0) = \frac{P}{2}\left(\text{erf}\,\frac{\sqrt{2}x}{W_x} + 1\right) \tag{A.7}$$

So, now we have a function that we can fit. The code in masterFILEhoriz14Nov.m calculates the approximate beam waist based on a series of knife cuts. First, one loads the intensity (in arbitrary units) and the position (in the units that the waist will ultimately be given in) into a number of arrays named x1, x2, .. . etc. The user types the position of the knife along the waist (show picture) into the vector called positions.

The function d4sigma attempts to calculate the second moment width using just the raw data. This is notoriously inaccurate and also it is probably misnamed because it probably just calculates something that is different from the standard D4σ by some factor of 2 or something. Also, we don't use this.

Ultimately, the program does a best fit approximation to a Gaussian for each beam

profile. The function we fit to is contained in the file beamWaistCalculator, which takes as its arguments the raw position data and the raw intensity data. This function is

$$f(x) = a_1 \operatorname{erf}\left(\frac{x - a_3}{a_2}\right) + a_4. \tag{A.8}$$

beamWaistCalculator thus returns a vector containing $(a_1 a_2 a_3 a_4)$. Thus, to get the beam waist, we will take a_2 and multiply by $\sqrt{2}$.

According to Siegman [56], the second moment width always propagates according to this equation:

$$W_x^2(z) = W_{0x}^2 + M_x^4 \left(\frac{\lambda}{\pi W_{0x}}\right)^2 (z - z_{0x})^2. \tag{A.9}$$

Of course, for a Gaussian beam, we recognize that allowing $M_x^2 \to 1$ gives us the equation for how the waist changes as it propagates.

This function then tries to fit to this:

$$W_x = a_1 \sqrt{1 + \left(\frac{(x - a_2)\lambda}{\pi a_1^2}\right)^2} \tag{A.10}$$

and this:

$$W_x = a_1 \sqrt{1 + (1 + a_3^2)\left(\frac{(x - a_2)\lambda}{\pi a_1^2}\right)^2}. \tag{A.11}$$

The first case we are forcing M^2 to be one. This gives us a worst-case scenario. A few test cases convinced us that if M^2 is higher than we think it is, we have a less-tightly focused center. Thus, for the purposes of not putting too much power into the AOM, we go with the fit to the first equation.

In principle, we should be able to fit the calculated second moment widths to the equations above, but they don't work overly well. Thus, we usually use the second moment width of the Gaussian we fit it to.

Using this method, we have determined the waist to be
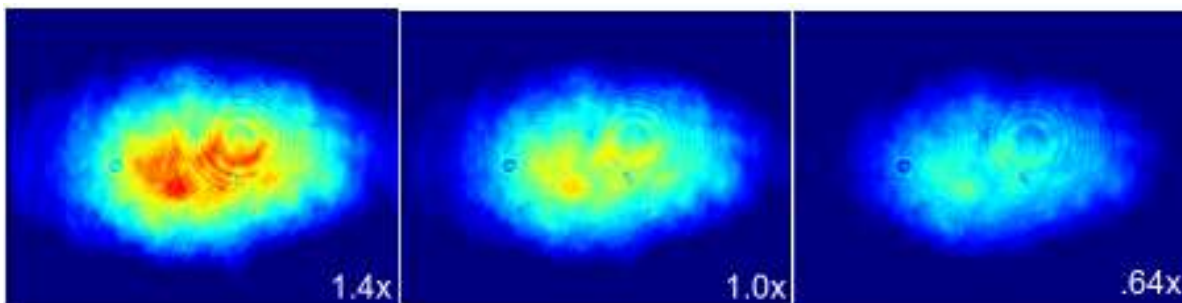
Figure A.1 Three images taken using the camera. Each was the same laser beam with the attenuation adjusted using our waveplate and polarizer setup. The total power was measured using a photodiode and the relative total power is shown in the lower right corner of each image. By comparing the pixel values of similar spots within the image, we were able to bootstrap some calibration parameters for the camera.

A.1   Using the camera

We initially wanted to measure the M^2 of our beam. The measurements are hard to do accurately. We tried to use the camera and got results that were not entirely usable.

A.1.1   Investigation of feasibility of using the camera

The camera seems like an appealing device to use to measure beam parameters since it can take large amounts of 2D data quickly.

To investigate the camera's feasibility, we wanted to verify that the camera was (a) linear and (b) that each pixel reading was independent of the rest of the image. To this end, we took several images of the same beam, which we attenuated using the polarizing beam cube/waveplates adjustable attenuator setup described in Appendix D. We took 20 measurements. Each time we measured the total intensity of the beam using a photodiode and we took a corresponding image of the beam

Our idea was that, if the camera is linear and the pixels act independently, the following statements should be true:

- The ratio of the reading on any pixel to the reading on the same pixel in a different image should be equal to the ratio of the total power of the two beams used in the two readings as measured by the photodiode.

- Any two pixels reporting the same number of counts are experiencing the same radiance.

Thus, for example, if we see that the pixel located at $(214, 442)$ has a pixel count of 127 in image 15, on which we measured the intensity to be proportional to 85.350, then we assume that we can compare it directly to a pixel located at the same location $(214, 442)$ on image 20 (which had an intensity proportional to 119.70). If the reading from the $(214, 442)$ pixel on image 20 was 155.46, we assume that a pixel count of 155.46 corresponds to $119.70/85.350 = 1.4025$ times as much intensity as a pixel count of 127. Additionally, we assume that any pixel we find in any of the images that reports a reading of 155.45 will have the same intensity as any other.

We went through the 20 images like this: We selected some reference pixel. We then added that pixel to a master list. We then found the corresponding pixels in the other images whose position on the grid match that of the reference pixel. They were then added to the master list, making note of their position, the reading on the pixel (count) and the assumed ratio between the amount of light hitting that pixel and the amount of light hitting reference pixel as inferred based on the readings from the photodiode.

Then, we select a random pixel from the master list and look for other pixels that have the same number of counts within any of the images. If a pixel has the same reading (number of counts) as the randomly selected pixel in the master list, it is added to the master list. Since this new pixel has the same counts as the randomly selectd pixel, we assume that the pixels have the same radiance relative to the reference pixel. Once the new pixel is added to the maseter list, we find the corresponding pixels from the other images and add them to

our list. We assume that the true irradiance at these pixels is proportional to the irradiance of pixel we just added.

In this way, we create a very long list of pixels, their counts and what we have inferred about the incident illumination of each pixel by comparing it to (a) other pixels that read the same value and (b) pixels in other images of different intensities. Note that the pixels in the list are not unique. Pixels can appear multiple times in the list.

If we plot the expected pixel count (as calculated by taking the reading on the main reference pixel and multiplying it by the relative radiance factors that we've been tracking) vs the actual pixel count, we get the plot in Fig. A.2, which seems to validate the assumption of pixel independence.

However, as one can see, the camera actually has a minimumt threshold below which it does not report light very well. Because the camera throws away information and has a minimum intensity threshold to register, we throw out any $M_{ij} = 0$. This way our function doesn't get penalized for showing a non-zero intensity for pixels that read out zero. The number of $M_{ij} = 0$ obviously doesn't change as we try different iterations of $f(M_{ij})$, so there's no way to game our little metric to make it not work.

We performed a curve fit to model our pixels response. In order to do this, we had to devise a cost function that produces some figure of merit to tell us whether our test function is succeeding at making all of the pixels have the right ratio. The way it works is this: Suppose that M_{ij} is a big list of our pixels. j runs from 1 to 20, corresponding to the 20 different images. i represents all the pixels in our image[1]. Let $f(p)$ be the proposed function that takes as its argument the count on a given pixel and gives as its output something that scales with the actual intensity of the light. The figure of merit that we can use to optimize

---

[1]Thus, if we are analyzing 8x8 bins, we should have 480/8*640/8=4800 pixels and i will range between 1 to 4800

$f(p)$ is calculated as follows:

$$\text{Figure of merit} = \sum_{M_{ij} \neq 0} \left(\frac{f(M_{ij})/P_j}{\text{average of all nonzero } f(M_{ij})/P_j \text{ for the ith pixels}} - 1 \right)^2 \quad \text{(A.12)}$$

where P_j is the power of the jth image.

In words, Eq. A.12 can be described as follows: First, act on the pixels with the proposed function. Then, scale them according to the intensity ratios (i.e. the ith pixel in image 1 gets divided by P_1 while the ith pixel in image 3 gets divided by P_3). Then, see by what fraction the intensity of that pixel differs from the average of the intensities calculated using data from the pixels corresponding to that one. If the function really were to find the ratio perfectly, then $f(M_{ij})/P_j$ should be exactly the same for the ith pixel from each of the j images.

We used this function to calculate what correction function to use. We did a couple of them and found great agreement with the inversion of the previous function–thus suggesting that our previous method was acceptable.

In the end, the camera offset and nonlinearity made it unsuitable for sensitive measurements of the second moment width of the beam. However they did provide a reasonable sanity check on our methods.
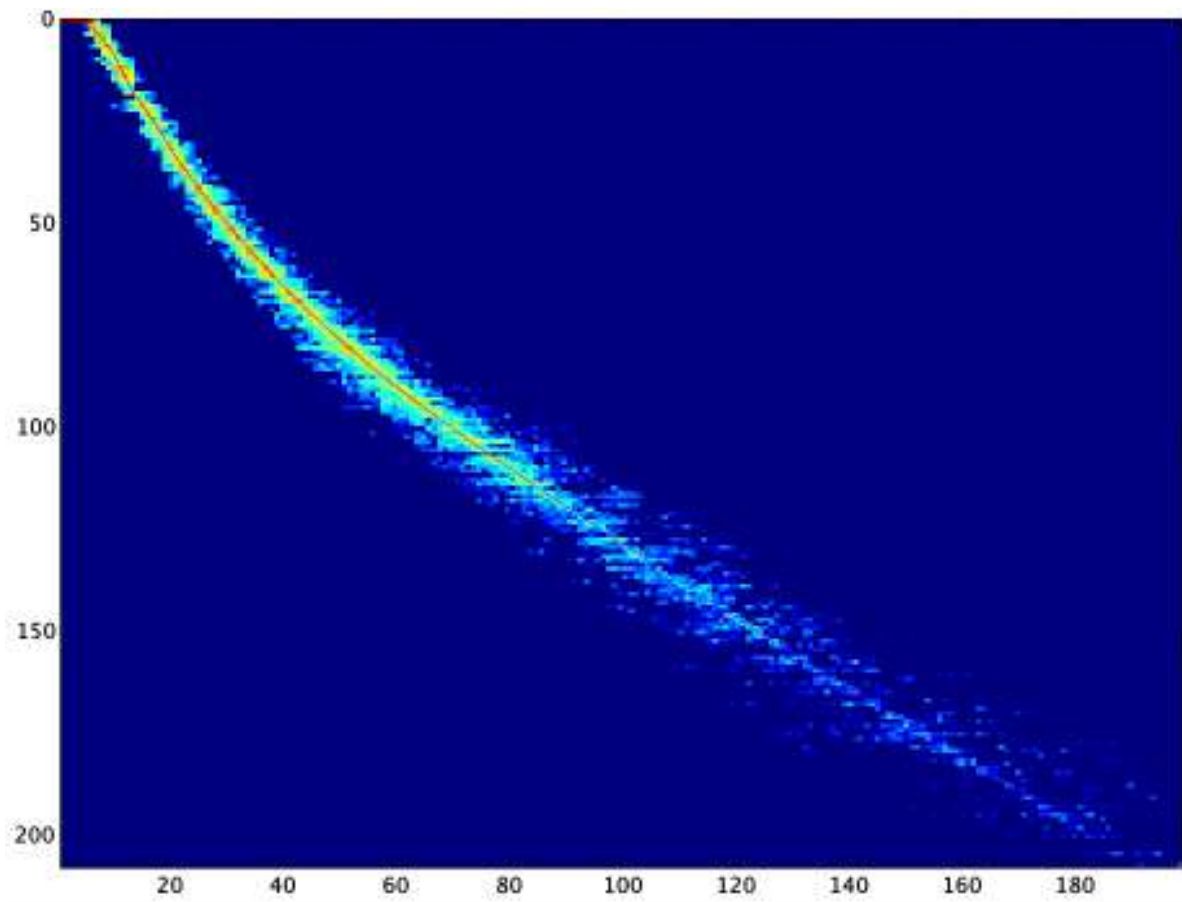
Figure A.2 On the x axis is the inferred pixel reading based on our assumptions about the ratios of pixel readings. On the y axis, we can see the actual readings of the pixels. This illustrates clearly the threshold issue of the camera. In the top, left side of the plot, there is clearly a region where our inferred readings should be nonzero, but the actual readings on the camera remain at zero.

Appendix B

Optimizing Motion of External Cavity Grating

In order to narrow the linewidth of the master laser and make it more tunable and stable, we have mounted a diffraction grating in a Littrow configuration. The gratings are mounted on piezoelectric actuators that can be automatically moved in unison by our control circuitry.

However, in order for this to work, it is important to verify that the piezos can be scanned in such a way that the resonances of the external cavity track smoothly. In order to accomplish this, one must find a ratio that relates the relative rates at which each piezoelectric actuator is scanned. As explained in Section 4.1.5, the length of the cavity and the angle of the grating must change in such a way that the wavelength featured by each changes at the same rate for small displacements.

For many configurations, this is not very tricky. However, at one point we discovered that for certain geometries, the appropriate ratio might be negative. To this end, we created the following Mathematica notebook to model the motion of the grating and help us to ensure that our electronics are capable of moving the actuators properly.

In practice, the results of this calculation would typically be used only as a starting point. In order to really get the laser working well, the experimenter usually adjusts the ratio iteratively in order to maximize the range over which the frequency of the laser can be scanned without modehopping.

Function Definitions

In[1]:= `(*change in angle due to piezos*)`

$$\Delta\theta[\text{x1\_, x2\_}] = \frac{\text{x2}-\text{x1}}{q};$$

`(*the location of the pivot point between the piezo actuators*)`

$$\text{Py}[\text{x1\_, x2\_}] = \frac{\text{x2}+\text{x1}}{2};$$

`(*the vector going from  the pivot point to the plane of`
`   the grating. It is perpendicular to the plane of the piezos.*)`

$$\text{ax}[\text{x1\_, x2\_}] = a\,\text{Cos}\left[\frac{\pi}{2}+\Delta\theta[\text{x1, x2}]\right];$$

$$\text{ay}[\text{x1\_, x2\_}] = a\,\text{Sin}\left[\frac{\pi}{2}+\Delta\theta[\text{x1, x2}]\right];$$

`(*a vector pointing along the direction of the plane of the grating*)`

$$\xi\text{x}[\text{x1\_, x2\_, }\xi\_] = \xi*\text{Cos}[\theta 1+\Delta\theta[\text{x1, x2}]];$$

$$\xi\text{y}[\text{x1\_, x2\_, }\xi\_] = \xi*\text{Sin}[\theta 1+\Delta\theta[\text{x1, x2}]];$$

`(*a vector representing where the laser hits the grating*)`

$$\text{Lx}[\text{x1\_, x2\_, }\xi\_] = \text{ax}[\text{x1, x2}]+\xi\text{x}[\text{x1, x2, }\xi];$$

$$\text{Ly}[\text{x1\_, x2\_, }\xi\_] = \text{ay}[\text{x1, x2}]+\xi\text{y}[\text{x1, x2, }\xi]+\text{Py}[\text{x1, x2}];$$

Solve the equation

In[9]:= `(*solve. α represents how much  the cavity is shortened by. Essentially,`
`   we say that the new place where the laser is striking the`
`    grating (Lx[x1,x2,ξ]) is equal to the old place (Lx[0,0,ξ0]) plus`
`    some  amount  α pointed in the direction of the laser beam *)`

$$\text{eq1} = \text{Lx}[\text{x1, x2, }\xi] == \text{Lx}[0, 0, \xi 0]+\alpha\,\text{Cos}[\theta\text{L}]$$

$$\text{eq2} = \text{Ly}[\text{x1, x2, }\xi] == \text{Ly}[0, 0, \xi 0]+\alpha\,\text{Sin}[\theta\text{L}]$$

Out[9]= $\xi\,\text{Cos}\left[\dfrac{-\text{x1}+\text{x2}}{q}+\theta 1\right] - a\,\text{Sin}\left[\dfrac{-\text{x1}+\text{x2}}{q}\right] == \xi 0\,\text{Cos}[\theta 1]+\alpha\,\text{Cos}[\theta\text{L}]$

Out[10]= $\dfrac{\text{x1}+\text{x2}}{2}+a\,\text{Cos}\left[\dfrac{-\text{x1}+\text{x2}}{q}\right]+\xi\,\text{Sin}\left[\dfrac{-\text{x1}+\text{x2}}{q}+\theta 1\right] == a+\xi 0\,\text{Sin}[\theta 1]+\alpha\,\text{Sin}[\theta\text{L}]$

Define some convenient functions based on the solution

αFUNCT is the function representing how much shorter the cavity gets depending on x1 and x2. ξFUNCT tells you how far along the grating you need to go from your center point to get there. It is mostly just a maintenance function

In[11]:= `Solve[{eq1, eq2}, α, ξ];`
`αFUNCT[x1_, x2_] = %[[1, 1, 2]] // Simplify`
`Solve[{eq1, eq2}, ξ, α];`
`ξFUNCT[x1_, x2_] = %[[1, 1, 2]] // Simplify`

Solve::bdomv : Warning : ξ is not a valid domain specification . Assuming it is a variable to eliminate . $\gg$

Out[12]= $\frac{1}{2} \text{Csc}\left[\frac{x1 - x2 - q\,\theta1 + q\,\theta L}{q}\right] \left(2\,a\,\text{Cos}[\theta1] + (-2\,a + x1 + x2)\,\text{Cos}\left[\frac{x1 - x2 - q\,\theta1}{q}\right] - 2\,\xi0\,\text{Sin}\left[\frac{x1 - x2}{q}\right]\right)$

Solve::bdomv : Warning : α is not a valid domain specification . Assuming it is a variable to eliminate . $\gg$

Out[14]= $\frac{1}{2} \text{Csc}\left[\frac{x1 - x2 - q\,\theta1 + q\,\theta L}{q}\right] \left((-2\,a + x1 + x2)\,\text{Cos}[\theta L] + 2\,a\,\text{Cos}\left[\frac{x1 - x2 + q\,\theta L}{q}\right] - 2\,\xi0\,\text{Sin}[\theta1 - \theta L]\right)$

Now, use the condition that the change in λ due to the changing grating angle must match the change in λ due to the change in cavity length

In[15]:= `(*this is the change in λ due to the change in cavity`
`    length (recall αFUNCT is how much  SHORTER the cavity is*)`
$\delta\lambda1 = -\dfrac{\alpha\text{FUNCT}[x1, x2]}{L}\,\lambda$
`(*this is the change in λ because of the change in the grating's angle*)`
`(*I believe the convention is that a larger Δθ corresponds to the`
`  grating angling away from  the light, meaning  it favors longer λs*)`
$\delta\lambda2 = 2\,d\,\text{Sin}\big[\text{grating}\theta + \Delta\theta[x1, x2]\big] - 2\,d\,\text{Sin}\big[\text{grating}\theta\big]$

Out[15]= $-\frac{1}{2\,L}\lambda\,\text{Csc}\left[\frac{x1 - x2 - q\,\theta1 + q\,\theta L}{q}\right] \left(2\,a\,\text{Cos}[\theta1] + (-2\,a + x1 + x2)\,\text{Cos}\left[\frac{x1 - x2 - q\,\theta1}{q}\right] - 2\,\xi0\,\text{Sin}\left[\frac{x1 - x2}{q}\right]\right)$

Out[16]= $-2\,d\,\text{Sin}[\text{grating}\theta] + 2\,d\,\text{Sin}\left[\text{grating}\theta + \frac{-x1 + x2}{q}\right]$

Now, the change in λ due to both the changing angle and the changing cavity length should be the same. Thus, subtracting these two should give us a constant number.

In[17]:= `aBigConstant = δλ1 - δλ2`

Out[17]= $2\,d\,\text{Sin}[\text{grating}\theta] - \frac{1}{2\,L}$
$\lambda\,\text{Csc}\left[\frac{x1 - x2 - q\,\theta1 + q\,\theta L}{q}\right] \left(2\,a\,\text{Cos}[\theta1] + (-2\,a + x1 + x2)\,\text{Cos}\left[\frac{x1 - x2 - q\,\theta1}{q}\right] - 2\,\xi0\,\text{Sin}\left[\frac{x1 - x2}{q}\right]\right) -$
$2\,d\,\text{Sin}\left[\text{grating}\theta + \frac{-x1 + x2}{q}\right]$

In[18]:= `aBigConstant = aBigConstant //. x2 → myRATIO1 *x1;`
`D[aBigConstant, x1] //. x1 → 0;`
`Solve[% == 0, myRATIO1 ];`
`RATIO[λ_, a_, q_, θ1_, d_, L_, ξ0_] = %[[1, 1, 2]]`

Out[21]= $\left(4\,d\,L\,Cos[grating\theta] + 2\,\lambda\,\xi0\,Csc\left[\frac{-q\,\theta1 + q\,\theta L}{q}\right] - \right.$

$q\,\lambda\,Cos[\theta1]\,Csc\left[\frac{-q\,\theta1 + q\,\theta L}{q}\right] + 2\,a\,\lambda\,Csc\left[\frac{-q\,\theta1 + q\,\theta L}{q}\right]Sin[\theta1]\left.\right) \Big/$

$\left(4\,d\,L\,Cos[grating\theta] + 2\,\lambda\,\xi0\,Csc\left[\frac{-q\,\theta1 + q\,\theta L}{q}\right] + q\,\lambda\,Cos[\theta1]\,Csc\left[\frac{-q\,\theta1 + q\,\theta L}{q}\right] + \right.$

$\left. 2\,a\,\lambda\,Csc\left[\frac{-q\,\theta1 + q\,\theta L}{q}\right]Sin[\theta1]\right)$

This is a symbolic expression for the correct piezo ratio. We did it symbolically so that we can plot it in a couple of sections to make sure that our ratio isn't extremely sensitive to any of the variables we may not have measured very well.

Data about setup

```
(*wavelength*)
λ = 407.771 *10⁻⁹;
(*grating spacing*)
d = .001/3600;
(*the angle between the normal  of the grating
  and the laser that satisfies the diffraction condition*)
```
$gratingθ = ArcSin\left[\frac{\lambda}{2\,d}\right];$
```
(*the angle between the grating and the plane of the piezos-0 if mounted  flat,
whatever angle if mounted  otherwise*)
θ1 = gratingθ;
(*the angle between the laser and the plane of the piezo actuators
  (e.g. for Chris' setup, it's 90 degrees-grating angle. For my  setup,
   it's π/2 radians, in general, it will be )*)
θL = π/2;
(*When you're piezos are at rest,
this represents how far the point you hit the laser at is from  where the vector a
  points. Sort of how far off center you are measured  along the grating.*)
ξ0 = 0;
(*distance between piezo actuators*)
q = (.05972 + .03056)/2;
(*Thickness-distance from  plane of piezo to plane of grating going
    perpendicularly from  the midpoint  between piezo actuators*)
a = .025;
(*cavity length*)
L = .04;
```

Let's check to make sure that when we expand aBigConstant using our newly found ratio, we get what we think we should.

To first order, aBigConstant should not vary with x1.

In[31]:= `(*This is the ratio we think we should get for the setup described above*)`
`myRATIO  = RATIO[λ, a, q, θ1, d, L, ξ0]`

Out[31]= `0.478755`

In[32]:= `test1 = aBigConstant //. myRATIO1  -> myRATIO ;`
`Series[test1, {x1, 0, 4}]`

Out[33]= $-1.69407 \times 10^{-21} \, x1 - 0.0000294958 \, x1^2 + 0.000751895 \, x1^3 - 0.0136018 \, x1^4 + O[x1]^5$

Nice! It looks like the x1 coefficient is pretty close to zero, probably to within the working precision of the machine.

How RATIO changes as a function of the geometry

We will plot the correct value of RATIO for various likely experimental parameters. Some of the geometry cannot be measured with perfect accuracy, so we mostly want to make sure that the RATIO does not change in some radical way over the values we are likely to have. One example of something we would worry about is if the RATIO became negative for geometrical configurations close to ours since this would require modification of the circuitry that drives the piezo controls.
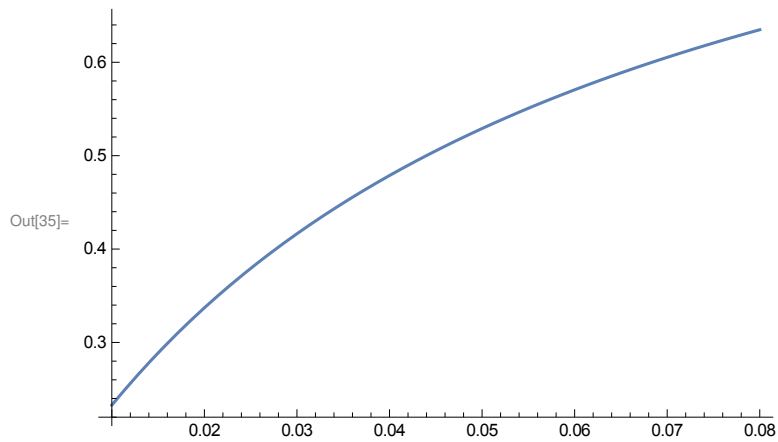
First, as a function of ax (the distance between the plane of the piezo actuators and the point where the laser strikes the plane of the grating)

In[34]:= `Plot[RATIO[λ, ax, q, θ1, d, L, ξ0], {ax, .002, .08}]`

Out[34]=
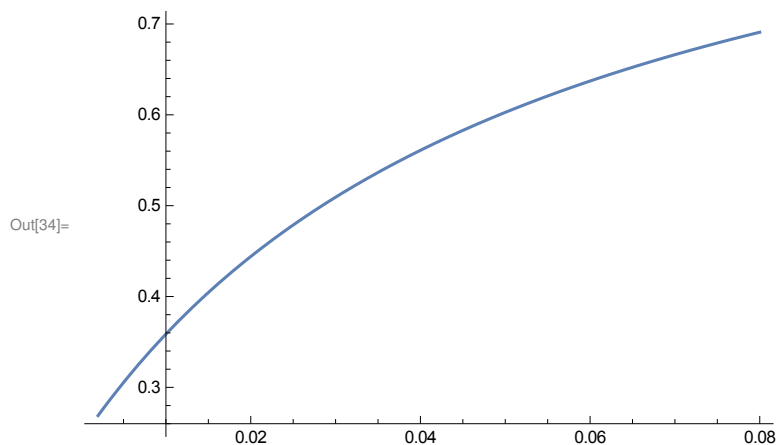
Length of the cavity (we can only measure the length of our external cavity to within a few mm at best):

In[35]:= $\texttt{Plot}\big[\texttt{RATIO}\big[\lambda,\,\texttt{a},\,\texttt{q},\,\theta1,\,\texttt{d},\,\texttt{Lx},\,\xi0\big],\,\{\texttt{Lx},\,.01,\,.08\}\big]$

Out[35]=

We assume that the laser beam would pass through the plane of the piezo actuators exactly in the middle. In this graph, we plot how much the ratio varies depending on how far off center the laser is.

In[36]:= $\texttt{Plot}\big[\texttt{RATIO}\big[\lambda,\,\texttt{a},\,\texttt{q},\,\theta1,\,\texttt{d},\,\texttt{L},\,\xi\texttt{x}\big],\,\{\xi\texttt{x},\,-.01,\,.01\}\big]$

Out[36]=
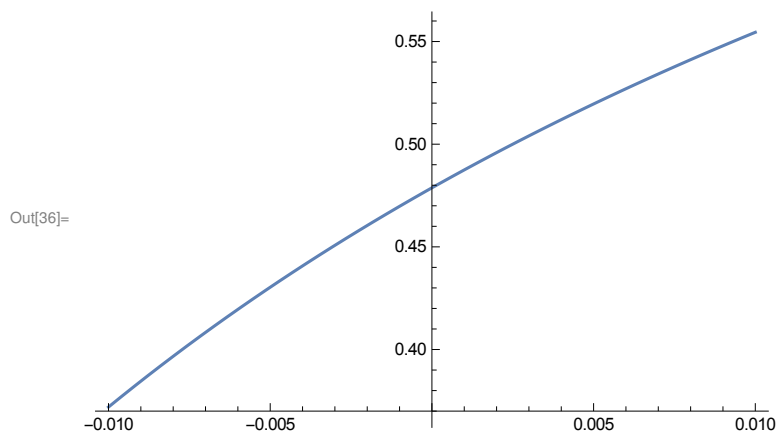
This shows the answer as a function of the actual distance between the actuators.

In[37]:= $\texttt{Plot}\big[\texttt{RATIO}\big[\lambda,\,\texttt{a},\,\texttt{qx},\,\theta1,\,\texttt{d},\,\texttt{L},\,\xi0\big],\,\{\texttt{qx},\,.04,\,.06\}\big]$

Out[37]=
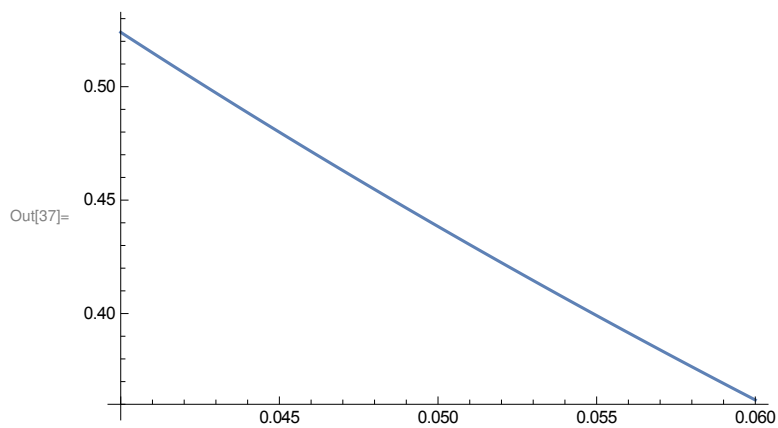
Check your answer graphically

Blue=laser beam
Green=vector of length αFUNCT that should represent the change in length of the optical cavity
Brown=parts of the piezo mount.
Red=ξ (points along grating surface to show you where things go)
Yellow=a

```
In[54]:= makeadiagram [x1_, x2_] := Graphics[{
          Arrow[{{0, 0}, {0, Py[x1, x2]}}],
          Text["P", {.001, .3 * Py[x1, x2]}], Thick, Yellow,
          Arrow[{{0, Py[x1, x2]}, {ax[x1, x2], ay[x1, x2] + Py[x1, x2]}}], Thick, Black,
          Text["a", {.5 * ax[x1, x2] + .001, .5 * ay[x1, x2] + Py[x1, x2]}], Thick, Red,
          Line[{{ax[x1, x2], ay[x1, x2] + Py[x1, x2]}, {ax[x1, x2] + ξx[x1, x2, ξFUNCT[x1, x2]],
                ay[x1, x2] + Py[x1, x2] + ξy[x1, x2, ξFUNCT[x1, x2]]}}],
          Text["ξ", {ax[x1, x2] + .5 * ξx[x1, x2, ξFUNCT[x1, x2]],
              ay[x1, x2] + Py[x1, x2] + .5 * ξy[x1, x2, ξFUNCT[x1, x2]] + .002}], Thin, Blue,
          Arrow[{{Lx[0, 0, ξ0] + .02 Cos[θL], Ly[0, 0, ξ0] + .02 Sin[θL]},
              {Lx[0, 0, ξ0] - .04 Cos[θL], Ly[0, 0, ξ0] - .04 Sin[θL]}}], Thick, Green,
          Line[{{Lx[0, 0, ξ0], Ly[0, 0, ξ0]}, {Lx[0, 0, ξ0] + αFUNCT[x1, x2] * Cos[θL],
              Ly[0, 0, ξ0] + αFUNCT[x1, x2] * Sin[θL]}}],
          Text["length=α \n direction of laser",
            {Lx[0, 0, ξ0] + .5 * αFUNCT[x1, x2] * Cos[θL] + .007,
              Ly[0, 0, ξ0] + .5 * αFUNCT[x1, x2] * Sin[θL]}],
          Thin, Brown,
          Circle[{q / 2, 0}, .001],
          Circle[{-q / 2, 0}, .001],
          Text["x₁", {-q / 2 + .002, x1 / 2}],
          Text["x₂", {q / 2 - .002, x2 / 2}],
          Arrow[{{q / 2, 0}, {q / 2, x2}}],
          Arrow[{{-q / 2, 0}, {-q / 2, x1}}], Thin, Black, Opacity[.8],
          Line[{{Lx[x1, x2, -.01], Ly[x1, x2, -.01]}, {Lx[x1, x2, .01], Ly[x1, x2, .01]}}],
          Opacity[.1],
          Polygon[{{.2 * ax[x1, x2] + q / 2, .2 * ay[x1, x2] + x2}, {q / 2, x2},
              {-q / 2, x1}, {.2 * ax[x1, x2] - q / 2, .2 * ay[x1, x2] + x1},
              {Lx[x1, x2, -.015], Ly[x1, x2, -.015]}, {ax[x1, x2], ay[x1, x2] + Py[x1, x2]},
              {ax[x1, x2], ay[x1, x2] + Py[x1, x2]}, {Lx[x1, x2, .015], Ly[x1, x2, .015]}}],
          Text["Cavity is " <> ToString[αFUNCT[x1, x2] * 10^6] <> "μm  shorter", {0, -.005}],
          Text["Δλ from  Angle is " <> ToString[-αFUNCT[x1, x2] * λ / L * 10^9] <> "nm ",
            {0, -.007}], Text["Δλ from  ΔL is " <>
              ToString[(2 d Sin[θ1 + Δθ[x1, x2]] - 2 d Sin[θ1]) * 10^9] <> "nm ", {0, -.009}]
        }]

In[63]:= myX1  = 0
        makeadiagram [myX1 , myX1 * myRATIO ]
        myX1  = 0.005
        makeadiagram [myX1 , myX1 * myRATIO ]
        myX1  = 0.01
        makeadiagram [myX1 , myX1 * myRATIO ]
        myX1  = 0.015
        makeadiagram [myX1 , myX1 * myRATIO ]
```
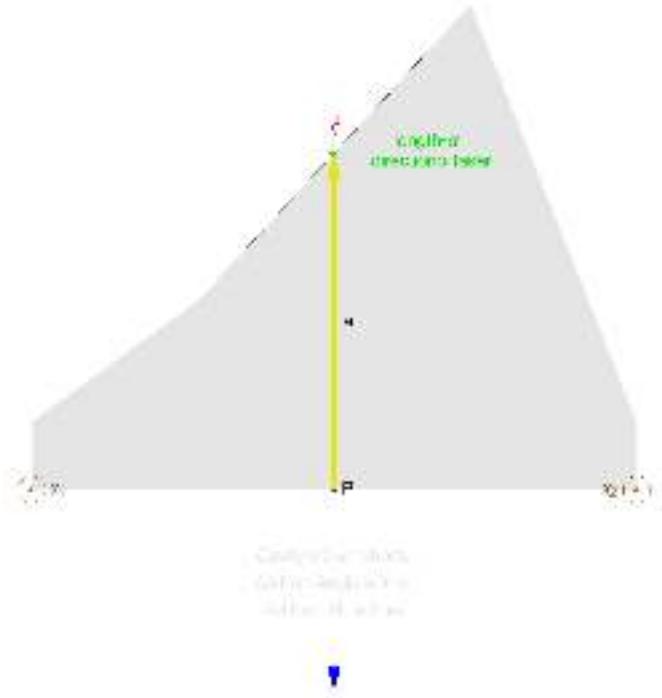
Out[63]= 0

Out[64]=

Out[65]= 0.005

Out[66]=

Out[67]= 0.01

Out[68]=

Out[69]= 0.015

Out[70]=
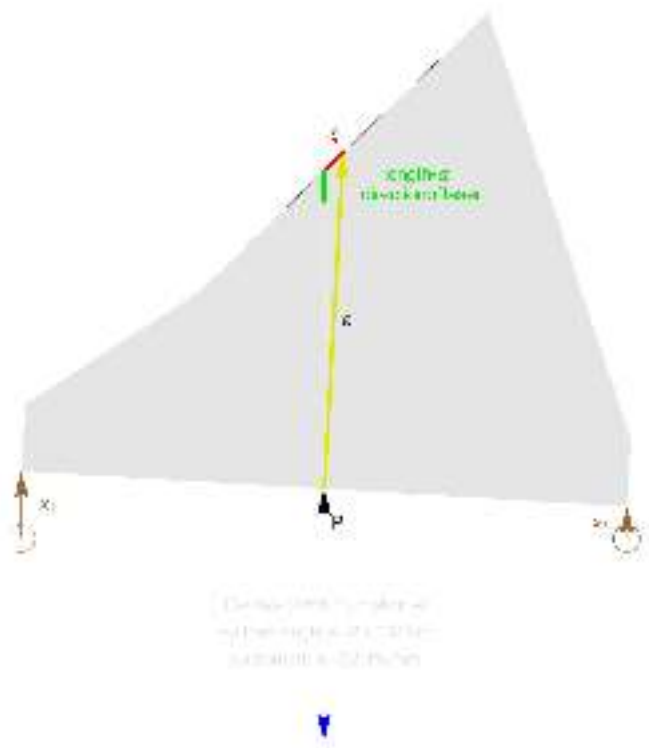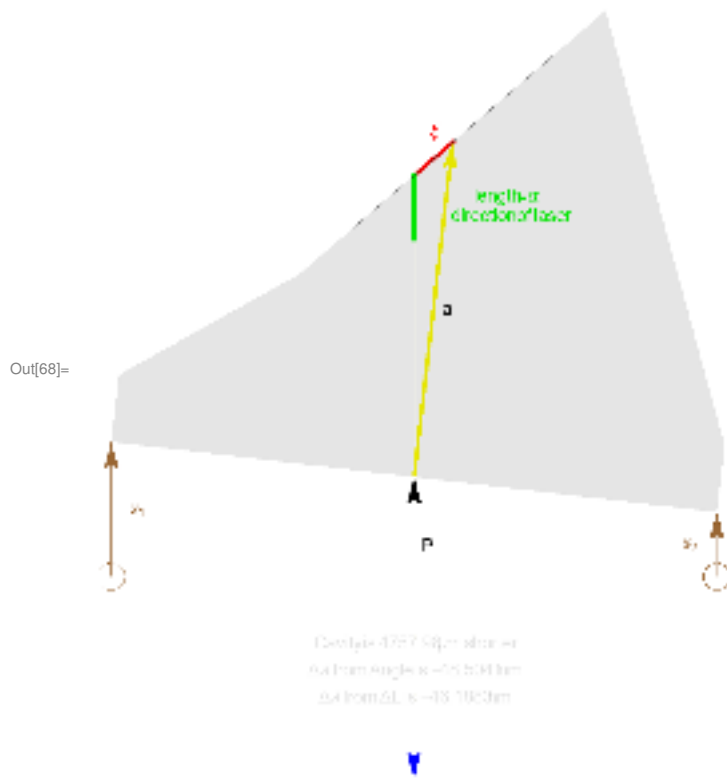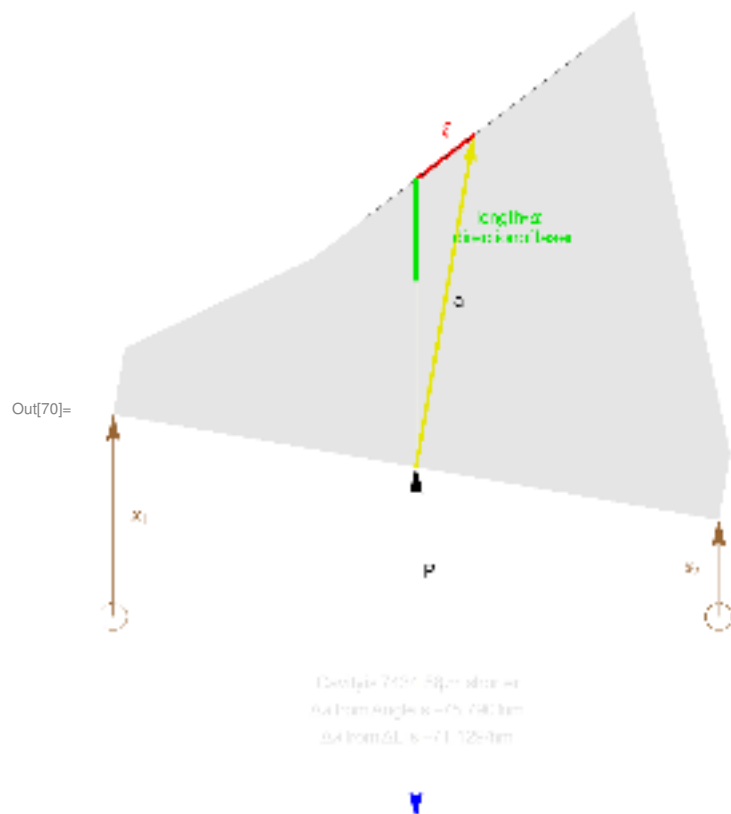
Appendix C

Spectrum Analyzer

In this Appendix, we discuss the Fabry-Perot spectrum analyzer that we built to analyze this system.

C.1 Spectrum analyzer design

One of the mirrors is mounted on a Thorlabs kinematic piezo mount and attached to a piezo driver designed specifically for spectrum analyzers.

The cavity is designed to be nearly semiconfocal.This is because a semiconfocal configuration is one of several in which many modes are degenerate, such that liht coupling to different transverse modes come into resonnance at the same frequency. This makes it possible to get very sharp, clear features without having to carefully couple to one specific transverse mode of the cavity.

C.2   Free spectral range basics

The Free Spectral Range (FSR) of the cavity is defined as the difference in frequency between adjacent resonant longitudinal modes of the cavity. It always works out to be $c/2L$. It is easy to condsider the example of a one-dimensional cavity with just one transverse mode. If we suppose that we have some wavelength λ that is resonant with our cavity, then the resonant condition would be that

$$m\lambda = 2L, \tag{C.1}$$

where m is an integer and L is the cavity length (center to center distance between the surfaces of the cavity mirrors). In other words, we require that for a mode to be resonant with our cavity, the total optical path length of a trip around the cavity (in this case, twice the cavity length) must be divisible by the wavelength of the light.

We can find other wavelengths of light that satisfy the resonance condition. So, for example, we might be able to find some wavelength λ' that satisifes

$$(m+1)\lambda' = 2L. \tag{C.2}$$

The free spectral range would just be the difference in frequencies corresponding to λ and λ'. Using $\lambda = c/f$, we see that

$$m\lambda = 2L \rightarrow \frac{mc}{f} = 2L, \tag{C.3}$$

which we can solve for f to find

$$f - f' = \frac{(m+1)c}{2L} - \frac{mc}{2L} \tag{C.4}$$

$$= \frac{c}{2L}, \tag{C.5}$$

where f' and f' are the frequencies associated with λ and λ' respectively.
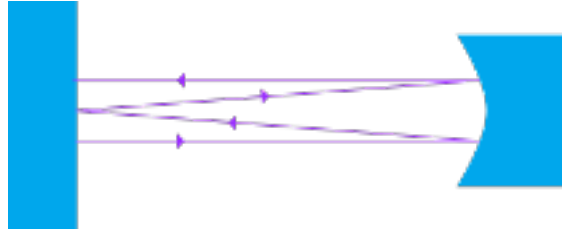
Figure C.1 Illustration of the optical path that makes a complete trip around the semiconfocal cavity. Note that the ray traverses the entire length of the path four times before doubling back on itself. It traverses the path 8 times before ending up in the same place again. This diagram similar to one found on page 277 of Ref. [55]. Here, we assume that the ray travels nearly parallel to the central axis of the cavity so that the length of each leg is well-approximated by the length of the cavity, L.

C.3 Free spectral range for real cavities

In general, there will be more than one transverse mode. The free spectral range remains $c/2L$. However, between any two peaks corresponding to one transverse mode, there will be other resonant peaks corresponding to other transverse modes. Thus, there will be resonances of our cavity spaced closer than the free spectral range. One could, in principle, couple to just a single transverse mode by carefully coupling the beam to the cavity.

However, in our system this is not necessary. We use a semiconfocal (hemiconfocal), which has the convenient property that the various transverse modes line up in such a way that they fall into four distinct, evenly-spaced groups. Therefore, if we couple to many transverse modes of the cavity, we expect that our effective free spectral range will be $c/8L$.

C.4 Derivation of free spectral range for semiconfocal cavities

This can be illustrated with a simple ray-tracing argument. In order for the cavity to be resonant with our light, the full optical path of the light must be an integer number of

wavelengths. The resonance condition is

$$n\lambda = d, \tag{C.6}$$

where n is an integer, λ is the wavelength and d is the length of the optical path in the cavity. For a semiconfocal cavity, we can convince ourselves visually (see Fig. C.1) that a ray parallel to the optical axis would traverse the entire length of the cavity 8 times before finally getting back to its starting point. Thus, we expect that $d \approx 8L$. We therefore expect that modes in the cavity will have resonant frequencies spaced by $c/8L$.

C.5 Using the paraxial wave equation

A more rigorous treatment of this can be done by solving the paraxial wave equation. This model will also allow us to model the exact behavior of our real life cavity (note that in the real cavity, we look at just a handful of wavelengths but we scan the cavity length).

C.5.1 Review of paraxial wave equation

We first examine the equation describing the electric field for different modes of the cavity. This can be derived directly from Maxwell's equations using the paraxial approximation (see, e.g., Refs. [55] and [61] for a complete discussion of this). The argument in brief is basically this:

- Assume that the three-dimensional electric field can be represented by a scalar quantity $E(\mathbf{r}, t)$

- Recall Maxwell's equations with no nearby charges or currents give rise to the wave equation $\nabla^2 E(\mathbf{r}, t) - \frac{1}{c^2} \frac{\partial^2}{\partial t^2} E(\mathbf{r}, \mathbf{t}) = 0$

- Assume solution takes the form $E(\mathbf{r}, t) = \mathcal{E}_0(\mathbf{r}) \exp(i(kz - \omega t))$ and plug this into the wave equation above.

- Make the paraxial approximation: Assume that $\lambda \left| \frac{\partial \mathcal{E}}{\partial z} \right| \ll |\mathcal{E}_0|$ and $\lambda \left| \frac{\partial^2 \mathcal{E}_0}{\partial z^2} \right| \ll \left| \frac{\partial \mathcal{E}_0}{\partial z} \right|$. In other words, we assume that the wiggling is mostly happening along the z direction.

This leads to the paraxial wave equation:

$$\left(\frac{\partial^2}{\partial x^2} + \frac{\partial^2}{\partial y^2} + 2ik \frac{\partial}{\partial z} \right) \mathcal{E}_0(\mathbf{r}) = 0. \tag{C.7}$$

The solutions to Eq. C.7 can be shown to be of the form:

$$\mathcal{E}_{mn}(x, y, z) = \frac{A w_o}{w(z)} H_m \left[\sqrt{2} \frac{x}{w(z)} \right] H_n \left[\sqrt{2} \frac{x}{w(z)} \right] \tag{C.8}$$

$$\times \exp(i(kz - (m + n + 1) \tan^{-1}(z/z_0)) \tag{C.9}$$

$$\times \exp(ik(x^2 + y^2)/2R(z)) \exp(-(x^2 + y^2)/w^2(z)). \tag{C.10}$$

Here, $\mathcal{E}$ is the magnitude of the electric field. H_m and H_n are the (physicists') Hermite polynomials of degree m and n[1]. $R(z), z_0, w_z$ and w_0 are defined in the same way that they are for a Gaussian mode:

$$w(z) = w_0 \sqrt{1 + \frac{z^2}{z_0^2}} \tag{C.11}$$

$$R(z) = z + \frac{z_0^2}{z} \tag{C.12}$$

$$z_0 = \frac{\pi w_0^2}{\lambda}. \tag{C.13}$$

C.5.2   Frequencies of resonant modes

Now, the propagation of the solution to the paraxial wave equation from C.8 can be calculated using Eq. 5.14. The resonant condition is that after propagating across the cavity an arbitrary

---

[1]If we ever were to need a real solution to the equation, we could find one by simply taking: $\mathcal{E} + \mathcal{E}*$.

number of times, a beam must be the same [55]. Alternatively, we may demand simply that $R(z)$ (which we interpret as the radius of the wavefronts) at the location of each of the mirrors match the radius of the mirror. This condition on R is sufficient to guarantee that the cavity mode the light is traversing is stable. In order to have a resonant mode (as opposed to a mode that is merely stable), the light must also accumulate a phase change that is some integer multiple of 2π after traversing the cavity a finite number of times.

Following this reasoning, Ref. [55] gives the following equation for the resonant frequencies of the longitudinal modes of our cavity:

$$\nu_{qmn} = \frac{c}{2L}\left[q + \frac{1}{\pi}(m+n+1)\cos^{-1}(\text{sgn}(g_1)\sqrt{g_1 g_2})\right]. \tag{C.14}$$

Here, L is the length of the cavity; q is a nonnegative integer; m and n are integers representing the order of the Hermite polynomials in the solution in the x and y directions. g_i is defined for each mirror and is given by $1 - L/R_i$. The term involving g_1 and g_2 will depend strictly on our cavity geometry[2].

From Eq. C.14, we see that the semiconfocal cavity has the special property that many of the resonances align. One of our mirrors is flat, so $g_1 = 1 - L/\infty = 1$, while the other's focal length, f_2 is equal to the length of the cavity. Recalling that the normal relationship between radius of curvature and focal length is $R_2 = 2f_2$, we see that $g_2 = 1 - L/R_2 = 1 - L/(2f_2) = 1 - L/(2L) = 1/2$. Thus,

$$\cos^{-1}(\text{sgn}(g_1)\sqrt{g_1 g_2}) = \frac{\pi}{4}. \tag{C.15}$$

Substituting this into Eq. C.14, we see that

$$\nu_{qmn} = \frac{c}{2L}\left[q + \frac{1}{4}(m+n+1)\right]. \tag{C.16}$$

---

[2]It may seem strange that Eq. C.14 depends on the sign of g_1 and not g_2. However, this equation is valid only for stable cavities and the condition for a stable cavity is that $0 \le g_1 g_2 \le 1$. Thus, we can assume that g_1 and g_2 have the same sign.

Since m,n and q are all integers, we see that the resonant modes will be integer multiples of $c/(8L)$. Thus, Eq. C.16 demonstrates one of the nicest features about semi-confocal cavities, which is that different transverse modes of the electric and magnetic have the same resonant frequency. In practice, this means that rather than having to couple carefully to the TEM_{00} mode, we can allow the light to couple to any transverse mode of the cavity. If we assume that we are coupled to many cavity modes (which we almost always will be, unless we were to purposefully try to avoid coupling to some subset of the resonant modes of the cavity), we can safely assume that adjacent resonant frequency peaks are separated by $c/8L$. We have thus derived Free Spectral Range of the cavity.

C.6 Modelling the actual spectrum analyzer

The spectrum analyzer works by allowing us to change the cavity length and thereby go into and out of resonance with different wavelengths of light. The above discussion is valid for calculating what frequencies will couple to a fixedcavity, but we would like to verify that coupling a fixed frequency into a cavity of variable length will give us essentially the same thing.

The piezoelectric mount (Thorlabs KC1-PZ) is rated to accept a maximum voltage of 150 V and provide a maximum of $\pm 4\mu$m of linear travel. Thus, since our sweep voltage is only about 75 V, we expect that our cavity should be sweeping 2μm. If the wavelength of the light is 408 nm, we expect that for each 2μm of displacement, we should see about $8 * 2\mu$m$/408nm \approx 40$ resonant peaks. This is a good order of magnitude estimate for the most peaks we can see. Therefore, we can say that the change in cavity length, $\Delta L < 2\mu$m.

Now, if we take Eq. C.14 and make the following substitutions:

$$g_1 \to 1 \text{ (since } R_1 = \infty) \tag{C.17}$$

$$g_2 \to 1 - L/(2L) \tag{C.18}$$

$$L \to L(1 - \epsilon), \tag{C.19}$$

we get

$$\nu_{qmn} = \frac{c}{2L(1+\epsilon)}\left(q + \frac{m+n+1}{\pi}\arccos(\sqrt{1 - L(1-\epsilon)/(2L)})\right). \tag{C.20}$$

Note that we have used $R_2 = 2L$ and not $R_2 = 2L(1+\epsilon)$ since the radius of the mirror does not change as we sweep the cavity.

We now make a Taylor expansion of Eq. C.20 using Mathematica, we get

$$
\begin{aligned}
\nu_{qmn} = \frac{c}{8L}\Bigg(& (4q + m + n + 1) + \\
& \left(-4q - m - n - 1 + \frac{2}{\pi}(1 + m + n)\right)\epsilon + \\
& \left(5q + m + n + 1 + \frac{2}{\pi}(1 + m + n))\right)\epsilon^2 + \\
& \left(-4q - m - n - 1 + \frac{7}{3\pi}(1 + m + n)\right)\epsilon^3 + \\
& \left(4q + m + n + 1 - \frac{7}{3\pi}(1 + m + n)\right)\epsilon^4\Bigg).
\end{aligned}
$$

The coefficient for the first order expansion in terms of ϵ contains integers m,n and q as we expect. However, it might seem unnerving at first that it also contains coefficents like $2/\pi$ that are of order unity! The reason this is ok is that $q \gg m, n$. We know this is the case for two reasons: First, the Laguerre Gaussian modes are derived using the paraxial wave approximation. The paraxial wave equation assumes solutions of the form

$$\vec{E}(\vec{r}, t) \approx \mathcal{E}(\vec{r})\exp[i(kz - \omega t)], \tag{C.21}$$

and it relies on the fact that

$$\left|2k\frac{\partial\mathcal{E}(\vec{r})}{\partial z}\right| \gg \left|\frac{\partial^2\mathcal{E}(\vec{r})}{\partial z^2}\right|. \tag{C.22}$$

Since the derivatives of $E(\vec{r})$ depend on mth and nth order Hermite polynomials, we see that our equations only hold up when m and n are reasonably small. Second, we can use qualitative observations of the cavity mode. The cavity length is 20cm, while the cavity mirrors are about 1 cm across and the laser modes in the cavity can be seen to be less than 5 mm in diameter. One may imagine intuitively that the number of nodes along a long dimension (represented roughly by q) is going to be large compared to the number of nodes created by light at the same frequency along a much smaller distance. Therefore, $q \gg m, n$.

If we assume the argument in the radical $(1 - L(1 + \epsilon)/(2L) \approx 1/2$ for all values of ϵ, then we get this expansion:

$$\nu_{qmn} = \frac{c}{8L}, \tag{C.23}$$

which is exactly what we had expected based on our ray-tracing argument. Plugging in values from our cavity $(L = 20cm)$, we see that the Free Spectral Range of the cavity is $\sim$187 MHz.

Appendix D

Adjusting Light Levels with Imperfect Waveplates

The light level from the master laser is constrained by our requirement that the Master laser operate single mode. However, we require control of the light levels further downstream in order to have the right light levels to avoid damage to the Acousto-Optic Modulator (AOM) and to have the right amount of light to injection lock the other lasers.

A typical way to accomplish this is to install a half wave plate followed by a polarizing beam cube. In this way, one can take the linearly polarized incoming light and rotate its polarization to any angle. One can thus exert complete control of the amount of light coming out of the polarizing beam cube.

We had initially intended to use this scheme. However, there was a mistake in placing the order. Instead of 0 order waveplates, we had received multi-order waveplates, whose performance rapidly degrades for wavelengths far from the specified wavelength.

We could have easily ordered a 0 order waveplate to replace them. However, we found a way to use the exising waveplates.

D.1   A review of the principles of operation of a wave-

plate

A waveplate rotates polarization by changing the relative phase of the oscillating components of the incoming polarized light. A waveplate has a fast axis and a slow axis. A half-wave plate is designed so that, at the specified wavelength, the component of polarization along the slow axis acquires a phase shift of $(2m + 1) * \pi$ relative to the fast axis. Here m is an integer.

Recall that the phase acquired by light as it passes through a medium of index of refraction n is given by

$$\Delta\phi = \frac{2\pi n x}{\lambda} \tag{D.1}$$

Given indices of refraction of n_1 and n_2 for our two axes, we find that the difference in phase acquired by the components of the light's polarization will be

$$\Delta\phi = \frac{2\pi n_1 x}{\lambda} - \frac{2\pi n_2 x}{\lambda}. \tag{D.2}$$

and we find that, in order to achieve the correct phase shift, the acceptable thicknesses of our half wave plate must satisfy

$$\Delta\phi = (2m + 1)\pi \tag{D.3}$$

where m is the order of the waveplate.

Combining D.3 and D.2 we find that the thickness of a waveplate x is given by

$$x = \frac{(2m + 1)\lambda}{2(n_1 - n_2)}. \tag{D.4}$$

We now examine what will happen if we put a different wavelength than specified into the waveplate. Thus, we assume that x,n_1,n_2 and m give the appropriate π phase shift for the wavelength at which the waveplate is designed to work (λ_s). Now, we try light of a different wavelength, λ'. Assuming that the indices of refraction stay roughly the same for both λ_s and λ', we see that

$$\Delta\phi = \frac{2\pi(n_1 - n_2)x}{\lambda'} \tag{D.5}$$

Then, taking $x \to ((2m+1)\lambda_s)/(2(n_1 - n_2))$ from Eq. D.4, we get

$$\Delta\phi = \frac{2\pi(n_1 - n_2)(2m+1)\lambda_s}{2(n_1 - n_2)\lambda'} \tag{D.6}$$

$$\Delta\phi = \frac{\pi(2m+1)\lambda_s}{\lambda'} \tag{D.7}$$

Eq. D.7 illustrates that the performance of a multi-order waveplate (with high value for m) will degrade more rapidly at different wavelengths than a low-order waveplate.

D.2 Motivation for use of two waveplates

In our lab, we had a half wave plate, but it was a multi-order plate designed for 405 nm. Thorlabs specifies that the waveplates we had would provide the correct retardance at 405 nm, however they also specify that at 407.71 nm the net retardance is 0.3655746 waves, or $\Delta\phi = (m_2 + .3656)(2\pi)$. Based on Eq. D.7, we see that this is consistent with and $m = 55$ order waveplate.

The problem here is that, in order to completely control the amount of light getting to the AOM, we want to change the polarization from fully vertical to fully horizontal. Given that the incoming light is vertically polarized, this retardance does not allow us to get fully horizontally polarized light, thereby imposing a minimum amount of light on us.

However, we found that we can compensate for this by simply using two waveplates in series. Using numerical methods, we found that the user can fix the orientation of one of the waveplates in such a way that by rotating the other waveplate over some reasonable distance (i.e. over a range of angles large enough that a user could adjust the waveplate by hand), the outgoing light can be smoothly adjusted between being completely vertical or completely horizontal.

Now, the polarization of the light when it is neither completely vertically nor completely horizontally polarized will not necessarily be linearly polarized. There will, in general, be some arbitrary phase shift between the components of polarization. However, this does not matter for our purpose since the goal was simply to control the amount of power exiting from each of two sides of a polarizing beam cube.

D.3   Jones matrices

This can be demonstrated using the Jones matrix formalism. The polarization of the incoming light can be represented by the following Jones vector:

$$\begin{pmatrix} 0 \\ 1 \end{pmatrix} \tag{D.8}$$

The Jones matrix corresponding to our waveplate is easily derived. Given that:

$$\begin{pmatrix} \cos\theta & -\sin\theta \\ \sin\theta & \cos\theta \end{pmatrix} \begin{pmatrix} \xi & 0 \\ 0 & 1 \end{pmatrix} \begin{pmatrix} \cos\theta & \sin\theta \\ -\sin\theta & \cos\theta \end{pmatrix}$$
$$= \begin{pmatrix} \cos^2\theta + \xi\sin^2\theta & \cos\theta\sin\theta - \xi\cos\theta\sin\theta \\ \cos\theta\sin\theta - \xi\cos\theta\sin\theta & \xi\cos^2\theta + \sin^2\theta \end{pmatrix} \tag{D.9}$$

where θ is the angle between the fast axis and the x axis.

We let $\xi \approx e^{.366(2\pi)}$ as specified by the waveplate. Then, to represent two of them mounted at angles θ_1 and θ_2 respectively, we need merely multiply two matrices like the one in Eq. D.9. Writing out the result is straightforward, but we left it to a computer algebra system.

By numerical experimentation, we found that there was a set of angles where we could mount our two waveplates that would result in a polarization for the outgoing light that is orthogonal to the polarization of the incoming light.

D.4 Alignment procedure

By physical and numerical experimentation, we found that you can achieve these angles by subsequently adjusting each of the two waveplates in turn. Keeping 100% of the light vertically polarized is easy and can be achieved for any fixed value of θ_2 since θ_1 can simply be adjusted so that the fast axis of the first waveplate aligns with the slow axis of the second. In this way, the total phase shift experienced by all the components is equal.

Thus, to correctly place the second waveplate at the angle θ_2, we adjust both angles until the outgoing light is entirely horizontally polarized (as measured by the output of the polarizing beam cube). I found that mounting the waveplates at the approximate angles I calculated followed by alternately adjusting each waveplate to minimize the amount of light transmitted achieved the desired result.

D.5 Results for other combinations of waveplates

We performed additional numerical calculations and found a couple things:

This only works for certain retardances. If one of the waveplates has a retardance of 0.5 waves, then (obviously) this would work. If the two waveplates have the same retardance and
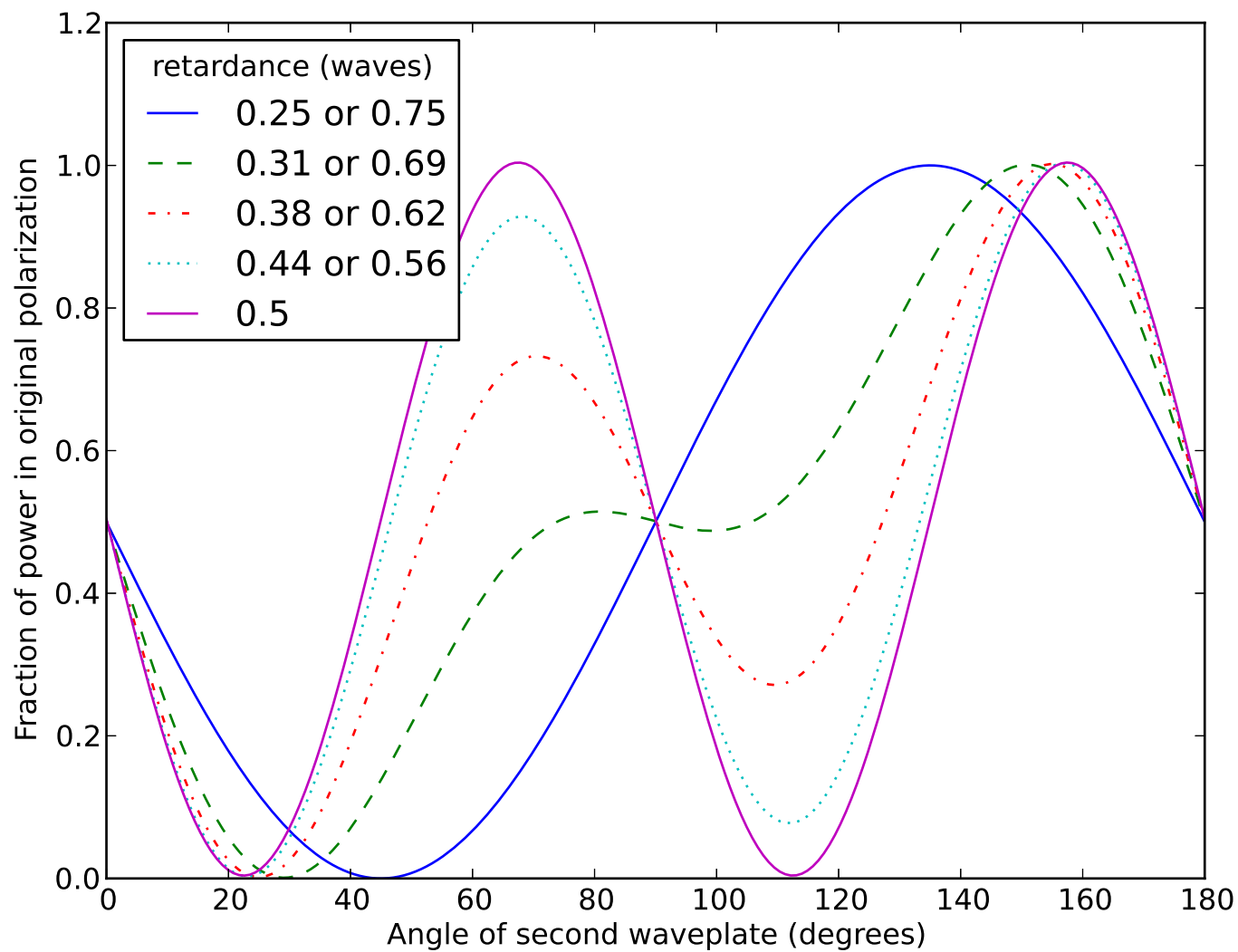
Figure D.1 A plot the magnitude of the fraction of the power at the original po-
larization as a function of the angle of the second waveplate for various retardances.

that retardance is between 0.25 and 0.75 waves, this will also allow the user to put anywhere from 0% to 100% of the power into either polarization. Figure D.2 illustrates the maximum power that can be extinguished as a function of the retardance of the two waveplates.

D.6 Attempt at building intuition

Armed with the important clue that the we can use this trick only if the waveplates have the same retardance, we can make an attempt at describing the phenomenon only in terms of symmetry arguments.

We first consider vertically polarized light travelling into a waveplate. If we align the fast axis of the waveplate to the vertical direction, our vertically polarized light will emerge with a vertical polarization.

However, if we rotate the fast axis to one side by some angle θ, we get elliptically polarized light. Notice tht if we rotate the fast axis to the other side (i.e. by some angle $-\theta$) we also get elliptically polarized light. However, this light is elliptically polarized with the same ellipticity, but with the opposite handedness.

Now, we consider the second waveplate. We would like to consider what it would take to get horizontally polarized light coming out of the second waveplate. We can do this by noting that our system has time reversal symmetry. The time reversed outgoing horizontally polarized light turns out to be incoming horizontally polarized light. Similarly as before, the second waveplate can achieve elliptically polarized light of various handednesses.

Now, we simply argue that, by symmetry, we can place the two waveplates at some set of angles such that the elliptically polarized light coming out of the first waveplate corresponds to the time reversed elliptically polarized light coming through the second waveplate. It turns out that this leads to a nice symmetry in the result where, in order to get linearly polarized light out of the whole apparatus, the angle between the incoming polarization and
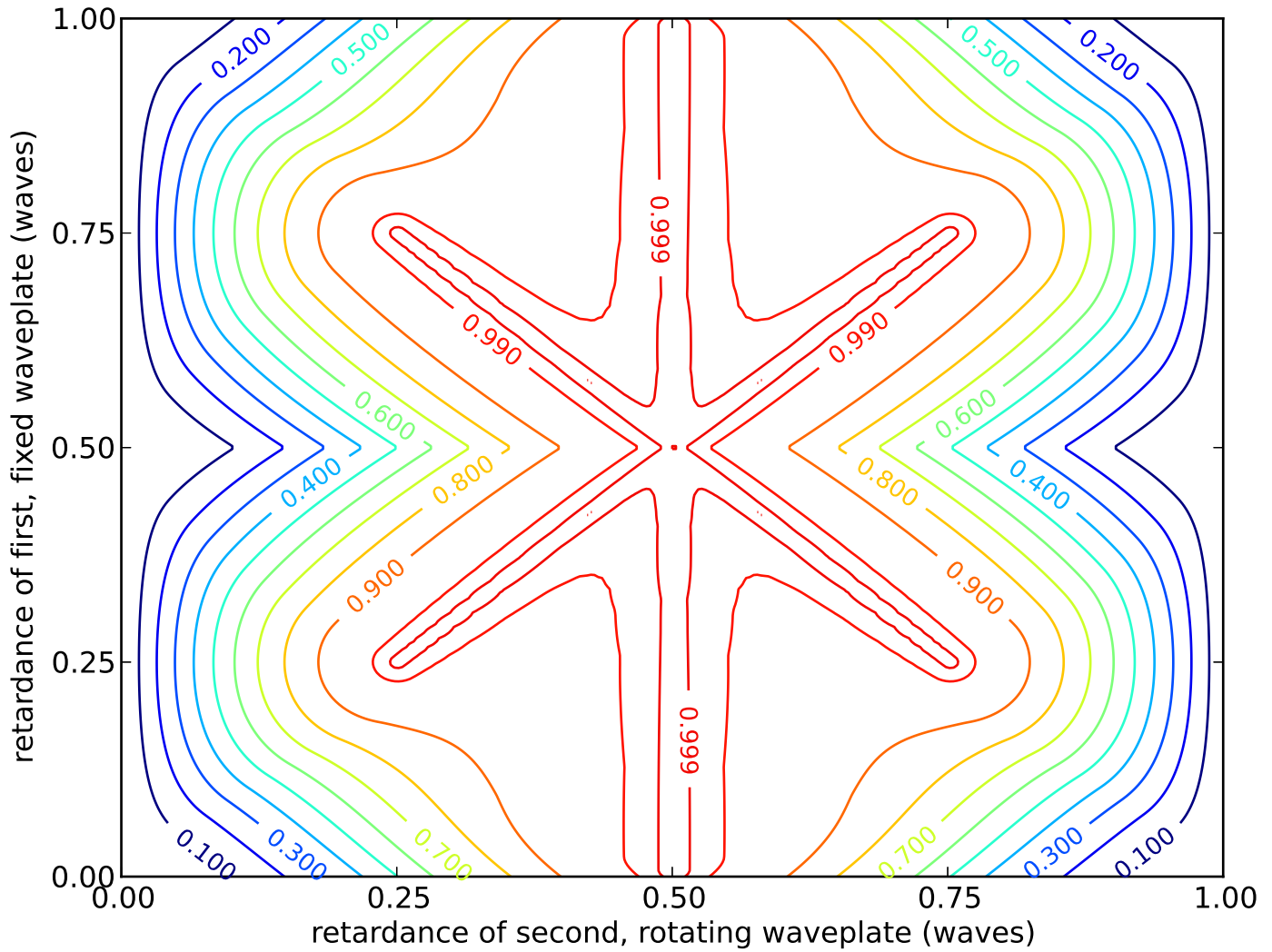
Figure D.2 The maximum power that one can extinguish through the polarizing beam cube given the retardance of the two waveplates. As one expects, if either waveplate has a retardance of 0.5 waves, one can get the full range of possible outgoing polarizations. However, this is only possible for certain combinations of waveplate retardances

the fast axis of the first waveplate will be equal in magnitude but opposite in sign to the angle between the outgoing polarization and the fast axis of the second waveplate.

Appendix E

Miscellaneous Bits of Code

E.1 Calculation of Dipole Moment Operator

This calculation is relatively straightforward. However, when dealing with a lot of constants, it is easy to use an online service to keep things straight. For this calculation, I prefer to enter "sqrt(3*hbar*c$\hat{3}$/(4*(2*pi*c/407.771 nm)$\hat{3}$)*4*pi*epsilon_0*4*1.41e8*1/s)" as a query into Wolfram Alpha. The result (as of 2015-11-25) can be found here. The result turns out to be 4.344 Bohr dipole moments.

E.2 Hyperfine splitting

This is a Jupyter notebook containing Python 2 codde to calculate the hyperfine splitting.

Our goal in this notebook is to calculate the hyperfine splitting for $^{87}\mathrm{Sr}^+$. This will be given by

$$E_{\mathrm{hfs}} = \frac{1}{2}AC + BC(C+1),$$

where C is given by

$$C = F(F+1) - J(J+1) - I(I+1).$$

First, we will store the values of A and B given by Safronova's paper. Both of these values are in MHz

```
In [1]: AP=-35.3
        BP=88.68
```

```
In [2]: def hyperfine_split(F,J=3.00/2,I=9.00/2):
            C=F*(F+1)-J*(J+1)-I*(I+1)
            #print "C=",C,"I=",I,"F=",F,"A=",AP,"B=",BP
            return (1.0/2)*AP*C+BP*C*(C+1)
```

```
In [3]: AP=-35.3
        BP=88.68

        print "F=3 gives", hyperfine_split(3),"MHz"
        print "F=4 gives", hyperfine_split(4),"MHz"
        print "F=5 gives", hyperfine_split(5),"MHz"
        print "F=6 gives", hyperfine_split(6),"MHz"

        F=3 gives 22971.135 MHz
        F=4 gives 5803.375 MHz
        F=5 gives 306.075 MHz
        F=6 gives 17120.835 MHz
```

Now, we look at the S state. $A = 1000$ MHz, $B = 0$ MHz while $J = \frac{1}{2}$ and I is still $\frac{9}{2}$.

```
In [4]: AP=1000
        BP=0

        print "F=4 gives", hyperfine_split(4,J=1.0/2)
        print "F=5 gives", hyperfine_split(5,J=1.0/2)

        F=4 gives -2750.0
        F=5 gives 2250.0
```

The difference between these is clearly 5 GHz.

```
In [5]: #A version table.
        #This notebook does not use anything else from the qutip package.
        from qutip.ipynbtools import version_table
        version_table()
```

/home/jlarchibald/anaconda/lib/python2.7/site-packages/IPython/parallel.py:13:
ShimWarning: The `IPython.parallel` package has been deprecated. You should imp
ort from ipyparallel instead.
    "You should import from ipyparallel instead.", ShimWarning)

Out[5]:

Software	Version
Cython	0.22.1
SciPy	0.15.1
QuTiP	3.1.0
Python	2.7.10 |Anaconda 2.3.0 (64-bit)| (default, Oct 19 2015, 18:04:42) [GCC 4.4.7 20120313 (Red Hat 4.4.7-1)]
IPython	4.0.0
OS	posix [linux2]
Numpy	1.9.2
matplotlib	1.4.3
Mon Nov 23 22:59:56 2015 CST	

E.3   Clebsch-Gordan coefficient calculation

When using the Wigner-Eckhart theorem in Chapter 3, I used this code to calculate the coefficients. I was not sure which states could be viably identified as $|i\rangle$, $|e\rangle$ and $|g\rangle$, so I somewhat used brute force to see which Clebsch-Gordan coefficients turned out to be nonzero.

We want to calculate the coefficients for the following values:

$$\langle {}^{2}P_{3/2}F' = [3,4,5,6], m_f = \text{All}||r|^2 S_{1/2}F = [4,5], m_f = \text{All}\rangle$$

for all values of q.

Thus we need these C-G coefficients:

$$\langle F, m_f, 1, q|F', m'_f\rangle$$

for

$$q = -1, 0, 1$$
$$F = 4, 5$$
$$F' = 3, 4, 5, 6$$

```
In [1]: from sympy.physics.quantum.cg import CG
        from sympy import S
        import sympy
```

First, we try looking at all the non-zero Clebsch-Gordan coefficients:

```
In [2]: Fs=[S(4),S(5)]
        Fps=[S(3),S(4),S(5),S(6)]
        qs=[S(-1),S(0),S(1)]
        for q in qs:
            for F in Fs:
                for Fp in Fps:
                    for mf in range(-F,F+1):
                        for mfp in range(-Fp,Fp+1):
                            if(CG(F,mf,S(1),q,Fp,mfp).doit()<>0):
                                print 'F=',F,',Fp=',Fp,',mf=',mf,',mfp=',mfp,',q=',q,'
        ,    CG COEFFICIENT =',CG(F,mf,S(1),q,Fp,mfp).doit()
```

```
F= 4 ,Fp= 3 ,mf= -2 ,mfp= -3 ,q= -1 ,    CG COEFFICIENT = 1/6
F= 4 ,Fp= 3 ,mf= -1 ,mfp= -2 ,q= -1 ,    CG COEFFICIENT = sqrt(3)/6
F= 4 ,Fp= 3 ,mf= 0 ,mfp= -1 ,q= -1 ,    CG COEFFICIENT = sqrt(6)/6
F= 4 ,Fp= 3 ,mf= 1 ,mfp= 0 ,q= -1 ,    CG COEFFICIENT = sqrt(10)/6
F= 4 ,Fp= 3 ,mf= 2 ,mfp= 1 ,q= -1 ,    CG COEFFICIENT = sqrt(15)/6
F= 4 ,Fp= 3 ,mf= 3 ,mfp= 2 ,q= -1 ,    CG COEFFICIENT = sqrt(21)/6
F= 4 ,Fp= 3 ,mf= 4 ,mfp= 3 ,q= -1 ,    CG COEFFICIENT = sqrt(7)/3
F= 4 ,Fp= 4 ,mf= -3 ,mfp= -4 ,q= -1 ,    CG COEFFICIENT = sqrt(5)/5
F= 4 ,Fp= 4 ,mf= -2 ,mfp= -3 ,q= -1 ,    CG COEFFICIENT = sqrt(35)/10
F= 4 ,Fp= 4 ,mf= -1 ,mfp= -2 ,q= -1 ,    CG COEFFICIENT = 3*sqrt(5)/10
F= 4 ,Fp= 4 ,mf= 0 ,mfp= -1 ,q= -1 ,    CG COEFFICIENT = sqrt(2)/2
F= 4 ,Fp= 4 ,mf= 1 ,mfp= 0 ,q= -1 ,    CG COEFFICIENT = sqrt(2)/2
F= 4 ,Fp= 4 ,mf= 2 ,mfp= 1 ,q= -1 ,    CG COEFFICIENT = 3*sqrt(5)/10
F= 4 ,Fp= 4 ,mf= 3 ,mfp= 2 ,q= -1 ,    CG COEFFICIENT = sqrt(35)/10
F= 4 ,Fp= 4 ,mf= 4 ,mfp= 3 ,q= -1 ,    CG COEFFICIENT = sqrt(5)/5
F= 4 ,Fp= 5 ,mf= -4 ,mfp= -5 ,q= -1 ,    CG COEFFICIENT = 1
F= 4 ,Fp= 5 ,mf= -3 ,mfp= -4 ,q= -1 ,    CG COEFFICIENT = 2*sqrt(5)/5
F= 4 ,Fp= 5 ,mf= -2 ,mfp= -3 ,q= -1 ,    CG COEFFICIENT = 2*sqrt(35)/15
F= 4 ,Fp= 5 ,mf= -1 ,mfp= -2 ,q= -1 ,    CG COEFFICIENT = sqrt(105)/15
F= 4 ,Fp= 5 ,mf= 0 ,mfp= -1 ,q= -1 ,    CG COEFFICIENT = sqrt(3)/3
F= 4 ,Fp= 5 ,mf= 1 ,mfp= 0 ,q= -1 ,    CG COEFFICIENT = sqrt(2)/3
F= 4 ,Fp= 5 ,mf= 2 ,mfp= 1 ,q= -1 ,    CG COEFFICIENT = sqrt(30)/15
F= 4 ,Fp= 5 ,mf= 3 ,mfp= 2 ,q= -1 ,    CG COEFFICIENT = sqrt(15)/15
F= 4 ,Fp= 5 ,mf= 4 ,mfp= 3 ,q= -1 ,    CG COEFFICIENT = sqrt(5)/15
F= 5 ,Fp= 4 ,mf= -3 ,mfp= -4 ,q= -1 ,    CG COEFFICIENT = sqrt(55)/55
F= 5 ,Fp= 4 ,mf= -2 ,mfp= -3 ,q= -1 ,    CG COEFFICIENT = sqrt(165)/55
F= 5 ,Fp= 4 ,mf= -1 ,mfp= -2 ,q= -1 ,    CG COEFFICIENT = sqrt(330)/55
F= 5 ,Fp= 4 ,mf= 0 ,mfp= -1 ,q= -1 ,    CG COEFFICIENT = sqrt(22)/11
F= 5 ,Fp= 4 ,mf= 1 ,mfp= 0 ,q= -1 ,    CG COEFFICIENT = sqrt(33)/11
F= 5 ,Fp= 4 ,mf= 2 ,mfp= 1 ,q= -1 ,    CG COEFFICIENT = sqrt(1155)/55
F= 5 ,Fp= 4 ,mf= 3 ,mfp= 2 ,q= -1 ,    CG COEFFICIENT = 2*sqrt(385)/55
F= 5 ,Fp= 4 ,mf= 4 ,mfp= 3 ,q= -1 ,    CG COEFFICIENT = 6*sqrt(55)/55
F= 5 ,Fp= 4 ,mf= 5 ,mfp= 4 ,q= -1 ,    CG COEFFICIENT = 3*sqrt(11)/11
F= 5 ,Fp= 5 ,mf= -4 ,mfp= -5 ,q= -1 ,    CG COEFFICIENT = sqrt(6)/6
F= 5 ,Fp= 5 ,mf= -3 ,mfp= -4 ,q= -1 ,    CG COEFFICIENT = sqrt(30)/10
F= 5 ,Fp= 5 ,mf= -2 ,mfp= -3 ,q= -1 ,    CG COEFFICIENT = sqrt(10)/5
F= 5 ,Fp= 5 ,mf= -1 ,mfp= -2 ,q= -1 ,    CG COEFFICIENT = sqrt(105)/15
F= 5 ,Fp= 5 ,mf= 0 ,mfp= -1 ,q= -1 ,    CG COEFFICIENT = sqrt(2)/2
F= 5 ,Fp= 5 ,mf= 1 ,mfp= 0 ,q= -1 ,    CG COEFFICIENT = sqrt(2)/2
F= 5 ,Fp= 5 ,mf= 2 ,mfp= 1 ,q= -1 ,    CG COEFFICIENT = sqrt(105)/15
F= 5 ,Fp= 5 ,mf= 3 ,mfp= 2 ,q= -1 ,    CG COEFFICIENT = sqrt(10)/5
F= 5 ,Fp= 5 ,mf= 4 ,mfp= 3 ,q= -1 ,    CG COEFFICIENT = sqrt(30)/10
F= 5 ,Fp= 5 ,mf= 5 ,mfp= 4 ,q= -1 ,    CG COEFFICIENT = sqrt(6)/6
F= 5 ,Fp= 6 ,mf= -5 ,mfp= -6 ,q= -1 ,    CG COEFFICIENT = 1
F= 5 ,Fp= 6 ,mf= -4 ,mfp= -5 ,q= -1 ,    CG COEFFICIENT = sqrt(30)/6
F= 5 ,Fp= 6 ,mf= -3 ,mfp= -4 ,q= -1 ,    CG COEFFICIENT = sqrt(330)/22
F= 5 ,Fp= 6 ,mf= -2 ,mfp= -3 ,q= -1 ,    CG COEFFICIENT = sqrt(66)/11
F= 5 ,Fp= 6 ,mf= -1 ,mfp= -2 ,q= -1 ,    CG COEFFICIENT = sqrt(462)/33
F= 5 ,Fp= 6 ,mf= 0 ,mfp= -1 ,q= -1 ,    CG COEFFICIENT = sqrt(154)/22
F= 5 ,Fp= 6 ,mf= 1 ,mfp= 0 ,q= -1 ,    CG COEFFICIENT = sqrt(110)/22
F= 5 ,Fp= 6 ,mf= 2 ,mfp= 1 ,q= -1 ,    CG COEFFICIENT = sqrt(165)/33
F= 5 ,Fp= 6 ,mf= 3 ,mfp= 2 ,q= -1 ,    CG COEFFICIENT = sqrt(11)/11
F= 5 ,Fp= 6 ,mf= 4 ,mfp= 3 ,q= -1 ,    CG COEFFICIENT = sqrt(22)/22
F= 5 ,Fp= 6 ,mf= 5 ,mfp= 4 ,q= -1 ,    CG COEFFICIENT = sqrt(66)/66
F= 4 ,Fp= 3 ,mf= -3 ,mfp= -3 ,q= 0 ,    CG COEFFICIENT = -sqrt(7)/6
F= 4 ,Fp= 3 ,mf= -2 ,mfp= -2 ,q= 0 ,    CG COEFFICIENT = -sqrt(3)/3
F= 4 ,Fp= 3 ,mf= -1 ,mfp= -1 ,q= 0 ,    CG COEFFICIENT = -sqrt(15)/6
F= 4 ,Fp= 3 ,mf= 0 ,mfp= 0 ,q= 0 ,    CG COEFFICIENT = -2/3
F= 4 ,Fp= 3 ,mf= 1 ,mfp= 1 ,q= 0 ,    CG COEFFICIENT = -sqrt(15)/6
F= 4 ,Fp= 3 ,mf= 2 ,mfp= 2 ,q= 0 ,    CG COEFFICIENT = -sqrt(3)/3
F= 4 ,Fp= 3 ,mf= 3 ,mfp= 3 ,q= 0 ,    CG COEFFICIENT = -sqrt(7)/6
F= 4 ,Fp= 4 ,mf= -4 ,mfp= -4 ,q= 0 ,    CG COEFFICIENT = -2*sqrt(5)/5
F= 4 ,Fp= 4 ,mf= -3 ,mfp= -3 ,q= 0 ,    CG COEFFICIENT = -3*sqrt(5)/10
```

There are a lot! We can narrow this down by noting that there is a selection rule that says that F can only change by ± 1. Since we need to go both directions, we have to have $F = 4$ or $F = 5$

```
In [3]: Fs=[S(4),S(5)]
        Fps=[S(5),S(4)]
        qs=[S(-1),S(0),S(1)]
        for q in qs:
            for F in Fs:
                for Fp in Fps:
                    for mf in range(-F,F+1):
                        for mfp in range(-Fp,Fp+1):
                            if((CG(F,mf,S(1),q,Fp,mfp).doit()<>0)and (mf==0)):
                                print 'F=',F,',Fp=',Fp,',mf=',mf,',mfp=',mfp,',q=',q,'
        ,    CG COEFFICIENT =',CG(F,mf,S(1),q,Fp,mfp).doit(), ', other CG=',CG(Fp,mfp,
        S(1),q,F,mf).doit()
```

```
F= 4 ,Fp= 5 ,mf= 0 ,mfp= -1 ,q= -1 ,    CG COEFFICIENT = sqrt(3)/3 , other CG=
0
F= 4 ,Fp= 4 ,mf= 0 ,mfp= -1 ,q= -1 ,    CG COEFFICIENT = sqrt(2)/2 , other CG=
0
F= 5 ,Fp= 5 ,mf= 0 ,mfp= -1 ,q= -1 ,    CG COEFFICIENT = sqrt(2)/2 , other CG=
0
F= 5 ,Fp= 4 ,mf= 0 ,mfp= -1 ,q= -1 ,    CG COEFFICIENT = sqrt(22)/11 , other CG
= 0
F= 4 ,Fp= 5 ,mf= 0 ,mfp= 0 ,q= 0 ,    CG COEFFICIENT = sqrt(5)/3 , other CG= -s
qrt(55)/11
F= 5 ,Fp= 4 ,mf= 0 ,mfp= 0 ,q= 0 ,    CG COEFFICIENT = -sqrt(55)/11 , other CG=
 sqrt(5)/3
F= 4 ,Fp= 5 ,mf= 0 ,mfp= 1 ,q= 1 ,    CG COEFFICIENT = sqrt(3)/3 , other CG= 0
F= 4 ,Fp= 4 ,mf= 0 ,mfp= 1 ,q= 1 ,    CG COEFFICIENT = -sqrt(2)/2 , other CG= 0
F= 5 ,Fp= 5 ,mf= 0 ,mfp= 1 ,q= 1 ,    CG COEFFICIENT = -sqrt(2)/2 , other CG= 0
F= 5 ,Fp= 4 ,mf= 0 ,mfp= 1 ,q= 1 ,    CG COEFFICIENT = sqrt(22)/11 , other CG=
0
```

I want to be able to go from F=4 to F=5. Therefore, if A is the transition operator, then I need to find some state $|i\rangle$ that satisfies

$$\langle i|A|g\rangle \neq 0$$

and

$$\langle e|A|i\rangle \neq 0.$$

```
In [4]: F4=S(4)
        F5=S(5)
        Fps=[S(5),S(4)]
        qs=[-1,0,1]
        for q in qs:
            print "q is ",q
            for Fp in Fps:
                for mf in [S(0)]:
                    for mfp in range(-Fp,Fp+1):
                        if((CG(F5,mf,S(1),-q,Fp,mfp).doit()<>0)and(CG(Fp,mfp,S(1),q,F4
        ,mf).doit()<>0)):
                            print 'F=',F5,',Fp=',Fp,',mf=',mf,',mfp=',mfp,',q=',q,',
          CG COEFFICIENT =',CG(F5,mf,S(1),-q,Fp,mfp).doit(), ', other CG=',CG(Fp,mfp,S
        (1),q,F4,mf).doit()
                            print 'F=',F4,',Fp=',Fp,',mf=',mf,',mfp=',mfp,',q=',q,',
          CG COEFFICIENT =',CG(F4,mf,S(1),-q,Fp,mfp).doit(), ', other CG=',CG(Fp,mfp,S
        (1),q,F5,mf).doit()
```

```
q is  -1
F= 5 ,Fp= 5 ,mf= 0 ,mfp= 1 ,q= -1 ,    CG COEFFICIENT = -sqrt(2)/2 , other CG=
sqrt(33)/11
F= 4 ,Fp= 5 ,mf= 0 ,mfp= 1 ,q= -1 ,    CG COEFFICIENT = sqrt(3)/3 , other CG= s
qrt(2)/2
F= 5 ,Fp= 4 ,mf= 0 ,mfp= 1 ,q= -1 ,    CG COEFFICIENT = sqrt(22)/11 , other CG=
 sqrt(2)/2
F= 4 ,Fp= 4 ,mf= 0 ,mfp= 1 ,q= -1 ,    CG COEFFICIENT = -sqrt(2)/2 , other CG=
sqrt(2)/3
q is  0
q is  1
F= 5 ,Fp= 5 ,mf= 0 ,mfp= -1 ,q= 1 ,    CG COEFFICIENT = sqrt(2)/2 , other CG= s
qrt(33)/11
F= 4 ,Fp= 5 ,mf= 0 ,mfp= -1 ,q= 1 ,    CG COEFFICIENT = sqrt(3)/3 , other CG= -
sqrt(2)/2
F= 5 ,Fp= 4 ,mf= 0 ,mfp= -1 ,q= 1 ,    CG COEFFICIENT = sqrt(22)/11 , other CG=
 -sqrt(2)/2
F= 4 ,Fp= 4 ,mf= 0 ,mfp= -1 ,q= 1 ,    CG COEFFICIENT = sqrt(2)/2 , other CG= s
qrt(2)/3
```

Clearly, the light must have a "magnetic quantum number" (q) of either 1 or -1, while the intermediate state $|i\rangle$ must have $m'_f = 1$ or -1 (note that m'_f is called mfp in the code).

We are finally ready to make our table. We calculate the Clebsch-Gordan coefficients for values of q_1, q_2, and m_{fi} that allow the transition probability to be nonzero for the transition from $|g\rangle$ to $|i\rangle$ and from $|i\rangle$ to $|e\rangle$. This is pretty similar to before except slightly more neatly organized.

Also, I put in the characters to make a ready-made $\LaTeX$ table.

```
In [5]: Fi=[4,5]
        mfi=[-5,-4,-3,-2,-1,0,1,2,3,4,5]
        q1=[-1,0,1]
        q2=[-1,0,1]

        for Fi_ in Fi:
            for q1_ in q1:
                for q2_ in q2:
                    for mfi_ in mfi:
                        CG1=CG(5,0,1,q1_,Fi_,mfi_).doit()
                        CG2=CG(Fi_,mfi_,1,q2_,4,0).doit()
                        if ((CG1<>0) and (CG2<>0)):
                            print Fi_,'&',q1_,'&',q2_,'&',mfi_,'&$',sympy.latex(CG1),'
        $&$',sympy.latex(CG2),'$ \\\\ \n',

        4 & -1 & 1 & -1 &$ \frac{\sqrt{22}}{11} $&$ - \frac{\sqrt{2}}{2} $ \\
        4 & 1 & -1 & 1 &$ \frac{\sqrt{22}}{11} $&$ \frac{\sqrt{2}}{2} $ \\
        5 & -1 & 1 & -1 &$ \frac{\sqrt{2}}{2} $&$ \frac{\sqrt{33}}{11} $ \\
        5 & 1 & -1 & 1 &$ - \frac{\sqrt{2}}{2} $&$ \frac{\sqrt{33}}{11} $ \\
```

E.4   Spectator theorem

In Chapter 3, we had a need to look up the Wigner 6j symbols for various states. This was done using the following code:

```python
import numpy as np
import pandas as pd
import sympy.physics.wigner as wg
from sympy.physics.wigner import wigner_6j
import sympy
import itertools

Fp=range(10)
F=[4,5]
S=0.5
I=4.5
k=1
Jp=1.5
J=0.5
Lp=1
L=0

def calculate_spectator3():
    answer=''
    for i in itertools.product(Fp,F):
        #calculate Wigner 6j symbols, print if not 0
        if(wigner_6j(Jp,i[0],I,i[1],J,k)<>0):
            theNumber=sympy.simplify(wigner_6j(Jp,i[0],I,i[1],J,k)*(-1)**
(Jp+I+i[1]+k)*sympy.sqrt((2*i[0]+1)*(2*i[1]+1)))
            print theNumber
            #add some characters to make it a LaTeX table
            answer=answer+ "$F'="+str(i[0])+"$,$F="+str(i[1])+"$"
            answer=answer+"&$"+ sympy.latex(theNumber)+"$"
            answer=answer+"&"+str(theNumber.n(3))+"\\\\ \n"
    print answer
    return answer

if __name__=='__main__':
    calculate_spectator3()
```